Synthesis and Characterization of Self-healing Nano-Materials and their Applications

THESIS SUBMITTED FOR THE AWARD OF THE DEGREE OF

Doctor of Philosophy

in

Applied Physics

by

SHAKTI SINGH

Enrolment no.- 426/13

Under the supervision of

Prof. (Dr.) Bal Chandra Yadav

DEPARTMENT OF APPLIED PHYSICS

SCHOOL FOR PHYSICAL SCIENCES

BABASAHEB BHIMRAO AMBEDKAR UNIVERSITY,

LUCKNOW-226025, U.P., INDIA

2022

DECLARATION

I declare that the thesis entitled **"Synthesis and Characterization of Self-healing Nano-Materials and their Applications"** has been prepared by me under the supervision of **Prof. (Dr.) Bal Chandra Yadav**, Department of Applied Physics, School for Physical Sciences, Babasaheb Bhimrao Ambedkar University, Lucknow. No part of this thesis has formed the basis for the award of any degree, diploma or fellowship previously. Further, I declare that the material embodied in the present work is based on original research work and indebtness to others has been duly acknowledged at relevant places. This is also declared that the thesis is essentially free from all kind of plagiarism.

Shakti Singh

(SHAKTI SINGH)

Department of Applied Physics,

School for Physical Sciences,

Babasaheb Bhimrao Ambedkar University,

Vidya Vihar, Raebareli Road, Lucknow-226025, U.P., India

Date: 30/09/2022

Place: Lucknow

CERTIFICATE

This is to certify that the thesis titled **"Synthesis and Characterization of Self-healing Nano-Materials and their Applications"** submitted by **Mr. Shakti Singh** is an original research work and has not been previously submitted in part or full for the award of any other degree or diploma to this or any other university.

This thesis submitted to the Babasaheb Bhimrao Ambedkar University, Lucknow satisfies all the requirements as stipulated in the *Doctor of Philosophy (Ph.D.) regulations-1999 as amended in 2013* and it is fit for submission and evaluation for the award of Doctor of Philosophy of the University.

Prof. (Dr.) Bal Chandra Yadav

(Supervisor)

Prof. (Dr.) Bal Chandra Yadav

(Head of the Department)

विभागाध्यक्ष
Head
भौतिकी विभाग
Deptt. of Physics
बाबा साहेब भीमराव अम्बेडकर विश्वविद्यालय
Baba Saheb Bhimrao Ambedkar University
लखनऊ - 226025 उ0 प्र0, भारत
Lucknow - 226025, U.P., India

Date: 30-09-2022

Place: Lucknow

Dedicated

to

My Parents

Mr. Maheep Narayan Singh,

Mrs. Kavita Singh

&

Lord Shiva

ACKNOWLEDGEMENT

It is my firm belief that any major research work to result in a positive outcome including a worthy thesis requires the culmination of several factors such as a meaningful subject which can motivate a determined researcher to take up the challenge, a learned and sincere guide in the form of friend, relative and colleague who selflessly encourage and help the researcher throughout the research. I had the honour and privilege to have **Prof. (Dr.) Bal Chandra Yadav** as an excellent guide. I take this opportunity to place on record my heartfelt and sincere gratitude and deep indebtedness to him, without whose guidance this work could not have been meaningfully concluded.

I am extremely thankful to **Prof. Devesh Kumar, Dr. Ramesh Chandra**, **Dr. Anil Yadav**, **Dr. Khem Bahadur Thapa, Dr. Devendra Singh, Dr. Ajeet Kr. Maurya** for their valuable suggestions and encouragements which have been a great asset to me during the entire course of study. I owe my deep gratitude towards them for their constant motivation and moral support. I feel myself blessed to have such teachers. I am also blessed with the guidance and support of Prof. Gulzhian I. Dzhardimalieva (Russia), Dr. Manoj Kumar Gupta (AMPRI-Bhopal), Dr. Jinhwan Yoon (PNU-South Korea), Dr. Jiwan Singh, Dr. Chiranjit Maiti (PNU-South Korea), and Dr. Ravi Kant Tripathi. Without guidance of them this work could not have been meaningfully concluded.

Also, I am thankful to the staff members at Babasaheb Bhimrao Ambedkar University especially **Dr. Mukesh Kumar** (USIC), **Mr. Mukesh Tyagi** (DAP), **Mr. Amit Kumar** (DAP) and **Mr. Shatrughan Lal** (DAP).

I wish to express my reverence and sense of deep gratitude to **Dr. Abhisikta Bhaduri** for her continuous support and providing help at any hour of need. Without her contributions, the thesis would not be in its present form.

I express my gratitude towards my seniors **Dr. Monika Singh**, **Dr. Samiksha Sikarwar**, and **Dr. Utkarsh Kumar** for their constant support in academic upliftment. I would like to acknowledge the contribution of my juniors **Mr. Ajeet Singh**, **Mr. Arpit verma, and all lab mates** for a joyful and healthy environment around me to work.

I am also thankful to USIC BBAU, IIT Delhi, CSIR-AMPRI (Bhopal) and NPL India for providing characterization facilities for my samples.

I gratefully acknowledge **Babasaheb Bhimrao Ambedkar University, Lucknow** for providing financial support in form of **UGC non-NET fellowship**.

Finally, I would like to pay my highest regard and owe my indebtness towards my parents **Mr. Maheep Narayan Singh** and **Mrs. Kavita Singh** for their love, support and sacrifice from the very first day of my journey of life. I am highly thankful to **Mr. Siddharth Singh** and **Ms. Shikha Singh**, and all family members for their love and support.

Last but not the least, my final words of thanks will be for Almighty Shiva, for his countless blessings, mercy and companionship through all turmoil of my life.

Shakti Singh

(Ph.D. Scholar)

List of Publications

Part of the thesis published and communicated in the refereed journals:

1. **S. Singh,** A. Bhaduri, R.K. Tripathi, K.B. Thapa, R. Kumar, B.C. Yadav, Improved sensing behaviour of self-healable solar light photodetector based on core-shell type $Ni_{0.2}Zn_{0.8}Fe_2O_4$@ poly (Urea-Formaldehyde), Sol. Energy. 188 (2019) 278–290.
2. **S. Singh,** R.K. Tripathi, M.K. Gupta, G.I. Dzhardimalieva, I.E. Uflyand, B. Yadav, 2-D self-healable polyaniline-polypyrrole nanoflakes based triboelectric nanogenerator for self-powered solar light photo detector with DFT study, J. Colloid Interface Sci. 600 (2021) 572–585.
3. S. Singh, P. Yadav, M.K. Gupta, G.I. Dzhardimalieva, J. Yoon, C. Maiti, B.C. Yadav, Gigantic stimulation in response by solar irradiation in self-healable and self-powered LPG sensor based on triboelectric nanogenerator: Experimental and DFT computational study, Sensors Actuators B Chem. 359 (2022) 131573.
4. S. Singh, C. Bhan, M.K. Gupta, J. Yoon, C. Maiti, J. Singh, B.C. Yadav, Waste Material Based Self-Healable and Self-Powered Detection of Hazardous Fluoride Ions and its Removal with Novel Adsorbent: An Unexplored and Highly Responsive Detection Method, Journal of Hazardous materials. **(Under Review)**

Work not included in the Thesis

1. A. Bhaduri, S. Singh, K.B. Thapa, B.C. Yadav, Improved room temperature liquefied petroleum gas sensing performance of $Ni_{0.5}Zn_{0.5}Fe_2O_4$@Cl-doped polypyrrole nanoweb, Mater. Sci. Eng. B. 279 (2022) 115660.
2. A. Bhaduri, S. Singh, K.B. Thapa, B.C. Yadav, Visible light-induced, highly responsive, below lower explosive limit (LEL) LPG sensor based on hydrothermally synthesized barium hexaferrite nanorods, Sensors Actuators B Chem. 348 (2021).
3. G.I. Dzhardimalieva, B.C. Yadav, S. Singh, I.E. Uflyand, Self-healing and shape memory metallopolymers: State-of-the-art and future perspectives, Dalt. Trans. 49 (2020) 3042–3087.
4. A. Bhaduri, S. Singh, R.K. Tripathi, U. Kumar, K.B. Thapa, B.C. Yadav, Healable, highly sensitive LPG sensor based on $Ni_{0.4}Zn_{0.6}Fe_2O_4$ nanohybrid grown by auto combustion process, Sensors Actuators B Chem. 327 (2021) 128840.

5. S. Sikarwar, **S. Singh**, Satyendra, R. Srivastava, B.C. Yadav, V. V. Tyagi, Design and development of lab model of piezo-optic sensor for Structural Health Monitoring, Smart Mater. Struct. 26 (2017) 105047.
6. S. Sikarwar, Satyendra, **S. Singh**, B.C. Yadav, Review on pressure sensors for structural health monitoring, Photonic Sensors. 7 (2017) 294–304.
7. A. Singh, **S. Singh**, B. C. Yadav, Gigantic enhancement in response of heterostructured CeO_2/CdS nanospheres based self-powered CO_2 gas sensor: A comparative study, Sensors Actuators B Chem. **(Under review)**
8. P. Yadav, A. Singh, **S. Singh**, D. Shukla, Design and development of Paper/ZnO-SnO_2 heterostructured ultra-fast TENG based LPG sensor, ECS Sensor plus. **(Under review)**

Papers presented in National and International Conference/Webinar/Workshop

1. National Conference on "Sukshm Padarth evam Sambaddh Chetan Urja" 1st – 3rd February, 2019, BBAU, Lucknow. **(Oral Presentation)**
2. International Webinar on Nanoscience and Nanotechnology (IWNN-2020), 27th – 29th November, 2020, BBAU, Lucknow **(Oral presentation)**.
3. International Conference on Frontiers in Physics, Materials Science & Nanotechnology (FPMSN-2022) March 25-26, 2022, Sirsa **(Oral presentation).**
4. International Conference on Recent advances in Science (ICRAS-2022), 1st-2nd April, 2022, Bareilly **(Oral Presentation)**.
5. WEBINAR on 'SCIENCE: In Today's Prospect' February 28, 2022, Siddharthnagar **(Oral Presentation)**.
6. International Conference on Nanoscience and Nanotechnology (ICNN-2017), 22th – 24th September, 2017, BBAU, Lucknow **(Poster presentation)**.
7. "Synergistic Training Utilising the Scientific and Technological Infrastructure" (STUTI) training workshop, 22-28 August, 2022, BBAU, Lucknow **(Workshop)**

Achievements

- Project fellow in Indo-Russian project-2019 (Reference no. INT/RUS/RFBR/P-375).
- 13 days working in IPCP- Russian Academy of Sciences, Chernogolovka, Russia for synthesizing self-healable polymers and Advance polymerization synthesis technique under Indo-Russian project-2021
- 10 days of research work in CSIR-AMPRI (Bhopal) for developing hybrid nanogenerators for self-powered sensing applications.
- Best oral presentation at International conference on Recent Advances in Science (ICRAS-2022), Bareilly.
- Best oral presentation at webinar on National Science Day-2022, Lucknow.
- Best oral presentation at International webinar on Nanoscience and Nanotechnology (IWNN-2020), Lucknow.
- Best poster presentation at International conference on Renewable Energy for Sustainable Environment: Challenges and Remedies (ICRESE-2017), Jammu.

ABSTRACT

Nanomaterials exhibit chemical and physical traits that are completely different from their bulk counterparts, owing to their unique shapes and small sizes. At smaller sizes, high surface-to-volume ratio, along with quantum confinement occur in material, which are the main reasons behind the altered properties.

Among various branches of nanomaterials, self-healing nanomaterials are considered to be very astonishing, as these materials are able to reconstruct their structures after any damage, just like lizard tail and star fish. These days, the self-healable materials are being utilized in different devices like sensors, solar cells, batteries etc., which lengthens the service life of these devices by successfully restoring their structure after any deformation occurs. There are two different kinds of self-healing phenomena are realized in practice: **(1)** Intrinsic self-healing materials, where the healing is achieved from reversible covalent and noncovalent bonds, and **(2)** Extrinsic self-healing materials where an external agent is needed to exhaust the healing substance into the damaged site.

In this work, the self-healable nanomaterials were combined in different applications to attain self-healable and self-powered sensing device. The sensors being devices to realize the changes in some physical variable and gives an output as a function of that input. Nanogenerators were used to make the devices self-powered, as these are capable of generating electrical energy from mechanical energies. The self-healing materials were used to recover the damages occurring in the self-powered sensing devices due to repetitive application of mechanical stress.

There are six chapters in the thesis and a brief outline of its contents is as follows:

Chapter 1 comprehends the basic information of the self-healing materials, along with their types, synthesis techniques, properties and applications in different fields of nanotechnology. This chapter also focuses on different self-healing materials along with their healing mechanism. A detailed investigation about the progress in self-healing materials, and usage of different self-healing materials in different applications are also included here. This chapter also elaborates different self-powered devices using

nanogenerators. The advantages of self-powered sensors over traditional resistive sensors are discussed as well.

Chapter 2 includes the preparation of a dual layered photo detector, with the lower layer containing microcapsules of urea-formaldehyde polymer, encircling a mixture of $Ni_{0.2}Zn_{0.8}Fe_2O_4$ and flaxseed oil, serving as the healing element, while the upper layer is of $Ni_{0.2}Zn_{0.8}Fe_2O_4$ playing the role of detection element. The $Ni_{0.2}Zn_{0.8}Fe_2O_4$ was prepared using citrate gel method, and the microcapsules of U-F infused with flaxseed oil and $Ni_{0.2}Zn_{0.8}Fe_2O_4$ core were prepared by oil emulsion process. The synthesized materials were investigated using TEM, SEM, FTIR, UV-visible absorption spectroscopy, TGA and XRD. The healing phenomena was demonstrated after creating an artificial crack in the dual layered film, and the healing was confirmed using SEM and EDS analysis. When exposed to visible light, both the uncracked and healed films exhibited very good response and ~98.5% restoration of the sensing capability was achieved through healing.

Chapter 3 involves the demonstration of self-healable and self-powered visible light photo detector. Polyaniline-Polypyrrole (PANI-PPY) nano flakes were used in the device and it was prepared using low temperature aided oxidative polymerization method. The formation of the nano flakes is also explained here via thermal scission and surfactant effect. The nano flakes were tested using SEM, FTIR, XRD, and Raman spectroscopy in detail. An optical absorption spectra spread in the visible region along with the optical band gap ~1.85eV. The detection was performed using TENG as power supply (maximum voltage ~149 volts, maximum current ~16 μA). With this setup, the nano-flakes showed a sensitivity of ~2.78 %response/mWcm^{-2}. The most novel characteristic of this research is acetone supported rapid self-restoration presented in Polyaniline-Polypyrrole (PANI-PPY) nano flakes, showing maximum healing efficiency ~99.8%.

Chapter 4 comprises of a self-powered, self-healable, and visible light-enhanced LPG sensor based on PANI-PPY 2-dimensional nano-sheets. The preparation of PANI-PPY (1:4) was similar to what followed in chapter 3 except the ratio of monomers. SEM, EDS, HRTEM FTIR, RAMAN, XRD, BET and TGA analysis were performed to characterize the material. The band gap ~2.02 eV was measured from Tauc plot using UV-Visible spectrum. The material exhibited brilliant LPG detection

below its LEL (sensitivity ~52.67 SR/vol.%), when illuminated with visible light of 30 mW/cm^2 at room temperature. The sensor was operated with TENG (3P) that generated an output voltage and current of ~142 volt and 80 μA respectively. Self-healing ability was also successfully introduced in the TENG layer to regain its properties after any damage. The Maximum healing efficiency of ~99.7% was achieved here.

Chapter 5 deals with a unique, cost-effective, and quick method for the detection of fluoride ions in water. The detection unit was fabricated with waste materials like BSR rubber, used polythene bag, and used plastic sheet, validating the waste to energy conversion ability with maximum output voltage ~242 volts and current ~40 μA. BSR ornamented with Lanthanum doped Polyaniline-Polypyrrole (LaPP) nanospheres (BSR-La) dispersed in PDMS (PDMS/BSR-La) matrix was used to prepare one layer of the TENG. The following layer is also self-healable in nature. The materials were characterized by SEM, EDX, elemental mapping, FTIR, XRD, and UV-Visible analysis. Using this novel detection unit, a maximum sensor response of 12.10, % sensor response of 1110 %, and 4.7 μM limit of detection was achieved. The PDMS/BSR-La nanocomposite confirmed fast healing in ~25 min with a healing efficiency of 99.9%, which is one of the unique features of this device.

Chapter 6 deals with the summarized results obtained from preparation of all materials and fabrication of different devices. This chapter also includes the summarised information of the material characteristics and sensing performances. This chapter also gives the guidelines for further research work in the field of self-healable and self-powered sensing devices.

PREFACE

As the Nanotechnology is progressing, the materials and devices are now becoming more and more smarter. A single device consists of multiple characteristics and properties. The present thesis contains such a sensing devices, which are both self-healable and battery less at the same time. Among various branches of nanomaterials, self-healing nanomaterials are considered to be very astounding, because these materials are able to renovate their assemblies after any mutilation. The purpose of studies presented in this thesis is to assemble various sensing devices like LPG, photo and chemical sensor, which have both self-rejuvenating and self-powering capabilities.

The present thesis is sectioned into five chapters. **Chapter 1** contains explanation of the self-healing materials, their types, self-healing process, properties and synthesis method. A thorough literature investigation of previously reported self-healable materials was also presented in this chapter. Further various synthesis techniques along with healing mechanism were also described. This chapter describes various types of self-powered devices based on nanogenerators in which self-recovering materials are used. **Chapter 2** describes dual layered core-shell type $Ni_{0.2}Zn_{0.8}Fe_2O_4$@ poly (Urea-Formaldehyde) photo detection sensor, which can reoccupy its actual sensing performance after damage occurs in its physical structure. **Chapter 3** deals with the 2-D PANI-PPY based self-healable and self-powered visible light photo detector, which was produced using low temperature aided oxidative polymerization method. A TENG was used to power the photo sensing film, which is self-healable via interaction with acetone. **Chapter 4** deals with PANI-PPY 2-dimensional nano-sheets based self-powered, self-healable, and visible light-enhanced LPG sensor. In this chapter the sensing performance was enhanced via incorporating visible light in LPG sensing. The healing phenomenon was achieved without using any external trigger source. **Chapter 5** describes a unique, cost-effective, and quick detection method of fluoride ions in water. A new self-powered technique is used and validated to detect fluoride ions, using a TENG based device fabricated using hazardous waste (BSR) coated with Lanthanum doped PANI-PPY, used polythene bag, and used plastic sheet, which validates the waste to energy conversion ability. **Chapter 6** explains with the proportional analysis of all synthesized materials and fabricated devices. This chapter deals with the summarised information of the material characteristics, sensing output, and future scope of all the chapters.

List of Abbreviations

S. No.	Name Compound	Full name
1.	NZF	Nickel Zinc Ferrite
2.	PANI-PPY	Polyaniline-Polypyrrole
3.	SHMs	Self-healing materials
4.	SEM	Scanning Electron Microscope
5.	EDS	Energy Dispersive X-ray Spectroscopy
6.	UV-vis	Ultra Violet-Visible Spectroscopy
7.	TEM	Transmission Electron Microscope
8.	FTIR	Fourier Transform Infrared Spectroscopy
9.	XPS	X-ray Photoelectron Spectroscopy
10.	LPG	Liquified Petroleum Gas
11.	LEL	Lower Explosive Limit
12.	NPs	Nanoparticles
13.	NIOSH	National Institute for Occupation Safety and Health
14.	OSHA	Occupational Safety and Health Administration
15.	XRD	X-Ray Diffraction
16.	TGA	Thermogravimetric analysis
17.	SHNs	Self-healing nanomaterials
18.	MPs	Metallopolymers
19.	NGs	Nanogenerators
20.	TENG	Triboelectric nanogenerator
21.	LaPP	Lanthanum doped Polyaniline-Polypyrrole
22.	BSR	Butadiene-styrene rubber

LIST OF TABLES

LIST OF FIGURES

Appendix: Experimental Methods and Characterization Technique

LIST OF APPENDICES

TABLES OF CONTENTS

Chapter 1

Introduction and Aim of Present Work

This chapter illuminates overview of self-healing nanomaterials, types, their self-healing mechanisms, properties and synthesis techniques. The present chapter also concentrates on different application of self-healing constituents in electronic gadgets. A thorough investigation of previously reported works in the area of self-healable electronic devices like sensors, nanogenerators as well as other devices are presented in this Chapter. Also, discussions have been carried out on the working mechanism of different sensors like photo, gas and fluoride sensors, which are performed to demonstrate self-healable sensing devices. Overall, this chapter highlights the problems that emerged in the previously reported researches and motivations for further research work.

1.1 Introduction to nanomaterials

Nanomaterials have developed as a thrilling class of materials, which had been taken after the Greek term "NANOS" or Latin term "NANUS", meaning of which is ''dwarf". The dimension of a nanomaterial can be imagined through the example of the size of 5 silicon or 10 hydrogen atoms aligned, which is 1 nanometer with one of their dimensions in the range of 1 to 100 nm. Nanotechnology receiving consideration in nearly all divisions of science and technology like medicine, engineering, environment, electronics, defence, security, etc.

The nanomaterials display different physical and chemical behaviour than the bulk material because of their shape and size. Astonishingly, the nanomaterials show advanced features and proficiencies through the modifications of the size and shape at the nano dimension, which is called the "size effect". Other than the size effect, "Quantum confinement" also shows a crucial role in showing amazing properties in nano regime. These properties are as follows:

- **In size effect**, the decrement of the particle size enhances the number of particles present on the particle surface. When bulk particles break into smaller nanoparticles, the overall surface-to-volume ratio (S/V) increases (as S/V is directly proportional to 3/r, r being the radius of the particle). The chemical, excitation, reactivity, emission, and stability properties are dependent on size.
- **In the quantum confinement effect**, the word "quantum confinement" primarily deals with confined electron energy. In the case of nanomaterials, the energy levels of electrons become discrete rather than continuous as in bulk material. This type of property appears when the dimensions of the confining structure approach near to de Broglie wavelength of electrons, which results in discrete energy levels. Due to this effect unique optical, electronic and magnetic behaviour. Based on this confinement, the nanomaterials are zero dimension (all dimensions are confined in nano regime), one dimension (only one dimension is confined in nano regime), two dimensions (two dimensions are confined in

nano regime), and three dimensions (all dimensions are not confined in nano regime like in core-shell nanomaterial)

1.2 Self-healing nanomaterials

In the past decade, self-healing materials (SHMs) have shown the most optimistic growth in the research fields of materials science. It is one of the furthermost fascinating and complicated capabilities of repairing damages. Self-healing properties actually mimic the healing functionality found in some natural creatures like starfish and lizard tails. Most of the materials possess a principal concern of mechanical deformation. Owing to repeated environmental weathering and mechanical pressure, internal stress arises, which leads to degradation and decrement of the proper functioning of that particular material. Similarly, when mechanical or environmental forces are applied continuously to electronic devices like solar cells, sensors, batteries, etc, their output performances decrease slowly. To tackle these problems, Self-healing constituents are used nowadays in various kinds of electronic devices like solar cells, sensors, batteries, etc and in building materials. Polymers and metallopolymers are generally used as self-healing materials. This can upsurge the working life, protection and cost-effectiveness of these devices and structures. Self-healing nanomaterials (SHNs) are used in an extensive variety of applications, for example, in biomedicine, tissue engineering, biomaterials, smart materials, etc. In electronic devices, by using the self-healing nanomaterials the output performance of the device can be stabilized throughout a long period i.e. after mechanical deformation these electronic devices can regain their original functionality by self-generation behaviour.

1.2.1 Classification of self-healing nanomaterials

Depending on the material and healing agent used, self-healing nanomaterials are classified into 2 categories as shown in Fig. 1.1:

1.2.1.1 Intrinsic self-healing materials

Intrinsic SHNs comprise of reversible non-covalent and covalent bonds, resettlement of which gives renovation of the polymeric assembly afterwards deformation. The concept of intrinsic curing depends on the mechanism that frail bonds

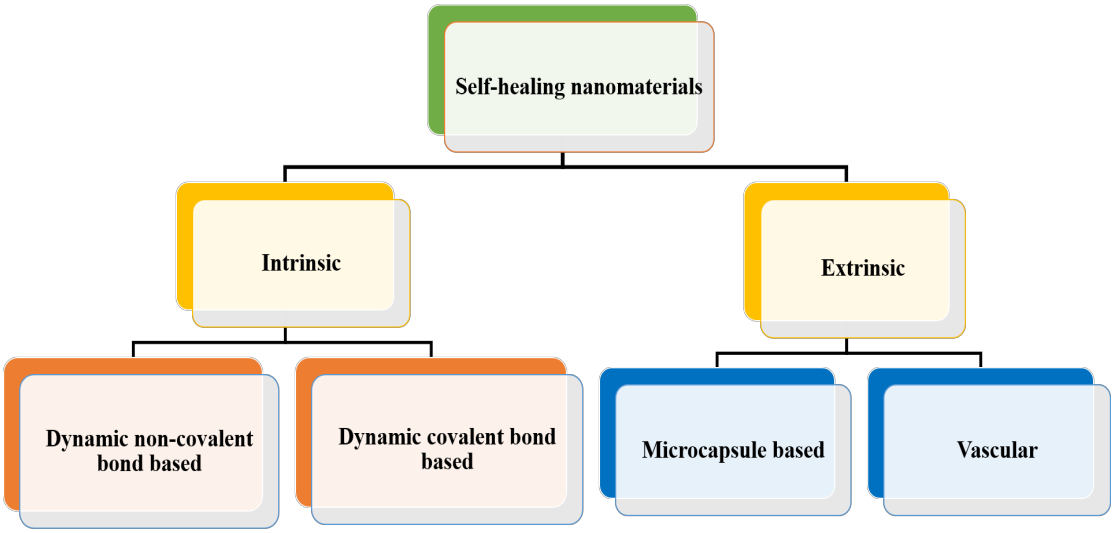

Fig.1.1 Types of self-healing materials.

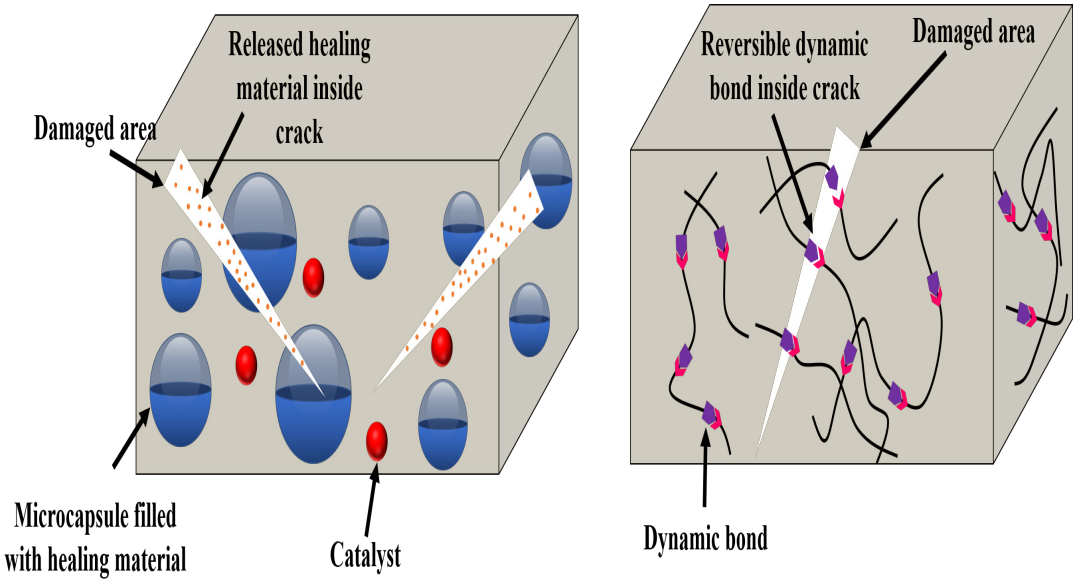

Fig.1.2 Difference in Extrinsic and Intrinsic self-healing.

can be shattered through mechanical stress with the development of species with low molecular weight, which, consecutively, can recover more rapidly/easily, inspiring

quicker healing. In intrinsic self-healing, the process of healing relies on the alterable frail chemical bonds of polymeric chains that include dynamic non-covalent bonds and dynamic covalent bonds.

- **In dynamic non-covalent bond**, the process of healing is governed by metal coordination bonding, hydrogen bonding, electrostatic cross-linking, etc. In this type, the healing procedure generally happens in the time periods extending from minutes to hours. Various kinds of outward incentives like heat, light, humidity, and pressure can be utilized to boost the speed of healing. Metal–ligand (M–L) noncovalent bonds deliver amazing flexibility regarding the strength of the bonds (50–400 kJ mol^{-1}) via altering the pH or the metal ion in the polymer, which guides towards the controlled mechanical characteristics. It permits the usage of different M–L mixtures for the preparation of shape memory and self-healing materials. Recently, many metallopolymers (MPs) with remarkable characteristics have been employed in numerous applications as functional materials.
- **In dynamic covalent bonds,** many kinds of dynamic covalent bonds like acyl hydrazone, Diels–Alder reaction, ester, disulphide, olefin, and imine are investigated to synthesize the intrinsic self-healing nanomaterials. As compared with noncovalent bonding, external forces like heat, pH, pressure and light are always required to activate the healing procedure, as a consequence of the slow formation dynamic of covalent bonds. It is also denoted as a non-autonomous self-healing process. Their main benefit is an unlimited quantity of recurrences of the healing procedure without the extra addition of healing materials. The reversible covalent bonds are usually fused into polymers by means of cross-linkages, hence, these bonds will initially disrupt and then reorganized under the effect of exterior inducements, advancing towards repetitive self-healing.

1.2.1.2 Extrinsic self-healing materials

Here, the healing procedure necessitates the exhaustion of healing agents which are pre-placed during the production. This self-healing practice is labelled as “extrinsic self-healing” because the healing phenomenon is not an intrinsic property of these materials, but some external agent is required to rapture the healing container inside the

matrix. Extrinsic self-healing materials release their self-healing negotiator that are encapsulated in "capsules" or "pipes". When damage occurs, the regenerating mediators come out from these microcapsules or pipes at the damaged zones to renovate the fractures by polymerization or materially filling the gap.

- **In microcapsule based extrinsic self-healing,** microcapsules with micro or nano healing agents are incorporated into the interior of the polymer. Within these microcapsules regenerating agents are filled, which is conveyed towards the impaired region prior to fracture of the capsule. The concept of microcapsule-based self-healing was anticipated by White et al. [1]. They implanted capsules comprising healing material and catalyst inside a matrix attaining quite good self-healing proficiency. Ever since, microcapsule-based healing gained attention worldwide and were widely explored by several scientists owing to their versatile applicability and prospective production in large quantities.
- **In vascular-based extrinsic self-healing,** equivalent to blood vessels in the biological system, vascular or fibre-based self-healable structures incorporate rejuvenating agents into a matrix through micro-channels. This novel idea is proposed by Toohey et al. [2], in which integration of a micro-channel network comprising dicyclopentadiene (DCPD) in the material. These micro-channels transported DCPD self-organizing agent to an epoxy superficial coating comprising Grubbs' catalyst.

1.2.2 Mechanism of different types of self-healing nanomaterials and literature survey

As discussed above self-healing materials are categorised into two parts: **Intrinsic and Extrinsic**. The mechanism involved in self-healing is shown in Fig. 1.2 as discussed below:

1.2.2.1 Intrinsic self-healing

- **In non-covalent Intrinsic self-healing**, the procedures comprise all weak interactions, like van der Waals interactions, hydrogen bonding, ionic interactions, stacking of π-π, dipole-dipole interactions, host-guest collaborations, and coordination between metal and ligand [3]. Non-covalent self-healing is characterized by the manifestation of the small bonding energy

in comparison to pure covalent healing. Therefore, they generally display excessive healing capabilities and enable the renovation of the fragmented bonding at room temperature. These non-covalent-based healing are mostly employed in elastomers found on hydrogen bonds. Burattini et al. [4] pronounced an amalgamation of hydrogen bonding and π-π stacking in a polyurethane and polyimide elastomer through pyrenyl groups. The healing occurs due to π-π stacking at the π-electron-vacant di-imide clusters and the pyrenyl components enriched with π-electron and hydrogen bondings arose at the intermolecular state, among the terminal remains of the pyrenyl assemblies. In ionic interactions, electrostatic attraction occurs between opposite charge sites. Xu et al. [5] successfully synthesized carboxylated styrene-butadiene rubber (XSBR) packed with nano-chitosan in which ionic clusters allowed the formation of a crosslinked supramolecular system with adjustable bondings at room temperature with healing capabilities up to 92%. In host-guest interaction, the healing occurs due to the acceptance of one whole molecule (guest) by another molecule (host). Xiao et al. [6] synthesized a material grounded on the mixture of hydrogen bonding and host-guest interactions in a water-borne polyurethane.

- **In covalent Intrinsic self-healing,** healing is associated with the bonds which can be originated among dissimilar atoms and are kinetic in the influence of external entities. Disulfide bonds are of R─S─S-R′ type and specially found in diene elastomers because sulphur is main element in cross-linked self-healable reaction [3]. Amine bonds are of R─C═N─R′ type which exhibits exchange and metathesis reactions [3]. In Diels–Alder reaction the chemical reaction occurs between a coupled diene and a replaced alkene, usually labelled as the dienophile, to generate a replaced cyclohexene derivative. This is reversible at a certain temperature [3].

1.2.2.2 Extrinsic self-healing

- **In microcapsule based self-healing**, the healing mediators are filled inside the spherical capsule-shaped polymer. When an external stimulus like light, heat, force etc. is employed in the system, it disrupts the capsule and healing representative is filled inside the cracks [7].

- **In vascular-based self-healing,** the healing material is filled inside a vein-like structure inside a system. These healing agents are packed with either one-part healing coordination or two-part resin and hardener matrix. In one part healing system the healing agents from hollow tubes alone heal the crack. In two part resin-hardener matrix, the cracks were filled when resin comes in contact with hardener after mechanical damage [7].

Table 1.1 provides the literature survey of most prefunding works in the field of self-healing materials, their mechanism and efficiency:

Table 1.1 Literature survey of recent self-healing materials.

S. No.	Self-healing material	Healing mechanism	Healing Efficiency (%)	Operating temperature (°C) and time	Ref.
1	Epoxy and Hardener	Micro-capsule	86	200, 24 hours	[8]
2	Epoxy and Hardener	Micro-capsule	64	50, 24 hours	[9]
3	Di-cyclopentadiene – Wax Grubbs	Micro-capsule	77	80, 48 hours	[10]
4	Epoxy resin (UF)	Micro-capsule	85	220, 1 hour	[11]
5	Epoxy and hollow glass fibres	Vascular	90	125, 75 min	[12]
6	Pyrenyl end-capped polymer	Hydrogen bonds and π —π stacking	80	100, 20 min	[4]
7	Carboxylated SBR	Hydrogen bonds and ionic interactions	92	RT	[5]
8	PDMS	Hydrogen bonds and ionic interactions	90	RT, 24 hours	[13]
9	Acrylic copolymer	Hydrogen bonds and Host-guest interactions	75	RT, 24 hours	[14]
10	Polyurethane	Hydrogen bonds and Host-guest interactions	93	100, 36 hours	[6]
11	PDMS	Disulfide bonds and Imine bonds	95	RT, 4 hours	[15]

12	Dynamic hyperbranched polyazomethine	Disulfide bonds and Imine bonds	91	RT, 48 hours	[16]
13	Poly(urea-urethane)	Hydrogen bonds and Disulfide bonds	97	RT, 24 hours	[17]
14	Polyurea	Hydrogen bonds and Disulfide bonds	—	150, 4 hours	[18]
15	Polyurethane	Hydrogen bonds and Diels-Alder chemistry	92	120, 8 hours	[19]
16	PDMS	Hydrogen bonds and Imine bonds	93	RT, 3 hours	[20]
17	Acrylic copolymer	Ionic interactions and Diels-Alder chemistry	86	60, 7 hours	[21]
18	Polysiloxane-based polymer	Hydrogen bonds and π —π stacking	60	120, 20 min	[22]
19	Brominated poly (isobutylene-co-isoprene) rubber	Hydrogen bonds and ionic interactions	39	70, 24 hours	[23]
20	Polyurethane	Hydrogen bonds and Disulfide bonds	88	RT, 60 min	[24]

1.2.3 Synthesis techniques of self-healing nanomaterials

Some of the synthesis techniques of self-healing nanomaterials are summarized below:

1.2.3.1 Micro-emulsion method

Microemulsion synthesis has been established to be a useful route to synthesize a variety of nanomaterials and micro-capsules like urea-formaldehyde. A microemulsion is a stable dispersion (thermodynamically) of two unmixable liquids in the existence of a surfactant. They are known for very low surface tension and large surface area. When oil is mixed in water, spherical droplets of oil are formed inside water, when polymerization of polymer happen in this solution, polymerized material coat on to the oil droplet to create microcapsule [7].

1.2.3.2 Oxidative polymerization method

Oxidative polymerization is utilized for the preparation of the conducting polymers from benzene-based complexes like aniline, phenols, diphenyl, pyrrole,

sulfide, thiophenols etc. The monomers utilized in oxidative polymerization are known for distinct electron donation properties with elevated oxidation tendencies [25]. Oxidation of these monomers is attained by incorporating an oxidizing mediator or a potential difference (i.e., electrochemical oxidative polymerization). During oxidative polymerization, cation sites are produced in the monomer fragment, which initiates polymer growth.

1.2.3.3 Sol-gel method

Sol-gel synthesis is the most commonly used method for the preparation of metal oxides and metallopolymers. Here, 'sol' denotes a colloidal solution in the fluid phase, while 'gel' is termed as an interrelated network formed by metal-polymer chains capturing the liquid. Basically, in a general sol-gel technique, a mixture of metal salts undergoes hydrolysis and condensation chemical reactions to produce polymerized gel system at either room temperature or at an temperature ~25−200 ˚C. Typically the pH of the mixture is altered to deliver uniformity [26].

1.2.4 Applications of self-healing nanomaterials in different electronic devices

Nowadays electronic gadgets, that were bulky and unstable once, are small and highly accurate now. Stretchable electronics along with Flexible nature electronics are now also developing. However, the methods to fabricate these sensors and electronic devices are not resilient to unanticipated mechanical and environmental degradation caused by repetitive wear-tear, unintended cutting and scraping. These unexpected sources cause huge changes or total failure in the expected output performance of electronic devices. Failure of these electronic devices causes the following problems:

- After mechanical damage, when output performance is degraded. These devices are thrown down, which increases the amount of E-waste year by year. According to the global e-waste monitor 2020, nearly 53.6 tonnes of electronic-waste was generated in the year 2019 and this will rise exponentially up to 74.7 tonnes in 2020 [27].
- Reduction of rare and precious materials because of E-waste.
- Maximum of these electronic devices and sensors are made up of toxic materials. Because of e-waste, pollution in soil and groundwater increases.

These e-wastes comprise toxic and heavy metals like Cd, Pb, Hg etc. [28], which infect soil and groundwater and cause serious health problems in all living organisms.

To tackle above described problem, researchers are now discovering new materials, ideas and techniques to fabricate self-generating electronic devices as shown in Fig. 1.3. Different kinds of Self-healable electronic devices like nanogenerators, sensors, solar cells, batteries, super capacitors etc. have been fabricated with fast healing ability, which are summarised below:

1.2.4.1 Perovskite Solar Cells

Methyl ammonium lead iodide ($CH_3NH_3PbI_3$) based perovskite solar cell (PSC) display high efficiency in power conversion surpassing 25%. The deprivation of the perovskite solar cell-based materials in the existence of ultraviolet light, moisture, and oxygen was the foremost serious issue constraining the elongated stability [29]. Recent works in self-healing nanomaterials delivered an auspicious approach for perovskite solar cells to increase or maintain stability [30]. Such as, the main problem with lead halide perovskite materials is degradation when kept in presence of humidity. To remove this deficiency, Zhao et al. [31] devised a self-generating PSC utilizing PEG (polyethylene glycol) as a polymer matrix. PEG particles on the perovskite surface are attached via hydrogen bonding, which efficiently absorbs moisture and acts as an obstruction for the protection of the film from the penetration of water. Due to the strong collaboration between $CH_3NH_3PbI_3$ and PEG, $CH_3NH_3PbI_3$ molecules were healed by PEG. In a different report, Finkenauer et al. [32] described a self-healing of 6-μm scratch after heating at 100 °C for 1 h in a nitrogen atmosphere in hybrid halide PSC by integrating self-rejuvenating thiourea-triethylene glycol inside polycrystalline perovskite. Chu et al. exhibited electrical self-healing by liquid metal microcapsules to re-establish the electrical output performance of flexible PSC [33].

1.2.4.2 Nanogenerators

Nanogenerators, which are mechanical energy harvesters are very prone to mechanical failure due to cyclic stress during operation. These devices (Piezoelectric and triboelectric nanogenerators) are able to produce electrical energy from mechanical

energy by different means. Kim et al. [34] recommended a polyurethane-based shape memory polymer for self-healable triboelectric nanogenerators (TENG) for the restoration of its output results after deprivation. In another work, Xu et al. [35] developed TENG by covering a unique electrode comprising small magnets by self-healing film of polydimethylsiloxane-polyurethane (PDMS-PU). Parida et al. [36] showed a healable and stretchable TENG based on self-rejuvenating polyurethane acrylate. Polyurethane acrylate had hydrogen bonding, which prepared this TENG stretchable (2500%) and healable after damage.

1.2.4.3 Supercapacitors

Supercapacitors (SCs), or, electrochemical capacitors have huge power density, ultra-fast charge and discharge times, and very high cycle lifetimes. The basic ideas of the self-healing electrolytes and electrodes in SCs are to attain the renovation of ionic and electrical conductivities, respectively. Wang et al. [37] conveyed the foremost electrical and mechanical self-healable supercapacitors. In this research, the healable electrodes were designed by adding Single-Walled Carbon Nanotubes (SWCNTs) thin film onto self-restoring substrates. This was made up of a supramolecular web reinforced by TiO_2 nanoparticles. In another work, Sun et al. [38] reported a self-healing yarn-shaped SC depending on a highly proficient conducting wire which serves as the electrode by covering aligned CNT on healable polymer fibers.

1.2.4.4 Batteries

To achieve high energy density, researchers are now developing novel electrode materials for batteries. Lithium Ion Batteries were the most favourable energy storing devices owing to their long lifecycle, high volumetric energy density, and environmental favourability. Flexible Lithium Ion Batteries may be deformed under various strain conditions and the micro-cracks due to the structural variations throughout the continuous charging and discharging processes can utterly lessen the life cycle. Self-recovering Lithium Ion Batteries can reconcile mechanical damages, or micro-cracks formed in the battery interior to expand the lifetime. For this, Zhao et al. [39] presented electrodes that were prepared by positioning CNT sheets on a self-healable substrate. These CNT sheets were coated with $LiMn_2O_4$ and $LiTi_2(PO_4)_3$. Wu

et al. [40] informed a self-healable Lithium Ion Battery anode using Ga-Sn liquid metal alloy, which is decorated on an RGO/CNT skeleton. This structure regained its structure after mechanical deformation.

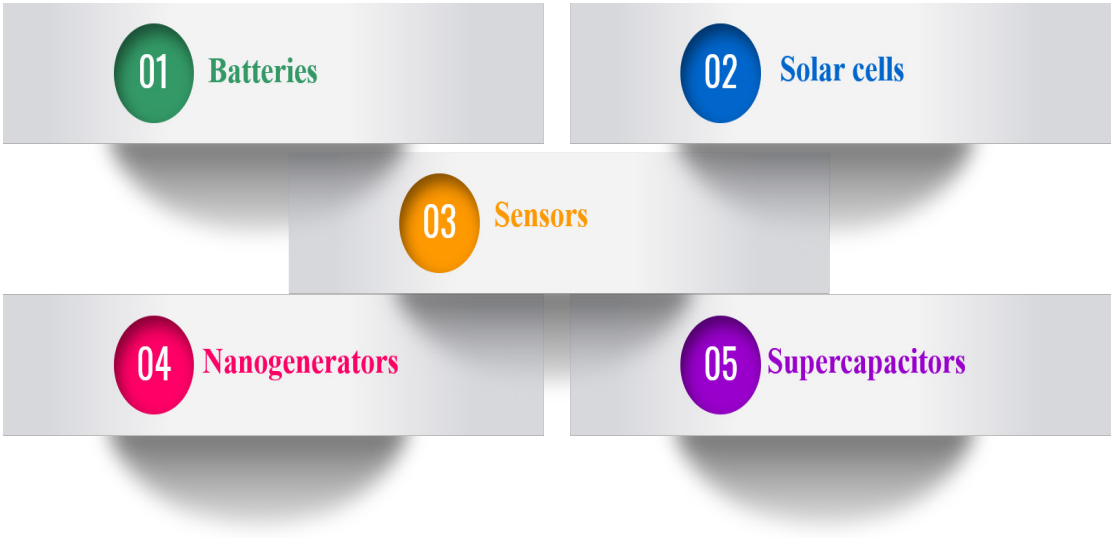

Fig. 1.3 Applications of self-healing materials in different electronic devices.

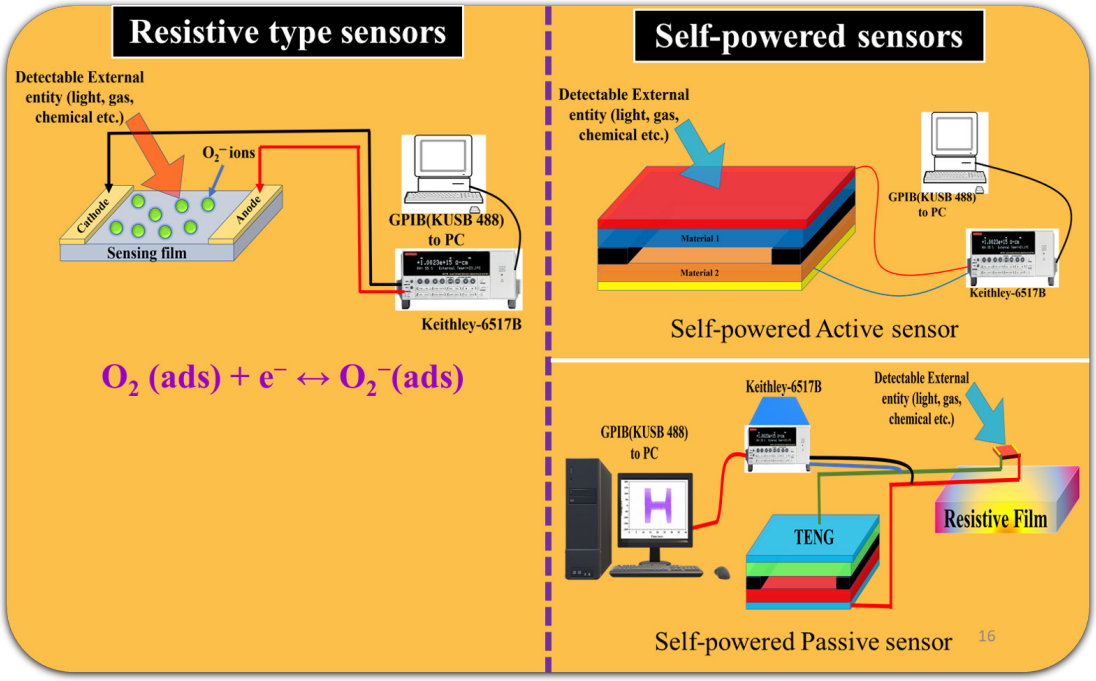

Fig. 1.4 Difference between resistive and self-powered sensors.

1.2.4.5 Sensors

Sensors, which can sense and distinguish external signals, are a member of the central apparatus for fabricating stretchable and habiliment smart electronic sensors. The self-healing materials are most widely used in the sensing area in the electronic field. Huynh et al. [41] presented a self-healable disulfide-cross-linked polyurethane and polyurethane/silver-microparticles (μAg) composite flexible sensor to detect pressure and temperature. The sensor can self-heal the cracks after harsh mechanical damage. Wang et al. [42] produced a conductive polymeric combination of phytic acid, polyacrylic acid, and polyaniline to be used in a pressure sensor. The self-healing with 99% efficiency within 24 hours, because of dynamic contact between hydrogen and electrostatic binding was achieved. Various gas sensors [43], humidity sensors [44], biosensors [45] etc. were fabricated, which shows the huge potential of self-generating materials in the sensor area.

1.2.5 Types of sensors

Sensors can be divided in three types:

- **Physical sensor:** A physical sensor is an instrument, which can compute a physical quantity (like temperature, light, pressure, refractive index etc.) and translates it into a signal that can be identified by an observer or by a device [46, 47,48]. It is important to know that the measurement features comprised in a physical sensor does not involve any chemical reaction. These sensors can be easily fabricated into clothes as a wearable electronics or even used for the assembly of electronic skin.
- **Chemical sensor:** Chemical detection is the part of a data-acquisition method in which the details is obtained about the chemical configuration of the system in instantaneous time. In this method, an electric signal originated from the reaction between a chemical species and the sensing device [48,49]. Various gas sensors [50], humidity sensors [51,52], hazardous ion sensing in drinking water [53–55] etc. have been explored previously by many researchers.
- **Bio sensor:** The word “biosensor” denotes prevailing and pioneering analytical devices including biological sensing components, which have a large array of

applications, like biomedicine, drug discovery, food safety, diagnosis, processing [56] etc. Bio-molecules such as receptors, enzymes, antibodies, micro-organisms etc. have been used as biological sensing elements.

1.3 Nanogenerator and self-powered sensor

The self-powered sensor is very new among all types of sensors, which is based on Nanogenerators. So, before discussing self-powered sensors, it is very vital to discuss nanogenerators and their types.

Nanogenerators are a very new type of energy-harvesting device that generates electric power from unused mechanical energy such as human motion, water waves, wind, vehicle motion etc [57]. Energy is a crucial necessity for everyday life and the ecological growth of our present civilization. Energy is essential in transport, communication, and aviation, as well as for small electronics like sensors, computers, smart phones, and other electronic and electrical equipment. In the last few years, the hasty industrial development, and population progression have amplified the mandate for energy, which increases the overwhelming exhaustion of fossil fuels. This rationalizes the fossil assets. Along with this problem, the rising global warming and climate change reserves are headed to enthusiastic research in the direction of renewable energy sources. The foremost nanogenerator was fabricated by Wang et al. [58] in 2006 using ZnO nanowires based on the piezoelectric effect, which is called piezoelectric nanogenerator (PENG). In the successive development of nanogenerator technology, a triboelectric generator based on the triboelectric effect was firstly introduced in 2012 by Wang et al. [59]. PENG and TENG are two chief associates in the nanogenerator class to harvest mechanical energy that is universally ample in the surroundings. Pyroelectric nanogenerator (PyENG) coverts thermal energy into electrical energy [60]. Another new sort of nanogenerator combining two or more nanogenerators and energy sources was developed, which is known as hybrid nanogenerator (HNG) [61].

1.3.1 Types of nanogenerators

As mentioned earlier, the nanogenerators are of 4 types:

(a) Piezoelectric Nanogenerator (PENG)

(b) Triboelectric Nanogenerator (TENG)

(c) Pyroelectric Nanogenerator (PyNG)

(d) Hybrid Nanogenerator (HNG)

It is very important to discuss the working principle and voltage generation mechanism in these nanogenerators, especially in TENG. Because TENG generates the highest output power among all nanogenerators.

1.3.1.1 PENG

The foremost nanogenerator is revealed in aligned ZnO nanowire (NW) arrays, by scanning with conductive atomic force microscopy (AFM) [58]. We can understand the basic mechanism of PENG by taking an example of this first pioneer work, which depends on the semiconducting and piezoelectric characteristics of these types of materials. The deflection of the piezoelectric material by external force creates a strain field. Negative strain is developed on the compressed part of the piezoelectric material, while positive strain generates throughout the stretched part of the piezoelectric material. Along the strain, an electrical field is generated, when the positive and negative charge centers move. Through this electric dipoles get created inside the piezoelectric materials. Because of the applied external stress, these dipoles align themselves and a net dipole moment is created inside the piezoelectric material, which is the straight outcome of piezoelectric characteristic. The piezoelectric nanogenerators generate a low output voltage than TENG, but the stability is very high in terms of power generation.

1.3.1.2 TENG

TENG, which is the most recent and highest voltage generation nanogenerator among all available nanogenerator works on the principle of “Electrostatic induction” and “Triboelectric effect”. The triboelectric effect is charge transmission by which two distinct materials develop electrical charges in reverse signs after interaction with each other [62,63]. It is well acknowledged that the triboelectric charges are only restricted on the material surface. When both of the different triboelectric materials, get into touch under external force, charges due to the triboelectric effect are generated on their

exteriors. As this force is removed, these charged sides are detached, and a difference in potential is created on the two back electrodes. If these electrodes are coupled to a load, a current is flown amid them to terminate the electric field originated by the charged faces. As the surfaces are carried into touching base again, the potential change on these electrodes alters and the same current drift in the reverse track. By this, an endless AC output is achieved by reciting this sequence. To put it simply, this device functions on the pairing of two occurrences, electrification at the contact, and electrostatic induction. The earlier provides the stationary charges on the surfaces of the material and the later motivations the conversion of mechanical energy to electrical energy by mechanically caused variation in potential.

Four distinct manners of function of the TENG have been proposed [64,65].

- Lateral-sliding mode,
- Vertical contact-separation mode,
- Freestanding triboelectric-layer mode,
- Single-electrode mode.

Among all of the above approaches, the vertical contact-separation mode is preferred, due to its high output generation capacity and versatility [65]. The vertical contact-separation mode utilizes motion at right angles to the interface of two materials, and the difference in potential among electrodes is governed by the gap distance between two surfaces.

The theoretical description of TENG is explained by Maxwell's equation and Maxwell's displacement current is well-defined as below [64]:

$$J_D = \frac{\partial D}{\partial t} = \varepsilon \frac{\partial E}{\partial t} + \frac{\partial P_s}{\partial t} = \frac{\partial \sigma_{Tribo}(z,t)}{\partial t} \qquad (1.1)$$

Where, ε, D, E, P_S are the permittivity of the medium, displacement field, electric field, the polarization originated from the existence of the polarization charges developed on the surface from triboelectric or piezoelectric effect, while σ_{Tribo} is the surface charge density in TENG. The first term in Eqn. (1.1) discusses a time-variable electric field and is the cause of origin of electromagnetic waves, whereas the last term denotes the role from polarization of surface and is the cause of origin of

nanogenerators. Extra precisely, in TENGs, outward electrostatic charges that are induced from contact electrification generate surface polarization which is time-varying in nature, as two different materials come in touch.

1.3.1.3 PyNG

Thermal energy is one of the profuse energy available in the atmosphere. Thermoelectric energy nanogenerators have been prepared to convert the thermal energy in electrical energy with a temperature ramp, via the Seebeck effect [66]. Pyroelectricity in these nanogenerators is described as the temperature-reliant impulsive polarization in explicit anisotropic crystals. The voltage generated by these nanogenerators are very low in comparison to other, and the materials are also very limited.

1.3.1.4 HNG

Despite substantial developments in power density (output) and efficiency, the net electric power of nanogenerators is still limited. By coupling two or more types of nanogenerators and energy harvesters, hybridized nanogenerators are formed, which delivers a possible resolution to this problem [67]. This opens a new technique in the scavenging of multiple energies through different nanogenerators. PENG-TENG based hybrid nanogenerators have been emerging to be very popular due to their limitless output power capabilities. Yang et al. [68] firstly demonstrated the multiple coupled nanogenerator to achieve a superior amount of energy from the main configuration.

1.3.2 Self-powered sensors

As discussed earlier, TENG generates the highest output power among all Nanogenerators [69]. This is the core reason for selecting TENG to be a power source in the case of self-powered schemes developed and demonstrated in this thesis. With the advancement of the internet of things and smart cities, limitless sensors will be positioned on different types of sites, and most of them are in unapproachable locations like large-distance transmission lines, optical cables, gas and oil pipelines in remote areas and under the sea, forests, etc. Powering these sensors in remote areas is a very challenging task [69–71]. Power supply using cable is also a very challenging task for

these areas and lots of resources get wasted. Batteries as power supply unit is another option, but it has some limitations. These batteries have a limited amount of service life and they discharge very fast. Usage of batteries for such inaccessible areas is not a cost-effective approach. These are the reasons for the requirement of such types of sensors that do not require any peripheral power source. These sensors must possess a cost-effective fabrication and limitless service life with long-term stability.

As the name advocates, Self-powered sensors are those sensors which operate without utilization of an external power source [70,72,73]. The self-powered TENG-based system harvests ambient mechanical energy like human motion, water waves, wind, rain drops etc. to operate itself. The objective of this is to prepare it proficient to function self-sufficiently and wirelessly. Several TENG-based self-powered motion sensors [73,74], fluid sensors [75,76], gas sensors [73,77] etc. have been developed to demonstrate its wide range of applications. Based on the working principle, the self-powered sensors utilizing TENG are categorized in 2 types [78]: **(1)** Self-powered Active sensors, and **(2)** Self-powered passive sensors.

1.3.2.1 Self-powered Active sensors

When the external entity (Gas, chemical, pressure etc.), is directly applied to the nanogenerators and the output power increases or decreases after reacting to these external agents [79]. Then this whole setup is known as active self-powered sensing as they do not require any external loading resistance to sense these agents. The main advantage of these sensors is, that they sense the required external entity directly and they are a little cost-effective than passive sensors. As TENG possess 2 tribo layers, When TENG-based active sensors are for example exposed to a gas, chemisorption occurs on one layer. Based on the material on another layer in TENG, receiving or donating of an electron occurs [80]. This changes the output voltage or current of the system. As the concentration or intensity of these external agents change, a corresponding change in output occurs.

1.3.2.2 Self-powered passive sensors

When an external resistive film is connected to the TENG and the external agents (Gas, chemical, pressure etc.) are applied to this resistive film, not on the

nanogenerator. Based on the kind of resistive film (p-type or n-type) and the type of external entity applied, the resistance of the external resistive film increases or decreases [81]. The voltage drop across this film then also increases or decreases accordingly. This type of sensing is called passive self-powered sensing as the nanogenerator does not sense the external agents directly [78,82]. Advantages of these sensors are the fabrication of sensing film on any surface, cost-effectiveness and a wide range of materials for sensing.

1.4 Sensing mechanism of conventional resistive based sensor and self-powered sensor

Although there is a variety of sensors available like optical, acoustic, and capacitive but resistive types of sensors are mostly preferred because of the vast area of selection of materials and the need for less costly detection instruments. These resistive sensors change their resistance when external agents like light, gas, and chemicals are exposed to these films. The basic mechanism of resistive-based Photo, Gas, Light enhanced gas sensors and corresponding self-powered sensing of these external agents. As discussed earlier self-powered sensing is preferred by the research community because of its highly responsive, extremely stable and ultra-fast sensing nature. Here we will also discuss the comparative analysis of both types of sensors (resistive and self-powered sensors). The basic difference in resistive and self-powered sensor is shown in Fig. 1.4.

1.4.1 Photo sensors and mechanism of Resistive Photo sensor

Photo sensors (or photo detectors) are those sensors which sense the change the intensity of incident light (UV, Visible or other). The sensors can detect the change via variation in electrical resistance of the film, change in intensity (optical), change in polarization etc. Resistive Photo sensors are the simplest and most cost-effective among all of them.

In resistive photo sensors, the resistance of the film decreases upon the application of light of a particular wavelength on the film. When the resistive film is unveiled to the air, O_2 molecules present in the surroundings get chemically adsorbed

on the upper exterior of the film by attracting conduction band electrons and creating O_2^- ions as:

$$O_2\ (ads) + e^- \leftrightarrow O_2^-(ads) \qquad (1.2)$$

When photons hit the surface, it generates electron-hole duos **[hυ → e^- + h^+]**. On irradiance of the film, some electrons, receive satisfactory energy for passing over the potential wall employing an electronic transition from valance band to the conduction band. These holes, which are photogenerated associate with O_2^- ions and translates in O_2 molecule.

$$h^+(h\upsilon) + O_2^- \rightarrow O_2\ (Des.) \qquad (1.3)$$

These O_2 molecules lastly go through desorption from the film. The residual uncoupled electron results in a reduction in resistance of the material. With the light exposure period, further electron-hole sets are produced and create a reduction in the film resistance. However, as soon as the illumination is off, O_2 molecules begin to adsorb on the film and produce O_2^- ions. This results in the increment of electrical resistance because of the decrement in surface electrons by adsorption.

1.4.2 Gas sensors and mechanism of Resistive gas sensor

Gas sensor is a sort of chemical sensor that exhibits the variation in its physical properties upon the introduction of the gaseous molecules that is desirable to be sensed. There are various kinds of gas sensors like electrochemical gas sensors, acoustic gas Sensors, colorimetric gas sensors, resistive gas sensors, optical gas sensors etc. [83,84].

The principle behind the working of a resistive gas sensor is the deviation in electrical resistance of a material upon application of the desired gas. The resistance variation is noted as output and the different sensing properties are widely calculated from the data [83].

1.4.2.1 Mechanism of Resistive LPG gas sensing

LPG is an extremely combustive gas with an assortment of hydrocarbons, mainly butane and propane. It is extensively used as a fuel in industrial and domestic

applications. Despite being harmful and extremely combustible, LPG is the most extensively used gas [85]. Hence it is crucial to be detected in the prior stages of the leakage below the lower explosion limit (LEL) [86].

When the sensing film gets in interaction with the air, oxygen molecules Chemi-adsorbed to the film. The surrounding oxygen molecules react with the electrons of conduction band available on the material surface as follows:

$$O_2\,(\text{atmosphere}) + e^-\,(\text{film surface}) \rightarrow O_2^-\,(\text{chemisorbed}) \qquad (1.4)$$

As a result of the chemisorption of O_2 on the sensing element, the electron concentration on the material decreases, this causes enhancement in the resistance of the material. This resistance is designated as the resistance of the material in air, R_a.

After that, when LPG is announced to the material, it reacts with the adsorbed oxygen ions. LPG is comprised of hydrocarbons which chemically interact with the surface-bound oxygen anions and generates water and other gases following the reaction mentioned as below [86,87]:

$$C_nH_{2n+2} + O_2^- \rightarrow C_nH_{2n}O + H_2O + e^- \qquad (1.5)$$

If the detecting material is n-type, then the freshly generated electrons upsurge the total number of the majority charge carriers (electrons) present on the film, which reduces the film resistance. Conversely, if the film is p-type, the formed electrons combine with the majority charge carriers i.e. holes, which additionally boosts the film resistance. The variation in resistance becomes steady as soon as the production of the above-stated products halts.

1.4.2.2 Mechanism of Resistive photo enhanced LPG sensing

Photo enhanced gas sensing is a newly discovered technique to enhance the sensor response and sensitivity of gas sensors. This technique is a combination of the mechanism described in sections 1.4.1 and 1.4.2.1. In this technique, when a material is treated with light of particular energy, it stimulates electrons present in the valence band, which then led in the direction of the conduction band departing holes behind. Thus, many electron-hole pairs are formed in the material, which upsurges the electrical

conductivity significantly. Due to the generation of fresh electrons, more oxygen molecules get chemically adsorbed on the film surface. Hence, the amount of the O_2^- ions produced rises in illumination. When LPG is uncovered inside the sensing chamber, it reacts with added O_2^- ions than before and generates more electrons. These generated electrons then recombine with holes and increase the resistance (for p-type) of the sample quickly [88,89].

1.4.3 Mechanism of TENG based Self-powered Sensor

The TENG based self-powered passive sensing mechanism is common for all types of sensors (photo, gas, light enhanced self-powered gas sensor). In this self-powered system, a resistive film is attached with TENG in series connection, and the drop of voltage across this film is measured by measuring devices like (an electrometer or Digital CRO). The input voltage from TENG acts as an input for this resistive film.

When external agents like light, gas (here LPG), or any chemical was exposed to this resistive film, the resistance of the film changes (increase or decrease) subjected to the type of film (n-type or p-type) and nature of the external agent. These self-powered sensors function on the conception of the division of voltage. If R_2 acts as a resistance of sensing element, R_1 is the internal resistance of the electrical circuit, V_{IN} is the maximum output voltage fed to the resistive film R_2, and then voltage drop through R_2:

$$\mathbf{V_{OUT}} = \{\boldsymbol{R_2}/(\boldsymbol{R_1} + \boldsymbol{R_2})\} \times \mathbf{V_{IN}} \qquad \textbf{(1.6)}$$

Eqn. 1.6 demonstrates that the output voltage (V_{OUT}) through the sensing film is proportionate with R_2. If R_2 varies significantly, the resultant V_{OUT} would also vary. If the resistance of resistive sensing film R_2 rises, the voltage drop through the R_2 also increases and vice versa ($V = I \times R$).

1.5 Sensor parameters attributed to resistive and self-powered sensor

To judge the effectiveness of a sensor, the following parameters should be calculated [87, 91–93] and compared with previous reported results:

a) **Sensor Response (SR):** When an external agent like gas, light or chemical is dropped onto the sensor, one of the output continuously change. The sensor response of a sensing device is specified as the ratio of the maximum value of output (electrical resistance, voltage, or current) with values of output at different concentrations of an external agent. For example, sensor response for chemiresistive LPG sensing is specified as the ratio of the film resistance in the exposure of that LPG concentration (R_g), and the resistance of the film in the air (R_a), i.e.,

$$\mathbf{SR} = \frac{\mathbf{R_g}}{\mathbf{R_a}} \qquad \mathbf{(1.7)}$$

b) **Sensitivity:** The sensitivity of an sensor can be defined as the sensor response per unit concentration of an external agent, and can be evaluated by determining the slope of the sensor response versus the concentration curve.

c) **Response Time:** The time occupied by the sensing device to attain 90% of the maximum output value after the addition of external agents in the sensing chamber is known as the response time.

d) **Recovery Time:** The time needed by the sensing device to attain 90% of the minimum output value after the removal of an external agent in the sensing chamber is, the recovery time of the sensor.

e) **Selectivity:** Selectivity is the comparative study of a sensor toward different analytes. For example, a sensor device is said to have decent selectivity towards a particular gas, when it displays a significantly higher sensor response for that particular gas compared to other gases.

f) **Repeatability:** It is described as the proficiency of a sensor to recreate identical output over a continuously repeating cycle of input agent like gas, light etc.

g) **Reproducibility or long-term stability:** A sensor can replicate the same output results after a long time without any changes in the sensing parameters.

1.6 Literature survey with problems experienced in traditional photo sensor, LPG sensors and Fluoride ion sensors

There are many problems already exists in available photo sensors or photo detectors, LPG sensor and Fluoride ion sensor, which are listed below:

- These devices lose their sensing behaviour with time because of mechanical and environmental degradation. After the distortion in internal matrix of the film, output performance is greatly reduced. The use of self-healable materials for photo sensors is missing.
- Most photodetectors are not self-powered in nature. They use some kind of power source like batteries to operate properly, which limits them to not to use on remote areas.
- The sensor response and responsivity are very low, while response and recovery time are also very high for existing materials.
- Most of the sensors are very costly because of the usage of expensive materials like CNT, graphene etc. Ferrites, which are abundant on the earth's surface was never explored before for photodetector purposes.

Table 1.2 describes the works reported before in Photo sensing areas:

Table 1.2 Literature survey of recent photo sensing devices.

S. No.	Sensing material	Self-healing property	Self-powered Nature	Response/Recovery time (s)	Responsivity (RES)/ Sensor Response (SR)	Ref.
1	MoS_2/ZnS	Not present	Not present	22	9.50×10^{-6}	[93]
2	Nanocrystalline silicon thin film	Not present	Not present	4.92/4.06	-	[94]
3	ZnO Nanowire	Not present	Not present	20/20	-	[95]
4	Boron	Not present	Not present	1.8	91.7×10^{-6}	[96]
5	MoS_2/ZnO	Not present	Not present	55	2.7	[97]
6	Polypyrrole/SnO_2	Not present	Not present	21/24.5	-	[98]
7	$Ti_2C_2T_x/TiO_2$	Not present	Not present	2.54	6×10^{-3}	[99]
8	Black Phosphorus	Not present	Not present	200	9×10^4	[100]
9	MoS_2	Not present	Not present	13	10^3	[101]
10	Graphene	Not present	Not present	269	0.11	[102]
11	Carbon quantum dot/MoS_2	Not present	Not present	570	18.12×10^{-3}	[103]
12	WSe_2	Not present	Not present	900/2000	0.92	[104]

13	Methylammonium lead iodide perovskite/graphene	Not present	Not present	250/530	115	[105]
14	PMMA/MoS_2	Not present	Not present	12 $\times10^3$/19$\times10^3$	0.2 $\times10^{-3}$	[106]
15	InSe	Not present	Not present	1000/1000	3.9	[107]
16	ZnO nanorod/Graphene	Not present	Not present	300/500	84.94	[108]
17	MoS_2 nanosheet	Not present	Present	0.32/0.36	-	[109]
18	$CsPbI_3$-PVDF	Not present	Present	2.4/1.1	0.3$\times10^{-3}$	[110]
19	Graphene/Imidazolium-based norbornene polymer	Present	Not present	0.91/0.92	93 $\times10^{-6}$	[111]
20	ZnS/Cu/PDMS	Present	Not present	0.042/2.67	-	[112]

Note: $\boldsymbol{RES = \frac{I_{light} - I_{dark}}{AP}}$, $\boldsymbol{SR = \frac{\Delta R}{R_{light}} = \frac{V_{dark}}{V_{light}}}$

Table 1.3 pronounces the works reported before in LPG sensing:

Table 1.3 Literature survey of recent LPG sensing devices.

S. No.	**Sensing material and Operating temperature**	**Concentration**	**Self-healing property**	**Self-powered Nature**	**Response/Recovery time (s)**	**Sensor Response (SR)/% Sensor Response**	**Ref.**
1	Pd-ZnO (RT)	2600 ppm	Not present	Not present	80/240	—/84%	[113]
2	Li-$CuFe_2O_4$ (RT)	4.0 vol. %	Not present	Not present	162/1161.6	—/83.82%	[114]
3	$LaNbO_4$ (250 °C)	500 ppm	Not present	Not present	25/100	—/80 %	[115]
4	$CuFe_2O_4$ (RT)	5.0 vol. %	Not present	Not present	150/510	—/57 %	[116]
5	$ZnCo_2O_4$ (350 °C)	50 ppm	Not present	Not present	85/75	72/—	[117]
6	$CdFe_2O_4$-PANI (RT)	1000 ppm	Not present	Not present	50/110	—/50.83 %	[118]
7	$LaFeO_3$ (RT)	5000 ppm	Not present	Not present	50/350	—/394 %	[119]
8	CuO-ZnO (350 °C)	1000 ppm	Not present	Not present	10/16	140/—	[120]
9	$CuFe_2O_4$ (RT)	5.0 vol. %	Not present	Not present	30/200	—/2.6 %	[121]
10	$BaTiO_3$ (RT)	5.0 vol. %	Not present	Not present	30/60	—/250 %	[92]

11	Ag-In_2O_3 (400 °C)	50 ppm	Not present	Not present	6/30	16.53/—	[122]
12	Sn-$CuFe_2O_4$ (RT)	2.0 vol. %	Not present	Not present	32/111	—/78.78 %	[123]
13	CdO (425 °C)	0.16 vol. %	Not present	Not present	30/60	—/34.11 %	[124]
14	$ZnFe_2O_4$ (375 °C)	2000 ppm	Not present	Not present	35/55	—/55 %	[125]
15	α- Fe_3O_4 (300 °C)	500 ppm	Not present	Not present	3/480	1746/—	[126]
16	$ZnSnO_3$/ZnO (RT)	8000 ppm	Not present	Present	72/88	—/83.23 %	[127]
17	$Ni_{0.4}Zn_{0.6}Fe_2O_4$ (RT)	2.0 vol. %	Present	Not present	28.08/52.46	2.15/—	[128]
18	$Mn_{0.7}Zn_{0.3}Fe_2O_4$ (250 °C)	2.0 vol. %	Not present	Not present	58/30	1.88/—	[129]
19	TiO_2 (RT)	4.0 vol. %	Not present	Not present	240/247.8	2.80/—	[130]
20	NiO (300 °C)	5000 ppm	Not present	Not present	94/92	—/72 %	[131]

Table 1.4 pronounces the works reported before in Fluoride ion sensing:

Table 1.4 Literature survey of recent fluoride sensing devices.

S. No.	**Sensing material**	**Sensing technique**	**Self-healing property**	**Self-powered Nature**	**Limit of detection (LOD)**	**Ref.**
1	7-O-tert-butyldiphenylsilyl-4-methylcoumarin	Fluorescence	Not present	Not present	0.2 mg/L	[132]
2	Zirconium-SPADNS	Colorimetric	Not present	Not present	0.2 mg/L	[133]
3	Near-cubic ceria@zirconia nanocages) and a xylenol	Colorimetric	Not present	Not present	0.06 mg/L	[134]
4	Anthracene	Colorimetric & fluorescent	Not present	Not present	8 µM	[135]
5	Azo dye	Colorimetric	Not present	Not present	10 µM	[136]
6	Benzohydrazide	UV-Visible	Not present	Not present	0.5 mg/L	[137]
7	Arylaldoximes	UV-Visible	Not present	Not present	0.7 mM	[138]
8	Boronic acid	Fluorescent	Not present	Not present	0.1 mg/L	[139]

9	Levofloxacin, nebivolol and efavirenz Drug	Selective electrode	Not present	Not present	7.89 µM	[140]
10	RBC bioreactor	Potentiometry	Not present	Not present	72 µM	[141]
11	Benzothiadiazole-bisphenol A	Colorimetric & fluorescent	Not present	Not present	9.13 µM	[142]
12	Boron-dipyrromethene	Colorimetric & fluorescent	Not present	Not present	52 µM	[143]
13	Calixarene	Photolumines cence	Not present	Not present	6.6 µM	[144]
14	Coumarin-carbohydrazone	Colorimetric & fluorescent	Not present	Not present	9.2 µM	[145]
15	Diketopyrrolopyrrole	Colorimetric & fluorescent	Not present	Not present	21 µM	[146]

1.7 Motivation and Objective of research work

As discussed above via literature survey, there is very little work is going on in the field of self-healable and self-powered sensors and energy devices. During the literature survey following challenges are found:

- **Low cost and easy synthesis process:** Most of self-healing process utilizes expensive precursors and equipment, which enhances the cost of the synthesis process. So, it is very vital to select cost-effective precursors to synthesize efficient healable materials.
- **High self-healing efficiency:** It is required to get 100% efficient self-healable material. The motive of the work to be performed here is to come close to this efficiency.
- **Simultaneous Self-healable and Self-powered properties:** There is almost negligible amount of work which had been performed globally to achieve Self-healable and Self-powered properties in a single device. The main objective of work performed here is to demonstrate such electronic devices and sensors.
- **Exploration of new techniques:** After successful synthesis, it is required to explore other sensing applications of healable materials.
- **Room temperature sensing:** It is very crucial for cost effective sensors to perform efficiently at room temperature. So, the motive of this research work is the fabrication self-healable sensors and electronic devices operable at room temperature.

1.8 Organization of thesis

There are five chapters in this thesis and a brief outline of its contents is as follows:

Chapter 1: This chapter describes the self-healing materials, their types, self-healing process, properties and synthesis method. A detailed literature investigation of earlier reported research in the area of self-healable electronic devices is discussed in this chapter. This chapter also describes the different applications of self-healing nanomaterials in electronic devices. Discussions on the working mechanism of different sensors like photo, gas and fluoride sensors, which are performed to demonstrate self-healable sensing devices have been presented. This chapter illuminates the main problems that emerged in the earlier reported studies.

Chapter 2: This chapter describes a procedure to prepare a dual-layered photodetection sensor, which can reoccupy its actual sensing performance after damage occurs in its physical structure. In this work two layers were used, microcapsule based bottom layer and upper NZF sensing layer. The NZF nanomaterial was synthesized via citrate acid aided sol-gel process, and was used as the resistive sensing film. Microcapsules of U-F infused with NZF and flaxseed oil core were prepared by oil emulsion method and used as a self-healing material. Via the easy fluidic motion of the flaxseed oil, NZF nanoparticles can fill in the damaged areas when the microcapsules are ruptured. In this layer, flaxseed oil acts as a transporting agent, which carries NZF nanoparticles toward the cracks. The sensing capability of the sample post healing was recreatable up to 98.5%.

Chapter 3: This chapter deals with the fabrication of self-recoverable and self-powered (without battery) visible light photodetector. In this chapter 2-D Polyaniline-Polypyrrole (PANI-PPY) nanoflakes were produced using low temperature aided oxidative polymerization method. The NFs formation was also explained in this chapter via thermal scission and surfactant effect. The most distinctive characteristic of this research is acetone-reinforced rapid self-restoration presented in Polyaniline-Polypyrrole (PANI-PPY) nanoflakes. The maximum healing efficiency of 99.8% was accomplished in this work.

Chapter 4: This chapter deals with visible light-enhanced LPG sensor, which is self-powered, self-healable, and based on PANI-PPY (2P) 2-dimensional nano-sheets. The material showed enhanced LPG detection below its LEL when irradiated with visible light at room temperature. The material was able to detect very low concentrations of LPG almost instantaneously with response/recovery times 172/580 ms. Self-healing ability was also efficaciously introduced in the TENG layer to recover its properties after any damage. The maximum healing efficiency of ~99.7% was achieved here in this work.

Chapter 5: This chapter describes a unique, cost-effective, and quick detection method of fluoride ions in water. The device is assembled using waste materials like BSR rubber, used polythene bags, and used plastic sheets, which validate the ability of device for producing energy from waste materials. The self-healing ability of PDMS/BSR-La nanocomposite shows fast healing in ~25 min with a healing efficiency of 99.9%, which is one of the unique features of this device. This unique chemisorption-based self-powered fluoride detection device shows a maximum sensor response of 12.10 and % sensor response of 1110 %, which is very high.

Chapter 6: This chapter gives the concluding observation and comparative analysis of all synthesized materials and fabricated devices. This chapter incorporates summarised information on the material characteristics, sensing output, and future scope of all the chapters mentioned previously.

References

[1] S.R. White, N.R. Sottos, P.H. Geubelle, J.S. Moore, M.R. Kessler, S.R. Sriram, E.N. Brown, S. Viswanathan, Autonomic healing of polymer composites, Nature. 409 (2001) 794–797.

[2] K.S. Toohey, N.R. Sottos, J.A. Lewis, J.S. Moore, S.R. White, Self-healing materials with microvascular networks, Nat. Mater. 6 (2007) 581–585.

[3] S. Utrera-Barrios, R. Verdejo, M.A. López-Manchado, M.H. Santana, Evolution of self-healing elastomers, from extrinsic to combined intrinsic mechanisms: A review, Mater. Horizons. 7 (2020) 2882–2902.

[4] S. Burattini, B.W. Greenland, D.H. Merino, W. Weng, J. Seppala, H.M. Colquhoun, W. Hayes, M.E. Mackay, I.W. Hamley, S.J. Rowan, A healable supramolecular polymer blend based on aromatic π-π stacking and hydrogen-bonding interactions, J. Am. Chem. Soc. 132 (2010) 12051–12058.

[5] C. Xu, J. Nie, W. Wu, L. Fu, B. Lin, Design of self-healable supramolecular hybrid network based on carboxylated styrene butadiene rubber and nano-chitosan, Carbohydr. Polym. 205 (2019) 410–419.

[6] L. Xiao, J. Shi, K. Wu, M. Lu, Self-healing supramolecular waterborne polyurethane based on host--guest interactions and multiple hydrogen bonds, React. Funct. Polym. 148 (2020) 104482.

[7] I.L. Hia, V. Vahedi, P. Pasbakhsh, Self-healing polymer composites: Prospects, challenges, and applications, Polym. Rev. 56 (2016) 225–261.

[8] Y.C. Yuan, X.J. Ye, M.Z. Rong, M.Q. Zhang, G.C. Yang, J.Q. Zhao, Self-healing epoxy composite with heat-resistant healant, ACS Appl. Mater.& Interfaces. 3 (2011) 4487–4495.

[9] H. Zhang, J. Yang, Development of self-healing polymers via amine--epoxy chemistry: II. Systematic evaluation of self-healing performance, Smart Mater. Struct. 23 (2014) 65004.

[10] E.L. Kirkby, J.D. Rule, V.J. Michaud, N.R. Sottos, S.R. White, J.-A.E. Månson, Embedded shape-memory alloy wires for improved performance of self-healing polymers, Adv. Funct. Mater. 18 (2008) 2253–2260.

[11] L. Yuan, S. Huang, A. Gu, G. Liang, F. Chen, Y. Hu, S. Nutt, A cyanate ester/microcapsule system with low cure temperature and self-healing capacity, Compos. Sci. Technol. 87 (2013) 111–117.

[12] G.J. Williams, I.P. Bond, R.S. Trask, Compression after impact assessment of self-healing CFRP, Compos. Part A Appl. Sci. Manuf. 40 (2009) 1399–1406.

[13] G. Ye, Z. Song, T. Yu, Q. Tan, Y. Zhang, T. Chen, C. He, L. Jin, N. Liu, Dynamic Ag--N Bond Enhanced Stretchable Conductor for Transparent and Self-Healing Electronic Skin, ACS Appl. Mater. & Interfaces. 12 (2019) 1486–1494.

[14] J.-B. Hou, X.-Q. Zhang, D. Wu, J.-F. Feng, D. Ke, B.-J. Li, S. Zhang, Tough

self-healing elastomers based on the host--guest interaction of polycyclodextrin, ACS Appl. Mater. & Interfaces. 11 (2019) 12105–12113.

[15] C. Lv, K. Zhao, J. Zheng, A Highly Stretchable Self-Healing Poly (dimethylsiloxane) Elastomer with Reprocessability and Degradability, Macromol. Rapid Commun. 39 (2018) 1700686.

[16] X. Dai, Y. Du, Y. Wang, Y. Liu, N. Xu, Y. Li, D. Shan, B. Bin Xu, J. Kong, Stretchable self-healing polymeric networks with recyclability and dual responsiveness, ACS Appl. Polym. Mater. 2 (2020) 1065–1072.

[17] A. Rekondo, R. Martin, A.R. de Luzuriaga, G. Cabañero, H.J. Grande, I. Odriozola, Catalyst-free room-temperature self-healing elastomers based on aromatic disulfide metathesis, Mater. Horizons. 1 (2014) 237–240.

[18] T. Li, Z. Xie, J. Xu, Y. Weng, B.-H. Guo, Design of a self-healing cross-linked polyurea with dynamic cross-links based on disulfide bonds and hydrogen bonding, Eur. Polym. J. 107 (2018) 249–257.

[19] S. Yang, S. Wang, X. Du, Z. Du, X. Cheng, H. Wang, Mechanically robust self-healing and recyclable flame-retarded polyurethane elastomer based on thermoreversible crosslinking network and multiple hydrogen bonds, Chem. Eng. J. 391 (2020) 123544.

[20] H. Yan, S. Dai, Y. Chen, J. Ding, N. Yuan, A high stretchable and self--healing silicone rubber with double reversible bonds, ChemistrySelect. 4 (2019) 10719–10725.

[21] Y. Peng, Y. Yang, Q. Wu, S. Wang, G. Huang, J. Wu, Strong and tough self-healing elastomers enabled by dual reversible networks formed by ionic interactions and dynamic covalent bonds, Polymer (Guildf). 157 (2018) 172–179.

[22] Y. Zuo, Y. Zhang, T. Yang, Z. Gou, W. Lin, Polysiloxane-based two-photon fluorescent elastomers with superior mechanical and self-healing properties and their application in bioimaging, New J. Chem. 42 (2018) 14281–14289.

[23] S. Stein, A. Mordvinkin, B. Voit, H. Komber, K. Saalwächter, F. Böhme, Self-healing and reprocessable bromo butylrubber based on combined ionic cluster formation and hydrogen bonding, Polym. Chem. 11 (2020) 1188–1197.

[24] W. Yao, X. Chen, Q. Tian, C. Luo, X. Zhang, H. Peng, W. Wu, Directly printing of upconversion fluorescence-responsive elastomers for self-healable optical application, Chem. Eng. J. 384 (2020) 123375.

[25] N.Y. Abu-Thabit, Chemical oxidative polymerization of polyaniline: A practical approach for preparation of smart conductive textiles, J. Chem. Educ. 93 (2016) 1606–1611.

[26] A. Dehghanghadikolaei, J. Ansary, R. Ghoreishi, Sol-gel process applications: A mini-review, Proc. Nat. Res. Soc. 2 (2018) 2008–2029.

[27] V. Forti, C.P. Baldé, R. Kuehr, G. Bel, The Global E-waste Monitor 2020:

Quantities, Flows, and the Circular Economy Potential, United Nations Univ. (UNU)/United Nations Inst. Train. Res. – Co-Hosted SCYCLE Program. Int. Telecommun. Union Int. Solid Waste Assoc. (ISWA), Bonn/Geneva/Rotterdam. (2020) 1–119.

[28] B.H. Robinson, E-waste: an assessment of global production and environmental impacts, Sci. Total Environ. 408 (2009) 183–191.

[29] F. Lang, N.H. Nickel, J. Bundesmann, S. Seidel, A. Denker, S. Albrecht, V. V Brus, J. Rappich, B. Rech, G. Landi, others, Radiation hardness and self-healing of perovskite solar cells, Adv. Mater. 28 (2016) 8726–8731.

[30] Y. Yu, F. Zhang, H. Yu, Self-healing perovskite solar cells, Sol. Energy. 209 (2020) 408–414.

[31] Y. Zhao, J. Wei, H. Li, Y. Yan, W. Zhou, D. Yu, Q. Zhao, A polymer scaffold for self-healing perovskite solar cells, Nat. Commun. 7 (2016) 1–9.

[32] B.P. Finkenauer, Y. Gao, X. Wang, Y. Tian, Z. Wei, C. Zhu, D.J. Rokke, L. Jin, L. Meng, Y. Yang, others, Mechanically robust and self-healable perovskite solar cells, Cell Reports Phys. Sci. 2 (2021) 100320.

[33] K. Chu, B.G. Song, H.-I. Yang, D.-M. Kim, C.S. Lee, M. Park, C.-M. Chung, Smart Passivation Materials with a Liquid Metal Microcapsule as Self-Healing Conductors for Sustainable and Flexible Perovskite Solar Cells, Adv. Funct. Mater. 28 (2018) 1800110.

[34] J.H. Lee, R. Hinchet, S.K. Kim, S. Kim, S.-W. Kim, Shape memory polymer-based self-healing triboelectric nanogenerator, Energy & Environ. Sci. 8 (2015) 3605–3613.

[35] W. Xu, L.-B. Huang, J. Hao, Fully self-healing and shape-tailorable triboelectric nanogenerators based on healable polymer and magnetic-assisted electrode, Nano Energy. 40 (2017) 399–407.

[36] K. Parida, G. Thangavel, G. Cai, X. Zhou, S. Park, J. Xiong, P.S. Lee, Extremely stretchable and self-healing conductor based on thermoplastic elastomer for all-three-dimensional printed triboelectric nanogenerator, Nat. Commun. 10 (2019) 1–9.

[37] H. Wang, B. Zhu, W. Jiang, Y. Yang, W.R. Leow, H. Wang, X. Chen, A mechanically and electrically self-healing supercapacitor, Adv. Mater. 26 (2014) 3638–3643.

[38] H. Sun, X. You, Y. Jiang, G. Guan, X. Fang, J. Deng, P. Chen, Y. Luo, H. Peng, Self-healable electrically conducting wires for wearable microelectronics, Angew. Chemie. 126 (2014) 9680–9685.

[39] Y. Zhao, Y. Zhang, H. Sun, X. Dong, J. Cao, L. Wang, Y. Xu, J. Ren, Y. Hwang, I.H. Son, others, A self-healing aqueous lithium-ion battery, Angew. Chemie Int. Ed. 55 (2016) 14384–14388.

[40] Y. Wu, L. Huang, X. Huang, X. Guo, D. Liu, D. Zheng, X. Zhang, R. Ren, D.

Qu, J. Chen, A room-temperature liquid metal-based self-healing anode for lithium-ion batteries with an ultra-long cycle life, Energy & Environ. Sci. 10 (2017) 1854–1861.

[41] T.-P. Huynh, H. Haick, Self-healing, fully functional, and multiparametric flexible sensing platform, Adv. Mater. 28 (2016) 138–143.

[42] T. Wang, Y. Zhang, Q. Liu, W. Cheng, X. Wang, L. Pan, B. Xu, H. Xu, A self-healable, highly stretchable, and solution processable conductive polymer composite for ultrasensitive strain and pressure sensing, Adv. Funct. Mater. 28 (2018) 1705551.

[43] C.S. Luo, P. Wan, H. Yang, S.A.A. Shah, X. Chen, Healable transparent electronic devices, Adv. Funct. Mater. 27 (2017) 1606339.

[44] J. Wu, Z. Wu, H. Xu, Q. Wu, C. Liu, B.-R. Yang, X. Gui, X. Xie, K. Tao, Y. Shen, others, An intrinsically stretchable humidity sensor based on anti-drying, self-healing and transparent organohydrogels, Mater. Horizons. 6 (2019) 595–603.

[45] H. Jin, T.P. Huynh, H. Haick, Self-Healable Sensors Based Nanoparticles for Detecting Physiological Markers via Skin and Breath: Toward Disease Prevention via Wearable Devices, Nano Lett. 16 (2016) 4194–4202.

[46] S. Li, Y. Zhang, Y. Wang, K. Xia, Z. Yin, H. Wang, M. Zhang, X. Liang, H. Lu, M. Zhu, others, Physical sensors for skin-inspired electronics, InfoMat. 2 (2020) 184–211.

[47] A. Hatamie, S. Angizi, S. Kumar, C.M. Pandey, A. Simchi, M. Willander, B.D. Malhotra, Textile based chemical and physical sensors for healthcare monitoring, J. Electrochem. Soc. 167 (2020) 37546.

[48] J. Janata, Chemical sensors, Anal. Chem. 64 (1992) 196–219.

[49] X.-J. Huang, Y.-K. Choi, Chemical sensors based on nanostructured materials, Sensors Actuators B Chem. 122 (2007) 659–671.

[50] Y. Jian, W. Hu, Z. Zhao, P. Cheng, H. Haick, M. Yao, W. Wu, Gas sensors based on chemi-resistive hybrid functional nanomaterials, Nano-Micro Lett. 12 (2020) 1–43.

[51] Z. Chen, C. Lu, Humidity sensors: a review of materials and mechanisms, Sens. Lett. 3 (2005) 274–295.

[52] M.A. Najeeb, Z. Ahmad, R.A. Shakoor, Organic thin-film capacitive and resistive humidity sensors: a focus review, Adv. Mater. Interfaces. 5 (2018) 1800969.

[53] B. Chen, T. Jiang, H. Fu, X. Qu, Z. Xu, S. Zheng, Ultrasensitive, rapid and selective sensing of hazardous fluoride ion in aqueous solution using a zirconium porphyrinic luminescent metal-organic framework, Anal. Chim. Acta. 1145 (2021) 95–102.

[54] M. Sebastian, A. Aravind, B. Mathew, Green silver nanoparticles based multi-technique sensor for environmental hazardous Cu (II) ion, Bionanoscience. 9 (2019) 373–385.

[55] N. Kaewnok, J. Sirirak, S. Jungsuttiwong, Y. Wongnongwa, A. Kamkaew, A. Petdum, W. Panchan, S. Sahasithiwat, T. Sooksimuang, A. Charoenpanich, others, Detection of hazardous mercury ion using [5] helicene-based fluorescence probe with "TurnON" sensing response for practical applications, J. Hazard. Mater. 418 (2021) 126242.

[56] S. Vigneshvar, C.C. Sudhakumari, B. Senthilkumaran, H. Prakash, Recent advances in biosensor technology for potential applications-an overview, Front. Bioeng. Biotechnol. 4 (2016) 11.

[57] Y. Fu, W. Zang, P. Wang, L. Xing, X. Xue, Y. Zhang, Portable room-temperature self-powered/active H2 sensor driven by human motion through piezoelectric screening effect, Nano Energy. 8 (2014) 34–43.

[58] Z.L. Wang, J. Song, Piezoelectric Nanogenerators Based on Zinc Oxide Nanowire Arrays, Science. 312 (2006) 242–246.

[59] F.R. Fan, Z.Q. Tian, Z. Lin Wang, Flexible triboelectric generator, Nano Energy. 1 (2012) 328–334.

[60] Y. Yang, W. Guo, K.C. Pradel, G. Zhu, Y. Zhou, Y. Zhang, Y. Hu, L. Lin, Z.L. Wang, Pyroelectric nanogenerators for harvesting thermoelectric energy, Nano Lett. 12 (2012) 2833–2838.

[61] B.J. Hansen, Y. Liu, R. Yang, Z.L. Wang, Hybrid nanogenerator for concurrently harvesting biomechanical and biochemical energy, ACS Nano. 4 (2010) 3647–3652.

[62] G. Zhu, B. Peng, J. Chen, Q. Jing, Z.L. Wang, Triboelectric nanogenerators as a new energy technology: from fundamentals, devices, to applications, Nano Energy. 14 (2015) 126–138.

[63] S. Niu, Z.L. Wang, Theoretical systems of triboelectric nanogenerators, Nano Energy. 14 (2015) 161–192.

[64] C. Wu, A.C. Wang, W. Ding, H. Guo, Z.L. Wang, Triboelectric nanogenerator: a foundation of the energy for the new era, Adv. Energy Mater. 9 (2019) 1802906.

[65] S. Rathore, S. Sharma, B.P. Swain, R.K. Ghadai, A critical review on triboelectric nanogenerator, in: IOP Conf. Ser. Mater. Sci. Eng. 377 (2018) 12186.

[66] H. Ryu, S.-W. Kim, Emerging pyroelectric nanogenerators to convert thermal energy into electrical energy, Small. 17 (2021) 1903469.

[67] K. Zhang, Y. Wang, Y. Yang, Structure design and performance of hybridized nanogenerators, Adv. Funct. Mater. 29 (2019) 1806435.

[68] Y. Feng, L. Zhang, Y. Zheng, D. Wang, F. Zhou, W. Liu, Leaves based triboelectric nanogenerator (TENG) and TENG tree for wind energy harvesting, Nano Energy. 55 (2019) 260–268.

[69] Y. Zhou, M. Shen, X. Cui, Y. Shao, L. Li, Y. Zhang, Triboelectric nanogenerator based self-powered sensor for artificial intelligence, Nano Energy. 84 (2021) 105887.

[70] Z. Li, Q. Zheng, Z.L. Wang, Z. Li, Nanogenerator-based self-powered sensors for wearable and implantable electronics, Research. 2020 (2020).

[71] R. Mondal, M.A.M. Hasan, R. Zhang, H. Olin, Y. Yang, Nanogenerators-Based Self-Powered Sensors, Adv. Mater. Technol. (2022) 2200282.

[72] X. Cao, Y. Xiong, J. Sun, X. Zhu, Q. Sun, Z.L. Wang, Piezoelectric Nanogenerators Derived Self-Powered Sensors for Multifunctional Applications and Artificial Intelligence, Adv. Funct. Mater. 31 (2021) 2102983.

[73] Z. LináWang, Triboelectric nanogenerators as new energy technology and self-powered sensors--Principles, problems and perspectives, Faraday Discuss. 176 (2014) 447–458.

[74] K. Dong, J. Deng, Y. Zi, Y.-C. Wang, C. Xu, H. Zou, W. Ding, Y. Dai, B. Gu, B. Sun, others, 3D orthogonal woven triboelectric nanogenerator for effective biomechanical energy harvesting and as self-powered active motion sensors, Adv. Mater. 29 (2017) 1702648.

[75] W. Wang, Y. Wu, Z. Chang, F. Chen, H. Wang, G. Gu, H. Zheng, G. Cheng, Z.L. Wang, Self-powered intelligent water meter for electrostatic scale preventing, rust protection, and flow sensor in a solar heater system, ACS Appl. Mater. & Interfaces. 11 (2019) 6396–6403.

[76] C. Chen, Z. Wen, A. Wei, X. Xie, N. Zhai, X. Wei, M. Peng, Y. Liu, X. Sun, J.T.W. Yeow, Self-powered on-line ion concentration monitor in water transportation driven by triboelectric nanogenerator, Nano Energy. 62 (2019) 442–448.

[77] D. Wang, D. Zhang, J. Guo, Y. Hu, Y. Yang, T. Sun, H. Zhang, X. Liu, Multifunctional poly (vinyl alcohol)/Ag nanofibers-based triboelectric nanogenerator for self-powered MXene/tungsten oxide nanohybrid NO_2 gas sensor, Nano Energy. 89 (2021) 106410.

[78] Z.L. Wang, J. Chen, L. Lin, Progress in triboelectric nanogenerators as a new energy technology and self-powered sensors, Energy & Environ. Sci. 8 (2015) 2250–2282.

[79] A.S.M.I. Uddin, G.S. Chung, A self-powered active hydrogen gas sensor with fast response at room temperature based on triboelectric effect, Sensors Actuators B Chem. 231 (2016) 601–608.

[80] Y. Zhao, X. Lai, P. Deng, Y. Nie, Y. Zhang, L. Xing, X. Xue, Pt/ZnO nanoarray nanogenerator as self-powered active gas sensor with linear ethanol sensing at

room temperature, Nanotechnology. 25 (2014) 115502.

[81] D. Zhang, Z. Xu, Z. Yang, X. Song, High-performance flexible self-powered tin disulfide nanoflowers/reduced graphene oxide nanohybrid-based humidity sensor driven by triboelectric nanogenerator, Nano Energy. 67 (2020) 104251.

[82] L. Xu, W. Xuan, J. Chen, C. Zhang, Y. Tang, X. Huang, W. Li, H. Jin, S. Dong, W. Yin, others, Fully self-powered instantaneous wireless humidity sensing system based on triboelectric nanogenerator, Nano Energy. 83 (2021) 105814.

[83] S.Z.N. Demon, A.I. Kamisan, N. Abdullah, S.A.M. Noor, O.K. Khim, N.A.M. Kasim, M.Z.A. Yahya, N.A.A. Manaf, A.F.M. Azmi, N.A. Halim, Graphene-based materials in gas sensor applications: A review, Sens. Mater. 32 (2020) 759–777.

[84] N. Yamazoe, Toward innovations of gas sensor technology, Sensors Actuators B Chem. 108 (2005) 2–14.

[85] S. Goutham, N. Jayarambabu, C. Sandeep, K.K. Sadasivuni, D.S. Kumar, K.V. Rao, Resistive room temperature LPG sensor based on a graphene/CdO nanocomposite, Microchim. Acta. 186 (2019) 62.

[86] M. Singh, B.C. Yadav, A. Ranjan, R.K. Sonker, M. Kaur, Detection of liquefied petroleum gas below lowest explosion limit (LEL) using nanostructured hexagonal strontium ferrite thin film, Sensors Actuators B Chem. 249 (2017) 96–104.

[87] R.A.B. John, A.R. Kumar, A review on resistive-based gas sensors for the detection of volatile organic compounds using metal-oxide nanostructures, Inorg. Chem. Commun. 133 (2021) 108893.

[88] D. Haridas, A. Chowdhuri, K. Sreenivas, V. Gupta, Enhanced room temperature response of SnO_2 thin film sensor loaded with Pt catalyst clusters under UV radiation for LPG, Sensors Actuators B Chem. 153 (2011) 152–157.

[89] A. Bhaduri, S. Singh, K.B. Thapa, B.C. Yadav, Visible light-induced, highly responsive, below lower explosive limit (LEL) LPG sensor based on hydrothermally synthesized barium hexaferrite nanorods, Sensors Actuators B Chem. 348 (2021).

[90] M. Singh, B.C. Yadav, U. Kumar, A. Ranjan, R. Srivastava, M. Kaur, Fabrication of nanostructured lead-free bismuth sodium titanatethin film and its liquefied petroleum gas sensing, Sensors Actuators A Phys. 301 (2020) 111765.

[91] A. Paliwal, A. Sharma, M. Tomar, V. Gupta, Carbon monoxide (CO) optical gas sensor based on ZnO thin films, Sensors Actuators B Chem. 250 (2017) 679–685.

[92] M. Singh, B.C. Yadav, A. Ranjan, M. Kaur, S.K. Gupta, Synthesis and characterization of perovskite barium titanate thin film and its application as LPG sensor, Sensors Actuators b Chem. 241 (2017) 1170–1178.

[93] P.T. Gomathi, P. Sahatiya, S. Badhulika, Large-Area, Flexible Broadband

Photodetector Based on ZnS–MoS2 Hybrid on Paper Substrate, Adv. Funct. Mater. 27 (2017) 1701611.

[94] R.K. Tripathi, O.S. Panwar, I. Rawal, B.P. Singh, B.C. Yadav, Study on nanocrystalline silicon thin films grown by the filtered cathodic vacuum arc technique using boron doped solid silicon for fast photo detectors, J. Taiwan Inst. Chem. Eng. 86 (2018) 185–191.

[95] X. Yang, Z. Chen, X. Xie, X. Xu, W. Xiong, W. Li, S. Li, Enhanced response speed of ZnO nanowire photodetector by coating with photoresist, J. Nanomater. 2016 (2016).

[96] D. Ma, R. Wang, J. Zhao, Q. Chen, L. Wu, D. Li, L. Su, X. Jiang, Z. Luo, Y. Ge, others, A self-powered photodetector based on two-dimensional boron nanosheets, Nanoscale. 12 (2020) 5313–5323.

[97] M.-A. Kang, S. Kim, I.-S. Jeon, Y.R. Lim, C.-Y. Park, W. Song, S.S. Lee, J. Lim, K.-S. An, S. Myung, Highly efficient and flexible photodetector based on MoS 2--ZnO heterostructures, RSC Adv. 9 (2019) 19707–19711.

[98] I. Rawal, R.K. Tripathi, O.S. Panwar, Easy synthesis of organic--inorganic hybrid nanomaterials: study of DC conduction mechanism for light dependent resistors, RSC Adv. 6 (2016) 31540–31550.

[99] J. Chen, Z. Li, F. Ni, W. Ouyang, X. Fang, Bio-inspired transparent MXene electrodes for flexible UV photodetectors, Mater. Horizons. 7 (2020) 1828–1833.

[100] J. Wu, G.K.W. Koon, D. Xiang, C. Han, C.T. Toh, E.S. Kulkarni, I. Verzhbitskiy, A. Carvalho, A.S. Rodin, S.P. Koenig, others, Colossal ultraviolet photoresponsivity of few-layer black phosphorus, ACS Nano. 9 (2015) 8070–8077.

[101] J.F. Gonzalez Marin, D. Unuchek, K. Watanabe, T. Taniguchi, A. Kis, MoS2 photodetectors integrated with photonic circuits, Npj 2D Mater. Appl. 3 (2019) 1–6.

[102] P. Kang, M.C. Wang, P.M. Knapp, S. Nam, Photodetectors: Crumpled Graphene Photodetector with Enhanced, Strain-Tunable, and Wavelength-Selective Photoresponsivity, Adv. Mater. 28 (2016) 4565.

[103] P. Sahatiya, S.S. Jones, S. Badhulika, 2D MoS_2-carbon quantum dot hybrid based large area, flexible UV-vis-NIR photodetector on paper substrate, Appl. Mater. Today. 10 (2018) 106–114.

[104] Z. Zheng, T. Zhang, J. Yao, Y. Zhang, J. Xu, G. Yang, Flexible, transparent and ultra-broadband photodetector based on large-area WSe_2 film for wearable devices, Nanotechnology. 27 (2016) 225501.

[105] V.Q. Dang, G.-S. Han, T.Q. Trung, Y.-U. Jin, B.-U. Hwang, H.-S. Jung, N.-E. Lee, others, Methylammonium lead iodide perovskite-graphene hybrid channels in flexible broadband phototransistors, Carbon N. Y. 105 (2016) 353–361.

[106] F. Yu, M. Hu, F. Kang, R. Lv, Flexible photodetector based on large-area few-layer MoS2, Prog. Nat. Sci. Mater. Int. 28 (2018) 563–568.

[107] S.R. Tamalampudi, Y.-Y. Lu, R.K. U, R. Sankar, C.-D. Liao, C.-H. Cheng, F.C. Chou, Y.-T. Chen, High performance and bendable few-layered InSe photodetectors with broad spectral response, Nano Lett. 14 (2014) 2800–2806.

[108] S. Liu, Q. Liao, S. Lu, Z. Zhang, G. Zhang, Y. Zhang, Strain modulation in graphene/ZnO nanorod film schottky junction for enhanced photosensing performance, Adv. Funct. Mater. 26 (2016) 1347–1353.

[109] L. Han, M. Peng, Z. Wen, Y. Liu, Y. Zhang, Q. Zhu, H. Lei, S. Liu, L. Zheng, X. Sun, others, Self-driven photodetection based on impedance matching effect between a triboelectric nanogenerator and a MoS_2 nanosheets photodetector, Nano Energy. 59 (2019) 492–499.

[110] K. Maity, U. Pal, H.K. Mishra, P. Maji, P. Sadhukhan, Z. Mallick, S. Das, B. Mondal, D. Mandal, Piezo-phototronic effect in highly stable $CsPbI_3$-PVDF composite for self-powered nanogenerator and photodetector, Nano Energy. 92 (2022) 106743.

[111] C. An, F. Nie, R. Zhang, X. Ma, D. Wu, Y. Sun, X. Hu, D. Sun, L. Pan, J. Liu, Two-Dimensional Material-Enhanced Flexible and Self-Healable Photodetector for Large-Area Photodetection, Adv. Funct. Mater. 31 (2021) 2100136.

[112] S. Bin Choi, C.-J. Lee, C.J. Han, J.-W. Kang, C.-R. Lee, J.-W. Kim, Self-Healable Capacitive Photodetectors with Stretchability Based on Composite of ZnS: Cu Particles and Reversibly Crosslinkable Silicone Elastomer, Adv. Mater. Technol. 5 (2020) 2000327.

[113] M. Jabeen, A. Iqbal, R.V. Kumar, M. Ahmed, Pd-doped zinc oxide nanostructures for liquefied petroleum gas detection at low temperature, Sens. Bio-Sensing Res. 25 (2019) 100293.

[114] V. Manikandan, M. Singh, B.C. Yadav, J.C. Denardin, Fabrication of lithium substituted copper ferrite (Li-CuFe2O4) thin film as an efficient gas sensor at room temperature, J. Sci. Adv. Mater. Devices. 3 (2018) 145–150.

[115] C. Balamurugan, D.-W. Lee, A. Subramania, Preparation and LPG-gas sensing characteristics of p-type semiconducting $LaNbO_4$ ceramic material, Appl. Surf. Sci. 283 (2013) 58–64.

[116] S. Singh, B.C. Yadav, R. Prakash, B. Bajaj, others, Synthesis of nanorods and mixed shaped copper ferrite and their applications as liquefied petroleum gas sensor, Appl. Surf. Sci. 257 (2011) 10763–10770.

[117] S. Vijayanand, P.A. Joy, H.S. Potdar, D. Patil, P. Patil, Nanostructured spinel $ZnCo_2O_4$ for the detection of LPG, Sensors Actuators B Chem. 152 (2011) 121–129.

[118] S. Kotresh, Y.T. Ravikiran, S.K. Tiwari, S.C. Vijaya Kumari, Polyaniline--cadmium ferrite nanostructured composite for room-temperature liquefied

petroleum gas sensing, J. Electron. Mater. 46 (2017) 5240–5247.

[119] A.K. Yadav, R.K. Singh, P. Singh, Fabrication of lanthanum ferrite based liquefied petroleum gas sensor, Sensors Actuators B Chem. 229 (2016) 25–30.

[120] M.K. Deore, G.H. Jain, V.B. Gaikwad, LPG gas sensing properties of CuO loaded ZnO thick film resistors, Fifth Int. Conf. Sens. Technol., (2011) 233–238.

[121] S. Singh, B.C. Yadav, V.D. Gupta, P.K. Dwivedi, Investigation on effects of surface morphologies on response of LPG sensor based on nanostructured copper ferrite system, Mater. Res. Bull. 47 (2012) 3538–3547.

[122] K. Anand, J. Kaur, R.C. Singh, R. Thangaraj, Preparation and characterization of Ag-doped In_2O_3 nanoparticles gas sensor, Chem. Phys. Lett. 682 (2017) 140–146.

[123] V. Manikandan, M. Singh, B.C. Yadav, R.S. Mane, S. Vigneselvan, A. Mirzaei, J. Chandrasekaran, Room temperature LPG sensing properties of tin substituted copper ferrite (Sn- $CuFe_2O_4$) thin film, Mater. Chem. Phys. 240 (2020) 122265.

[124] D.M. Carballeda-Galicia, R. Castanedo-Perez, O. Jimenez-Sandoval, S. Jimenez-Sandoval, G. Torres-Delgado, C.I. Zuniga-Romero, High transmittance CdO thin films obtained by the sol-gel method, Thin Solid Films. 371 (2000) 105–108.

[125] J.Y. Patil, D.Y. Nadargi, J.L. Gurav, I.S. Mulla, S.S. Suryavanshi, Glycine combusted $ZnFe_2O_4$ gas sensor: Evaluation of structural, morphological and gas response properties, Ceram. Int. 40 (2014) 10607–10613.

[126] D. Patil, V. Patil, P. Patil, Highly sensitive and selective LPG sensor based on α-Fe_2O_3 nanorods, Sensors Actuators B Chem. 152 (2011) 299–306.

[127] Y. Fu, Y. Nie, Y. Zhao, P. Wang, L. Xing, Y. Zhang, X. Xue, Detecting Liquefied Petroleum Gas (LPG) at Room Temperature Using $ZnSnO_3$/ZnO Nanowire Piezo-Nanogenerator as Self-Powered Gas Sensor, ACS Appl. Mater. Interfaces. 7 (2015) 10482–10490.

[128] A. Bhaduri, S. Singh, R.K. Tripathi, U. Kumar, K.B. Thapa, B.C. Yadav, Healable, highly sensitive LPG sensor based on $Ni_{0.4}Zn_{0.6}Fe_2O_4$ nanohybrid grown by autocombustion process, Sensors Actuators B Chem. 327 (2021) 128840.

[129] M. Deepty, S. Ch, P.N. Ramesh, N.K. Mohan, M.S. Singh, C.L. Prajapat, A. Verma, D.L. Sastry, others, Evaluation of structural and dielectric properties of Mn^{2+}-substituted Zn-spinel ferrite nanoparticles for gas sensor applications, Sensors Actuators B Chem. 316 (2020) 128127.

[130] S.R. Sabhajeet, B.C. Yadav, R.K. Sonker, Sol-gel formed spherical nanostructured titania based liquefied petroleum gas sensor, AIP Conf. Proc.1953 (2018) 30078.

[131] S.U. Mutkule, S.T. Navale, V. V Jadhav, S.B. Ambade, M. Naushad, A.D. Sagar, V.B. Patil, F.J. Stadler, R.S. Mane, Solution-processed nickel oxide films and

their liquefied petroleum gas sensing activity, J. Alloys Compd. 695 (2017) 2008–2015.

[132] R. Chavali, N.S.K. Gunda, S. Naicker, S.K. Mitra, Rapid detection of fluoride in potable water using a novel fluorogenic compound 7-O-tert-butyldiphenylsilyl-4-methylcoumarin, Anal. Chem. Res. 6 (2015) 26–31.

[133] M. Mohapatra, S. Anand, B.K. Mishra, D.E. Giles, P. Singh, Review of fluoride removal from drinking water, J. Environ. Manage. 91 (2009) 67–77.

[134] S. Mukherjee, M. Shah, K. Chaudhari, A. Jana, C. Sudhakar, P. Srikrishnarka, M.R. Islam, L. Philip, T. Pradeep, Smartphone-based fluoride-specific sensor for rapid and affordable colorimetric detection and precise quantification at sub-ppm levels for field applications, ACS Omega. 5 (2020) 25253–25263.

[135] D. Udhayakumari, S. Velmathi, P. Venkatesan, S.-P. Wu, Anthracene coupled thiourea as a colorimetric sensor for F-/Cu^{2+} and fluorescent sensor for Hg^{2+}/picric acid, J. Lumin. 161 (2015) 411–416.

[136] C.H. Dos Santos, N.M. Uchiyama, I.A. Bagatin, Selective azo dye-based colorimetric chemosensor for F-, $CH3COO^-$and PO_4^{3-}, Spectrochim. Acta Part A Mol. Biomol. Spectrosc. 210 (2019) 355–361.

[137] A.N. Shetty, D.R. Trivedi, others, Colorimetric receptors for naked eye detection of inorganic fluoride ion in aqueous media using ICT mechanism, RSC Adv. 2 (2012) 10499–10504.

[138] J.-S. Chen, P.-W. Zhou, L. Zhao, T.-S. Chu, A DFT/TDDFT study of the excited state intramolecular proton transfer based sensing mechanism for the aqueous fluoride chemosensor BTTPB, RSC Adv. 4 (2014) 254–259.

[139] T. Nishimura, S.-Y. Xu, Y.-B. Jiang, J.S. Fossey, K. Sakurai, S.D. Bull, T.D. James, A simple visual sensor with the potential for determining the concentration of fluoride in water at environmentally significant levels, Chem. Commun. 49 (2013) 478–480.

[140] M.V.B. Krishna, S. V Rao, V.S.N. Murthy, D. Karunasagar, A simple UV-photolysis digestion method for the determination of fluoride in fluorine-containing drugs by ion-selective electrode and spectrophotometry techniques, Anal. Methods. 4 (2012) 1565–1572.

[141] R.B.R. Mesquita, I.C. Santos, M.F.F. Pedrosa, A.F. Duque, P.M.L. Castro, A.O.S.S. Rangel, Development of flow injection potentiometric methods for the off-line and on-line determination of fluoride to monitor the biodegradation of a monofluorophenol in two bioreactors, Talanta. 84 (2011) 1291–1297.

[142] S. Erdemir, O. Kocyigit, Reversible “OFF-ON” fluorescent and colorimetric sensor based benzothiazole-bisphenol A for fluoride in MeCN, Sensors Actuators B Chem. 221 (2015) 900–905.

[143] L. Wang, L. Li, D. Cao, Dual binding site assisted chromogenic and fluorogenic discrimination of fluoride and cyanide by boryl functionalized BODIPY, Sensors

Actuators B Chem. 228 (2016) 347–359.

[144] U. Baruah, N. Gogoi, G. Majumdar, D. Chowdhury, β-Cyclodextrin and calix [4] arene-25, 26, 27, 28-tetrol capped carbon dots for selective and sensitive detection of fluoride, Carbohydr. Polym. 117 (2015) 377–383.

[145] S. Biswas, M. Gangopadhyay, S. Barman, J. Sarkar, N.D.P. Singh, Simple and efficient coumarin-based colorimetric and fluorescent chemosensor for F- detection: an ON1-OFF-ON2 fluorescent assay, Sensors Actuators B Chem. 222 (2016) 823–828.

[146] X. Yang, L. Xie, R. Ning, X. Gong, Z. Liu, Y. Li, L. Zheng, G. Zhang, B. Gao, Y. Cui, others, A diketopyrrolopyrrole-based near-infrared sensor for selective recognition of fluoride ions, Sensors Actuators B Chem. 210 (2015) 784–794.

Chapter 2

Improved sensing behaviour of self-healable solar light photodetector based on core-shell type $Ni_{0.2}Zn_{0.8}Fe_2O_4$@ poly (Urea-Formaldehyde)

Here, a bi-layered, highly responsive, as well as self-healable photo sensor that is able to reinstate both of its internal configuration along with photo sensing characteristic after distortion, is described. This ferrite-based photodetector has extremely fast sensing capability and re-establishment property. Here dual-layered film is prepared, in which, the top most layer is made with $Ni_{0.2}Zn_{0.8}Fe_2O_4$ (NZF) sensing layer was prepared using citrate gel technique, while the bottom layer is of microcapsules made up of Urea-Formaldehyde (U-F) filled with NZF and flaxseed oil as core, and plays as self-healing layer that effectively repairs sensing characteristic of the film after deformation.

2.1. Introduction

Fossil fuels, coals etc. are non-renewable energy resources and will be depleted in the proximate future. The unceasing growth in population will bring the ingestion of more power sources [1]. The non-renewable energy sources are unable to satisfy these energy necessities. So, there will be a global dependency on conventional energy resources in the near future. To achieve sustainable growth, the conservation of electricity is as vital as its generation. Many research groups have been working on topics like batteries [4-6], superconductors [2,3], light dependent resistors (LDR) [7,8] to preserve electric power. Globally a gigantic extent of electric power is being wasted owing to unreasonable usage of certain equipment in the daytime. The unclear power conservation guidelines and highly expensive unmanned switches (e.g., light-dependent resistors) are the leading causes of the wastage of electric power [9,10]. The photodetector has the characteristic to alter its electrical resistance when the intensity of the applied light varies. While different nanomaterials are broadly investigated in this field [11-13], ferrites are the least explored materials in photodetection.

An additional serious complication in this perspective is the service life of electronic devices. The devices are unceasingly degrading with time due to frequent mechanical strain, corrosion, and damage while operating. Even slight damage in the structure can cause a vast variation in its output. Sometimes, it even causes complete failure of the entire device. This leads to a terrific yearly boost in electronic waste (E-waste). Roughly, e-waste of approximately 44.7 and 47 million metric tons was produced in 2016 and 2017 respectively [14]. Furthermore, e-waste produces stark impacts on the environment and health of humans. Mostly, the e-wastes comprise toxic and heavy metals (Cd, Hg, Pb etc.) [15] that infect the soil and natural sources of water which distresses all living creatures [16-18]. Recently, researchers are working on developing electronic appliences with self-healing capabilities that can redevelop their internal configurations and characteristics after any deformation. There is noteworthy progress in self-healable perovskite solar cells [22-24], nanogenerators [19-21], sensing devices [25-28], etc.

In the following work, we have pointed toward the concern of recovering the sensing behaviour of a solar light photosensor after mechanical distortion. NZF along with flaxseed oil coated with U-F polymeric shell was formed via the oil-in-water emulsion technique. The self-healing, along with the free-drifting competency of the flaxseed oil, has already been conveyed in many reports [29-32]. The entire preparation is very easy, simple and inexpensive. A photodetector that can recuperate its sensing characteristics after any structural distortion is well demonstrated here. The graphical representation of the working principle of the self-healing process is revealed in Fig. 2.1. A bi-layered, healable film, where the top layer was made with $Ni_{0.2}Zn_{0.8}Fe_2O_4$ (NZF) and the bottom layer with Urea-formaldehyde (U-F) microcapsule containing NZF and flaxseed oil. Taking advantage of the easy-flowing skill of flaxseed oil, NZF nanoparticles are able to fill in the damaged areas when the microcapsules are ruptured. Here flaxseed oil acts as a transporting agent, which carries NZF nanoparticles toward the cracks.

2.2. Experimental

2.2.1. $Ni_{0.2}Zn_{0.8}Fe_2O_4$ (NZF) synthesis

NZF nanomaterial was prepared through citrate acid-assisted sol-gel scheme. Hydrated metal nitrates (nickel nitrate, iron nitrate and zinc nitrate) in stoichiometric amount were added in DI and stirred magnetically at room temperature until a homogeneous mixture formed. Next, an aqueous solution of citric acid prepared at an equal molar ratio between the citric acid and the metal ions was included in the last concoction and blended in ambient temperature. In this synthesis process, citric acid is used for inducing chelation in order to achieve consistent distribution of metal cations. Afterwards, diluted ammonia in minute amount was added slowly in the (metal nitrate + citric acid) solution to increase the pH value from 2 to 8. The heat was then applied to the solution by applying an external temperature of ~100 °C until xerogel forms. Due to the presence of chelating agent, the gel starts igniting, and the dry xerogel speedily burns on its own and formed loose powder-like material. This nanopowder was then cooled down, rinsed multiple times, and treated at 600 °C for 2 hrs inside a tube furnace.

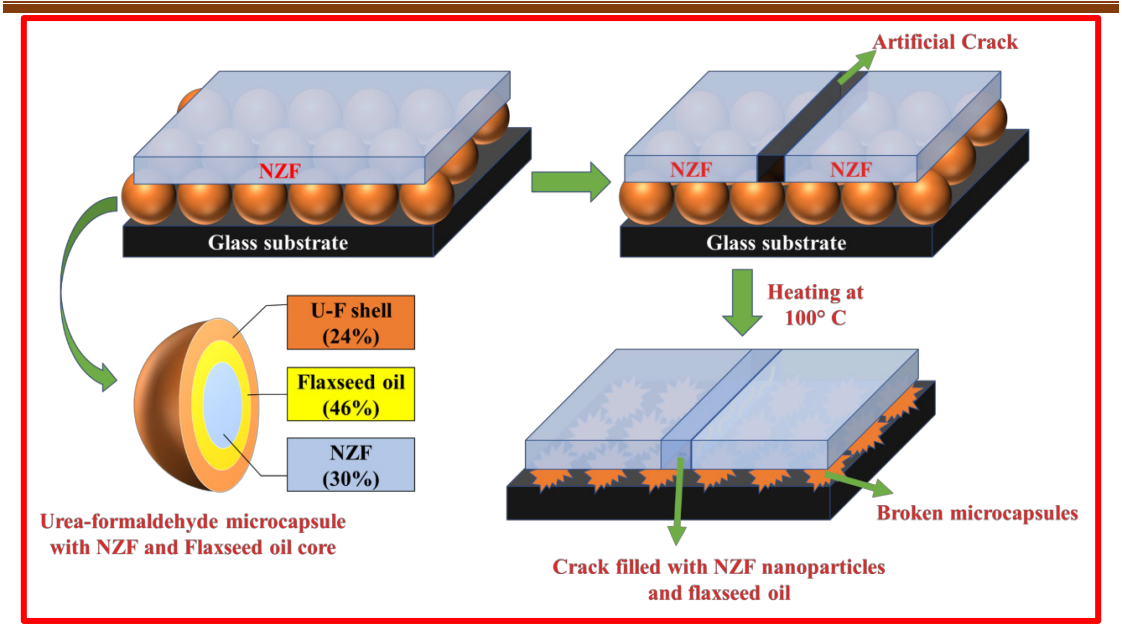

Fig. 2.1 Schematic diagram depicting the self-healing phenomenon in present work.

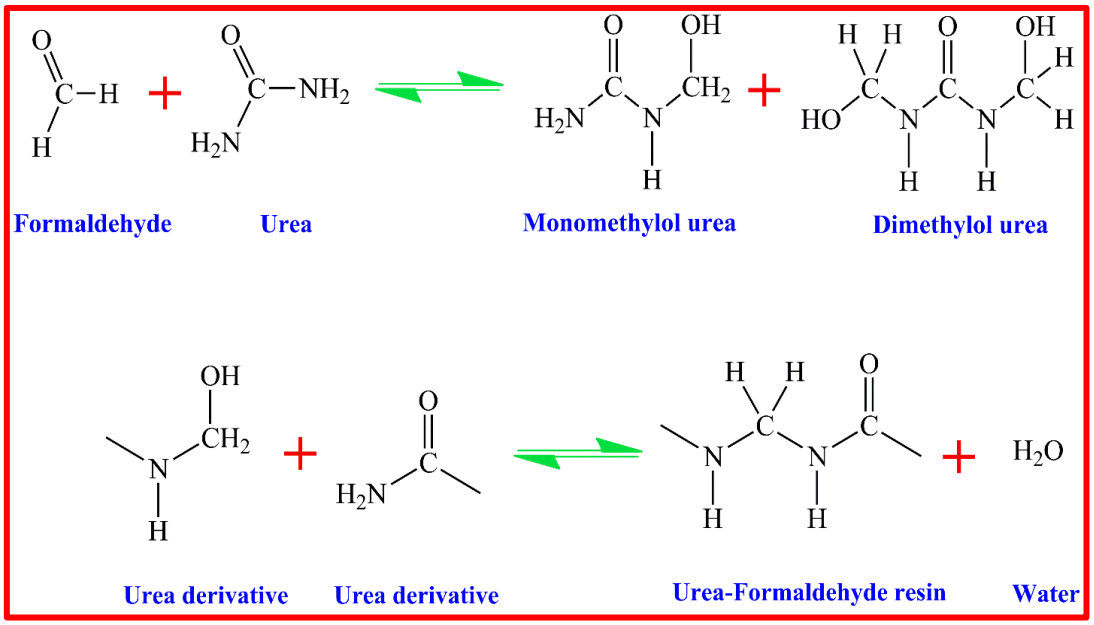

Fig. 2.2 Schematic diagram of the polymerization process of U-F.

After annealing, dark brown-coloured NZF nanopowder was received. The chemical reaction of NZF formation in this process is as follows:

$$0.2Ni(NO_3)_2.6H_2O + 0.8Zn(NO_3)_2.6H_2O + 2Fe(NO_3)_3.9H_2O + 3C_6H_8O_7 \rightarrow Ni_{0.2}Zn_{0.8}Fe_2O_4 + CO_2 + H_2O + N_2 \quad (2.1)$$

2.2.2. U-F Microcapsule synthesis

The polymeric U-F microcapsules were prepared using the reverse micellar procedure as shown stepwise in Fig. 2.3. In the beginning, 2 gm resorcinol, 1 gm NH_4Cl and 10 gm Urea were mixed in 100 ml DI. When everything was dissolved completely in water, aqueous solution of PVA (5 wt.%) was included in it and stirred. Next, the solution was made acidic by reducing its pH to 2. The stirring speed then increased from 500 rpm to 900 rpm, and 50 ml flaxseed oil was dripped very slowly in the solution for maintaining the size and shape of the microcapsules. ~ 4 gm NZF was added to the mixture. Finally, 37 wt.% formaldehyde solution was incorporated in the solution, while the temperature raising to 65 °C. Shortly, after 3 hrs, polymeric microcapsules enclosing NZF nanomaterial and flaxseed oil were formed. The microcapsules were then collected by filtration, washed, and dehydrated at room temperature overnight.

The chemical reactions of urea-formaldehyde polymerization are presented in Fig. 2.2. The whole polymerization occurs in a two-stage procedure: alkaline methylolation and acid condensation. In the 1st step, each molecule of urea connects with the formaldehyde molecules to form mono-, di- and tri-methylolurea prepolymers. In the 2nd stage, the prepolymers get accumulated on the surface of the oil droplets, and polymerization occurs at high temperatures. Finally, polymeric microcapsules encircling the core material (NZF+oil) are formed.

2.2.3. Self-healable bilayered film fabrication

Spin coating technique was used for depositing the bi-layered self-healable photo-detecting film. Temperature was controlled skillfully to maintain the microcapsules unbroken in the prepared film. ~ 8 gm microcapsules were mixed in 10 ml DI, and the mixture was smeared evenly on a clean substrate (glass) inside the spin coater spinning at 500 rpm, and dried at 55 °C for 10 min. Next, a dispersion of 2 gm NZF in acetic acid (10 ml) was layered above this film by spin coating at 1100 rpm for

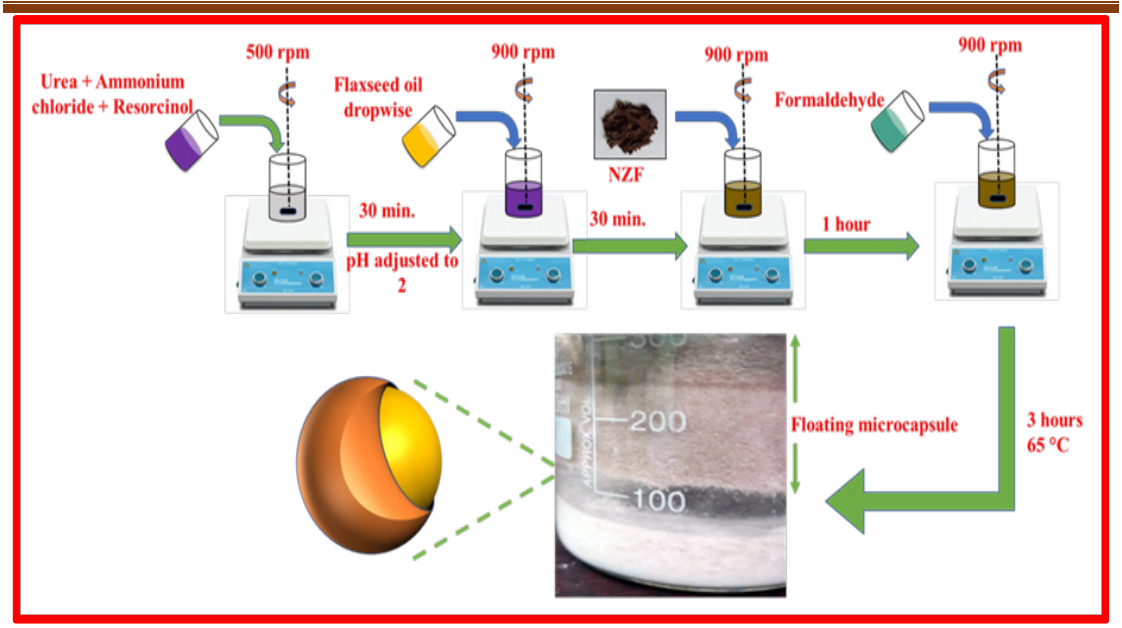

Fig. 2.3 Schematic representation of steps involved in the synthesis process.

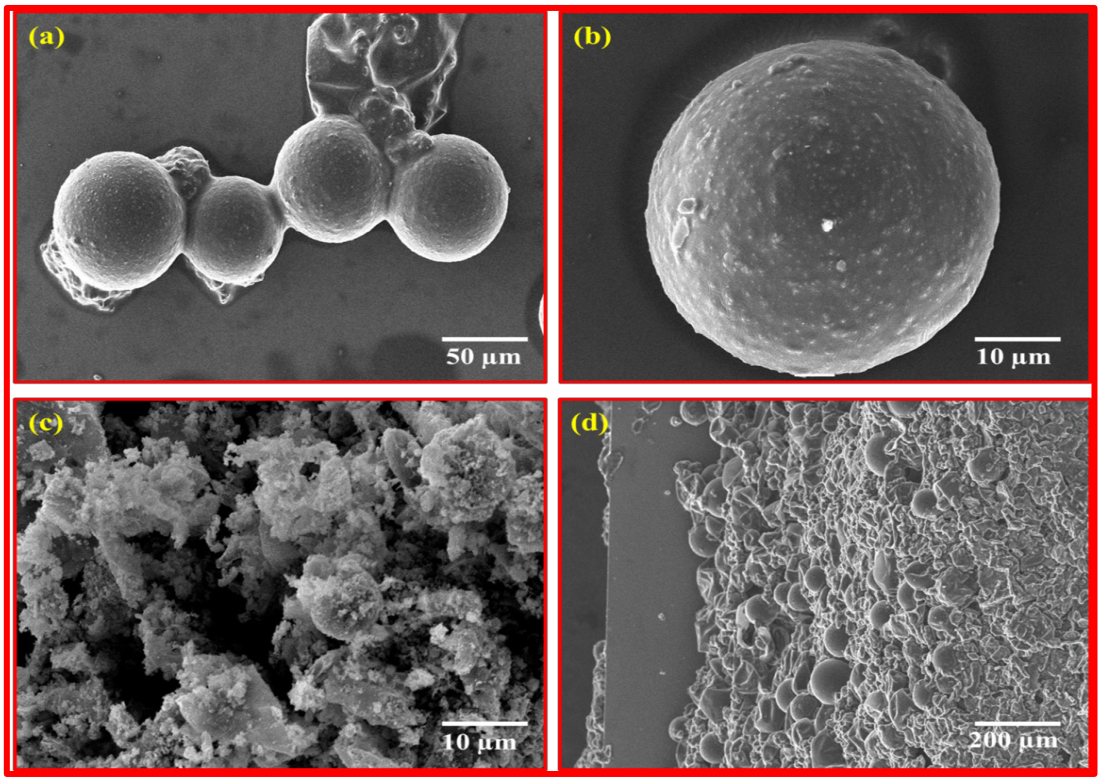

Fig. 2.4 SEM images of (a) group of microspheres, (b) single microcapsule, (c) porous NZF film and (d) dual-layered film.

60 sec. The final bi-layered film was ultimately desiccated by giving a temperature of ~55 °C for a period of 10 min.

2.3. Results and discussion

2.3.1. SEM and EDS analysis

SEM micrographs were taken for the morphological analysis of the microcapsules and NZF nanomaterials, along with the prepared bi-layered sensing film.

Fig. 2.4(a) shows the clustered microcapsules, being perfect spherical in shape. Fig. 2.4(b) shows a single microcapsule with a smooth surface. The SEM results verify the reliability of synthesis process in the formation of even, identical, perfect spheres of microcapsules.

Fig. 2.4(c) displays the porous surface of NZF nanomaterial, while, Fig. 2.4(d) demonstrates the SEM micrograph of the bi-layered film, that was analyzed when the sample stage was tilted at 53° from vertical.

The EDS analysis in Fig. 2.5 approves the presence of all constituent elements such as Iron (Fe): 47.73 wt.%, Oxygen (O): 20.36 wt.%, Zinc (Zn): 28.20 wt.% and Nickel (Ni): 3.71 wt.%.

2.3.2. HR-TEM analysis

The nesting of NZF in the interior of the polymeric microcapsules was affirmed by HR-TEM accompanied by SAED configuration (Fig. 2.6(a-d)). The outer periphery of the microcapsules containing the dark core material can be visualized easily. The SAED pattern revealed the lattice fringes of NZF regarding the planes (220) and (311) as shown in Fig. 2.6(b). A gloomy ring can be observed around NZF planes which represents the polymeric shell. In the TEM image of Fig. 2.6(c), the average NZF dimension can be seen as ~20 nm. Fig. 2.6(d) shows the crystalline nature of NZF. The interplanar spacing of the certain set of planes was ~0.165 nm, which belongs to (511) set of planes, as revealed from the XRD pattern of NZF.

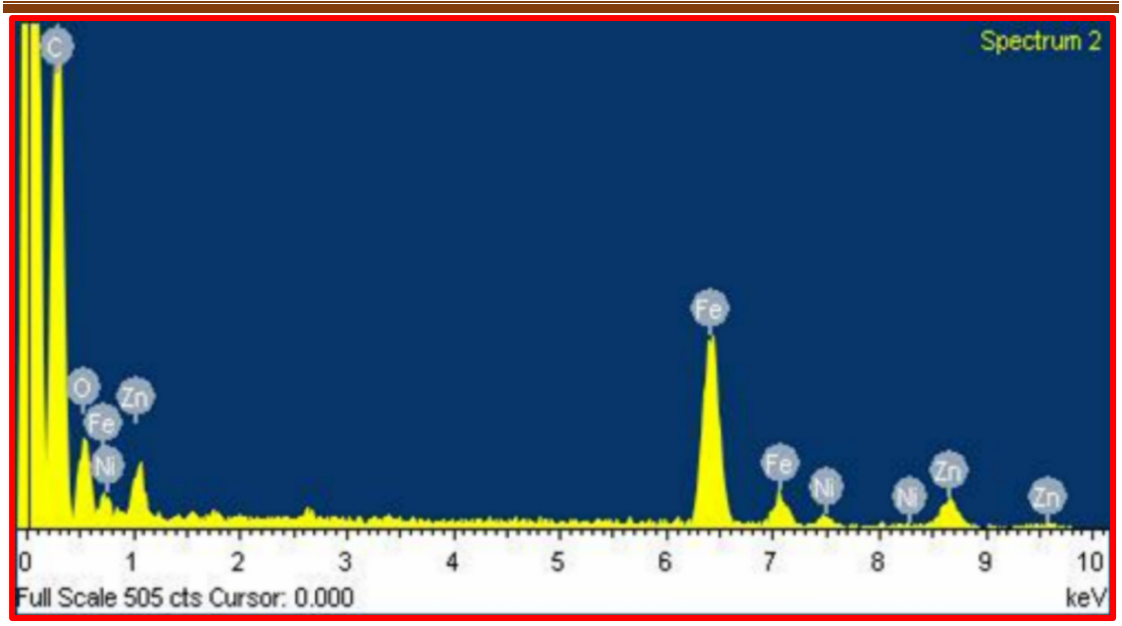

Fig. 2.5 EDS spectra of NZF nanopowder.

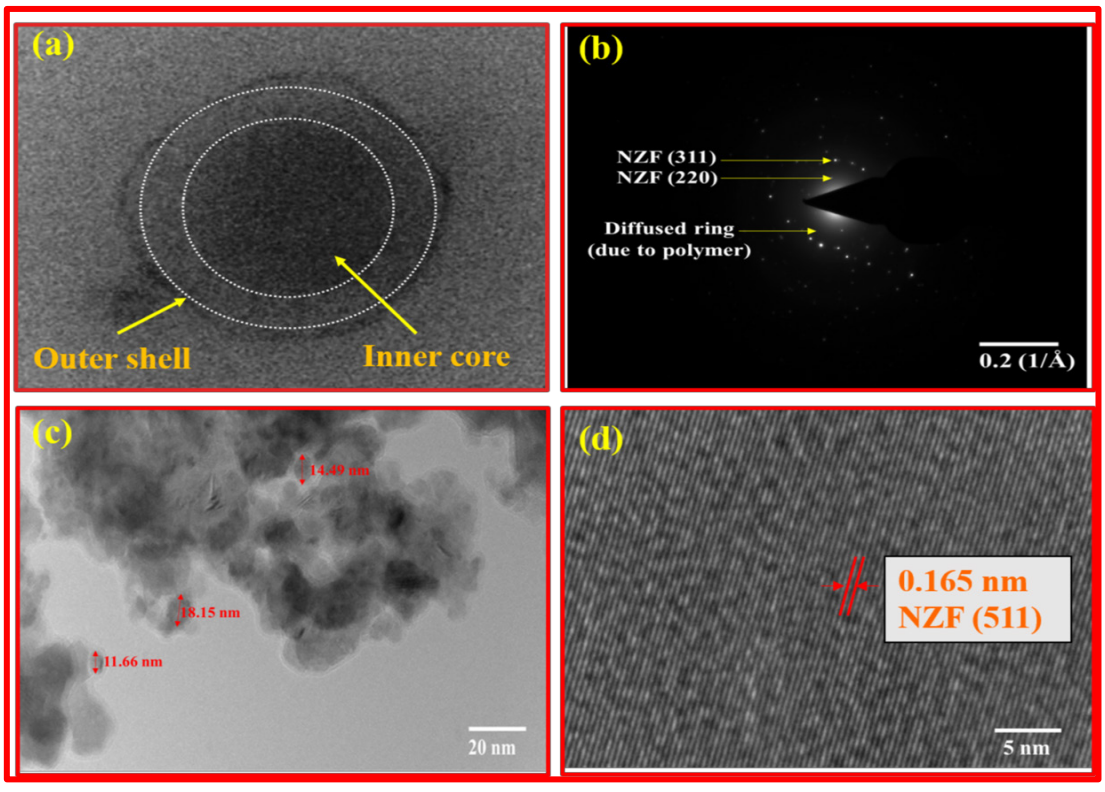

Fig. 2.6 (a) TEM image of single microsphere showing outer and inner boundary, (b) SAED pattern of NZF-flaxseed oil encapsulated U-F microcapsules, (c) TEM

image of NZF inside microsphere and (d) HRTEM image of crystalline NZF nanomaterial.

2.3.3. XRD analysis

The XRD representations of NZF nanopowder prior to, and after heat treatment is given in Fig. 2.7(a) and (b), arranged in the same scaling to get better visualization. The heat-treated nanomaterial owns all prominent characteristic peaks of NZF, as indexed in the image (JCPDS 08-0234). The diffraction from the planes (440), (511), (422), (400), (222), (311) and (220) occurred at 61.98°, 56.42°, 52.96°, 42.58°, 34.96° and 29.62° positions respectively.

In the as-synthesized sample, almost all characteristic NZF peaks have appeared, but their intensities are very low owing to low crystallinity. Whereas, sharp and strong peaks have occurred in the annealed sample, proving significant enhancement in both crystallinity and crystallite size due to heating at 600 °C. The molecular concentration increases on the surface of the crystal when a high temperature is applied. As a result, crystal growth is encouraged at high temperatures. Moreover, the mobility of atoms also increases at high temperatures, which provides excess energy to the crystal grains for further growth.

Using Scherer relation, the average crystallite size along (311) direction was calculated in case of both the samples:

$$D = 0.9\lambda/\beta\cos\theta \qquad (2.2)$$

Here, D, λ, θ and β are crystallite size, wavelength of the striking beam, Bragg's angle and FWHM. The measured size of the crystallite along (311), interplanar spacing of (311) planes and lattice constant of NZF before and after annealing are shown in Table 2.1, which illustrates that all the parameters have improved greatly with temperature. This means heat treatment is very important for controlling crystallization and crystallite sizes.

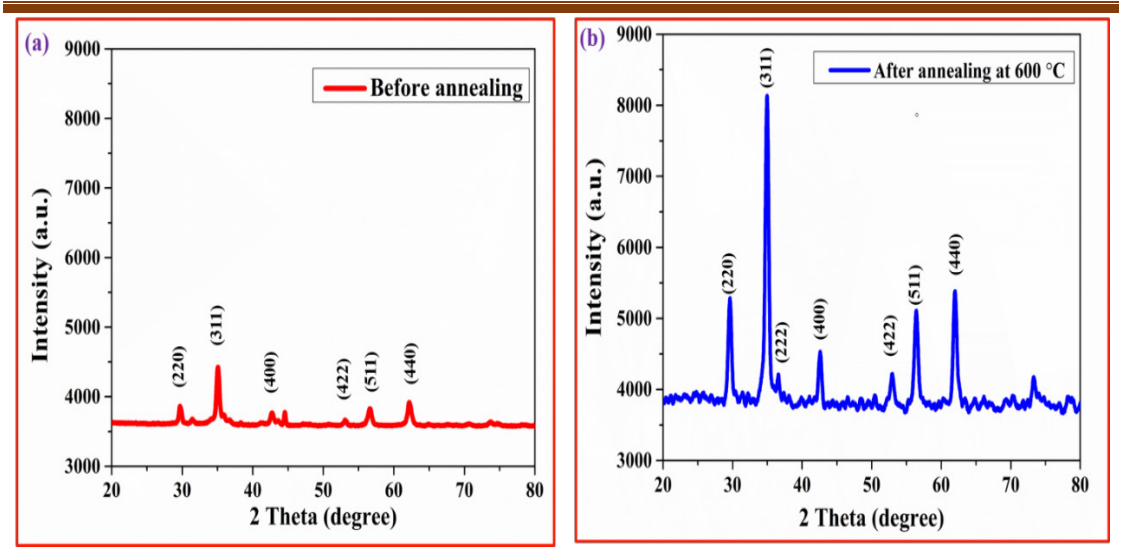

Fig. 2.7 XRD pattern of polycrystalline $Ni_{0.2}Zn_{0.8}Fe_2O_4$ nanopowder (a) before annealing and (b) after annealing (JCPDS No. 08-0234).

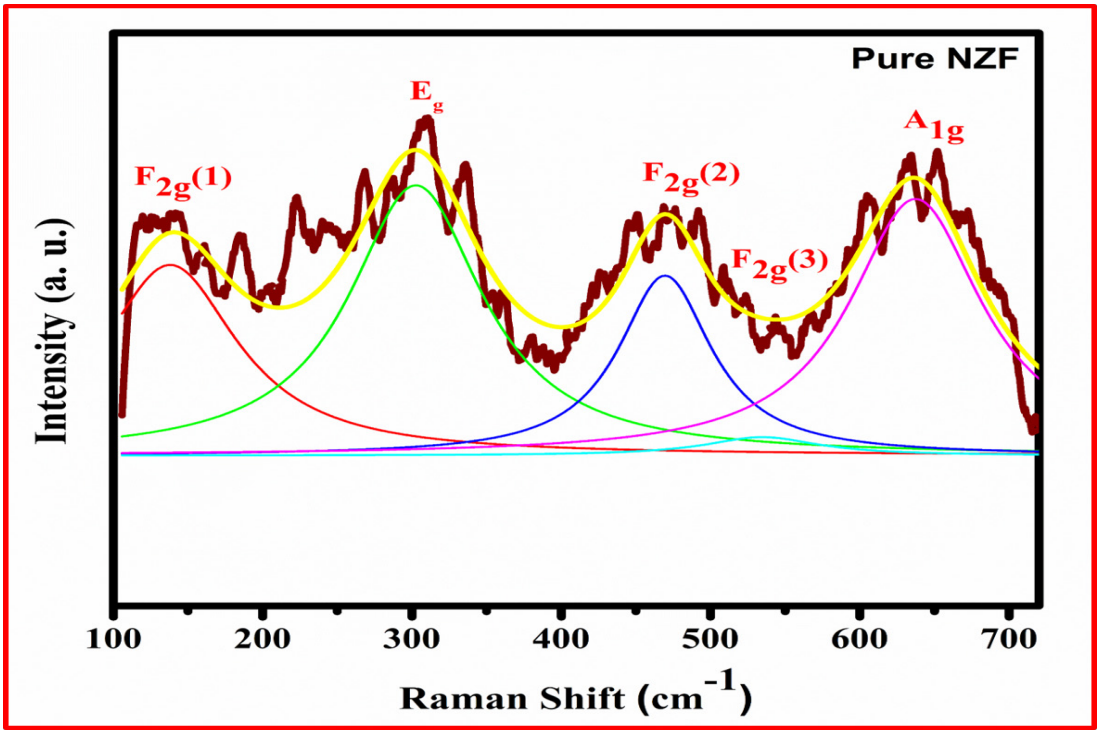

Fig. 2.8 Raman spectra of pure NZF nanopowder (annealed).

Table 2.1. Effect of annealing on crystal parameters.

Sample	Crystallite size, D (nm)	Interplanar spacing, d (Å)	Lattice constant, a (Å)
NZF before annealing	14.57	2.5635	8.1035
NZF after annealing	17.73	2.5690	8.1239

2.3.4. Raman analysis

In general, Zn^{2+} cations conquer the tetrahedral sites of the NZF lattice, and introduce structural disorder in the lattice, due to having larger diameter than Ni^{2+} cations. From the group theory prediction, the Raman active modes present in cubical spinel NZF (Fd-3m symmetry) are, $3F_{2g}$, A_{1g} and E_g [33]. The symmetric stretching vibrations of oxygen in Zn–O, Fe–O, along with Ni–O bonds residing in the tetrahedral positions give rise to A_{1g} modes, appearing at ~637 cm^{-1}. When vibrations occur among the ions residing in octahedral positions, they create two Raman modes: F_{2g} (2) and F_{2g} (3) at ~ 470 cm^{-1} and ~35 cm^{-1} correspondingly. The symmetric bending of oxygen anions in Fe–O bonds represents E_g mode at 303 cm^{-1}.

2.3.5. FTIR analysis

The IR exploration of annealed NZF, microcapsules containing only flaxseed oil, together with the microcapsules containing both flaxseed oil and NZF was done, and comparative data are presented in Fig. 2.9 for analysing the presence of characteristic peaks corresponding to the constituent phases in the nanohybrid.

The spectrum of NZF (black line) contains the fingerprint vibrations of spinel ferrites at 542.9 cm^{-1} due to stretching vibrations in M–O bonds residing in the tetrahedral positions, and under 400 cm^{-1} (not able to be detected precisely due to the instrumental limitations) due to stretching vibrations in M–O bonds residing in the octahedral positions [33].

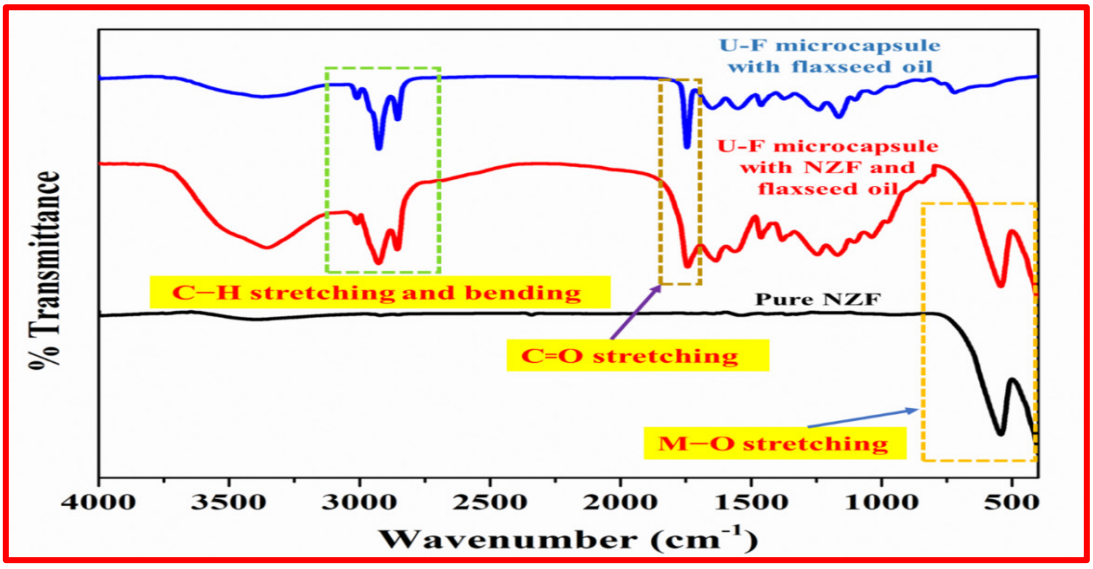

Fig. 2.9 FTIR spectra of U-F microcapsule with flaxseed oil, pure NZF and U-F microcapsule with NZF-flaxseed oil.

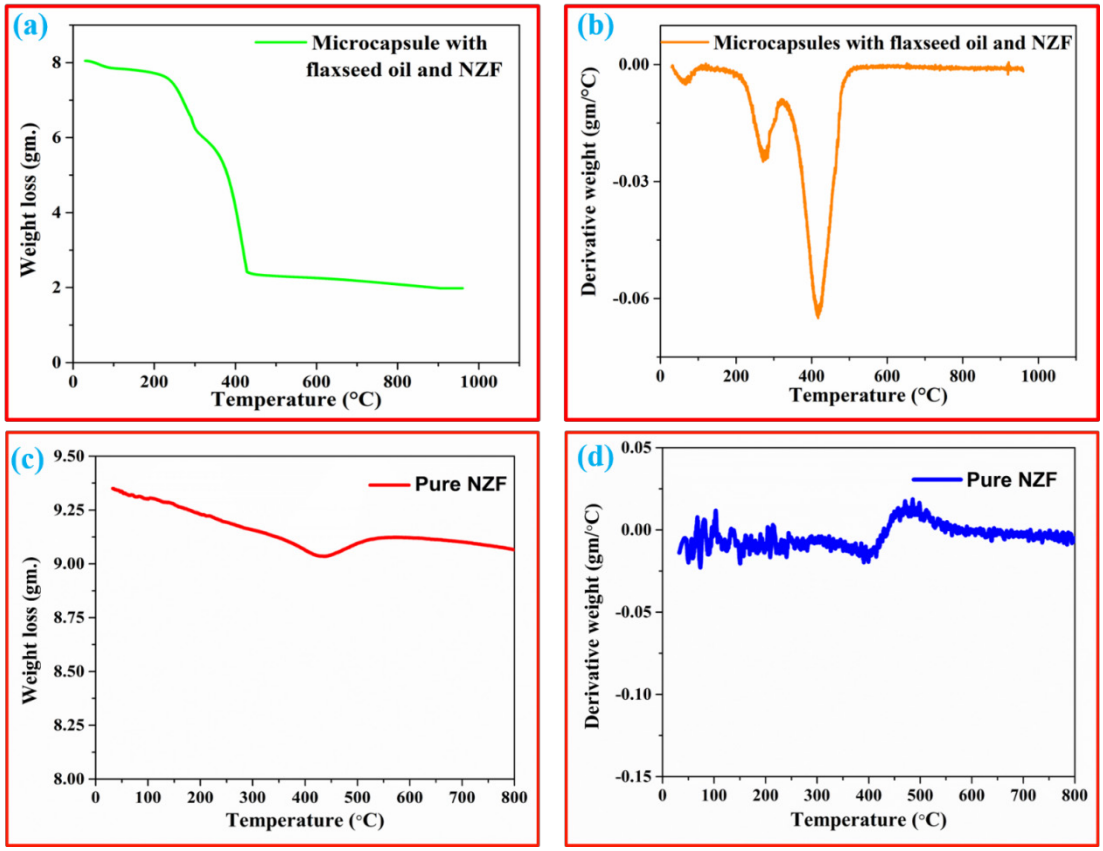

Fig. 2.10 Thermogravimetric analysis (a) Weight loss vs. Temperature of U-F microspheres with NZF-flaxseed oil **(b)** DTG curve of U-F microspheres with NZF-flaxseed oil (c) Weight loss vs. Temperature of pure NZF (d) DTG curve of pure NZF.

The spectrum of microcapsules containing flaxseed oil (blue line) contains representative vibrations of the core counterpart (flaxseed oil) at 1743 cm^{-1} and 1168 cm^{-1} because of vibrations generated due to stretching motions in the bonds C−O and C=O respectively. Another prominent vibration has also been perceived at 3354 cm^{-1} arising from the stretching at secondary N−H bonds. The bands present at 3016 cm^{-1}, 2929 cm^{-1}, 2850 cm^{-1} exist as the consequence of stretching at sp^3 C−H, whereas, the band at 1461 cm^{-1} is owing to bending at sp^3 C−H [29, 30].

The spectrum of microcapsules containing NZF and flaxseed oil (red line) contains all the representative bands of the individual phases, which confirms the presence of all the phases in the hybrid sample.

2.3.6. TGA analysis

To analyze the thermal stability of the hybrid sample and to assess the quantity of each phase present in the hybrid, TGA/DTA investigation was performed by raising the temperature upto 1000 °C (Fig. 2.10(a),(b)). The experiment started with ~8 gm of the sample. Later, at a temperature ~310 °C, the U-F microcapsules were decomposed, leaving NZF and flaxseed oil in the specimen. Beyond 310 °C, out of the initial amount, ~6.11 gm of the sample remained, and ~1.93 gm of U-F polymer material got decomposed. Hence, ~24% U-F polymer was existing in the nanohybrid. A major decomposition took place ~480 °C, proving the decomposition of the oil phase, after which ~2.42 gm sample remained, which is basically NZF. Therefore, in the hybrid, ~46% of material was flaxseed oil, while ~30% material was NZF. Beyond 480 °C, any loss in weight was not witnessed.

The TGA/DTA analysis of just-prepared NZF (without annealed) is presented in Fig. 2.10(c),(d). Three different decompositions can be seen in the curve. At 1st, among 50 °C – 150 °C, the adsorbed compounds (CO_2, H_2O etc.) got released from

NZF. Next, from 150 °C- 400 °C, oxidation of organic complexes and breakage of inorganic compounds happened. Then, from 400 °C – 600 °C the development of the metal oxide took place. Beyond that, any loss in weight was not witnessed, which means that annealing the sample at a temperature equal to or higher than 600 °C can eliminate all impurities.

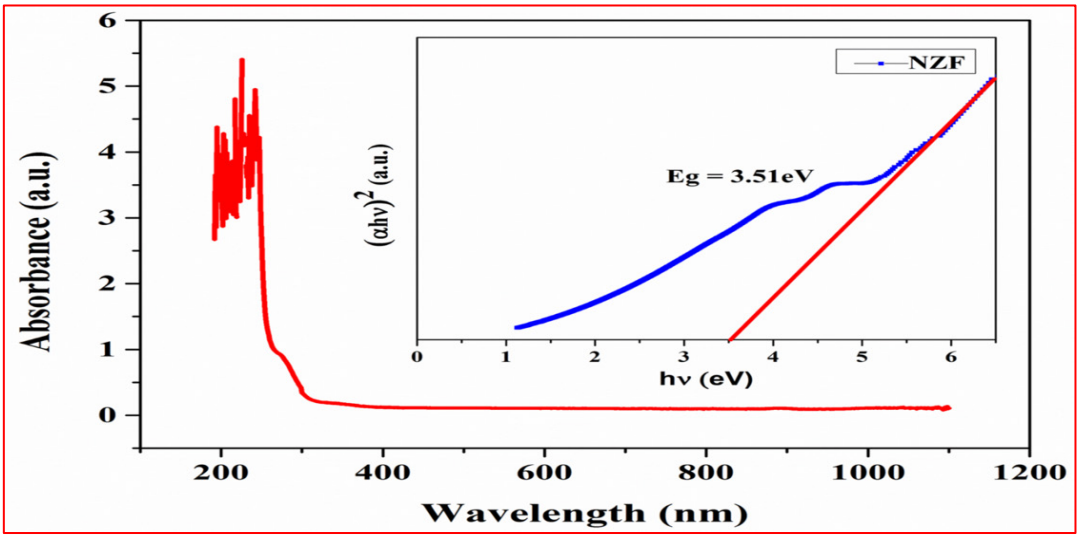

Fig. 2.11 Absorption spectra of pure NZF film with Tauc plot in the inset for band gap observation.

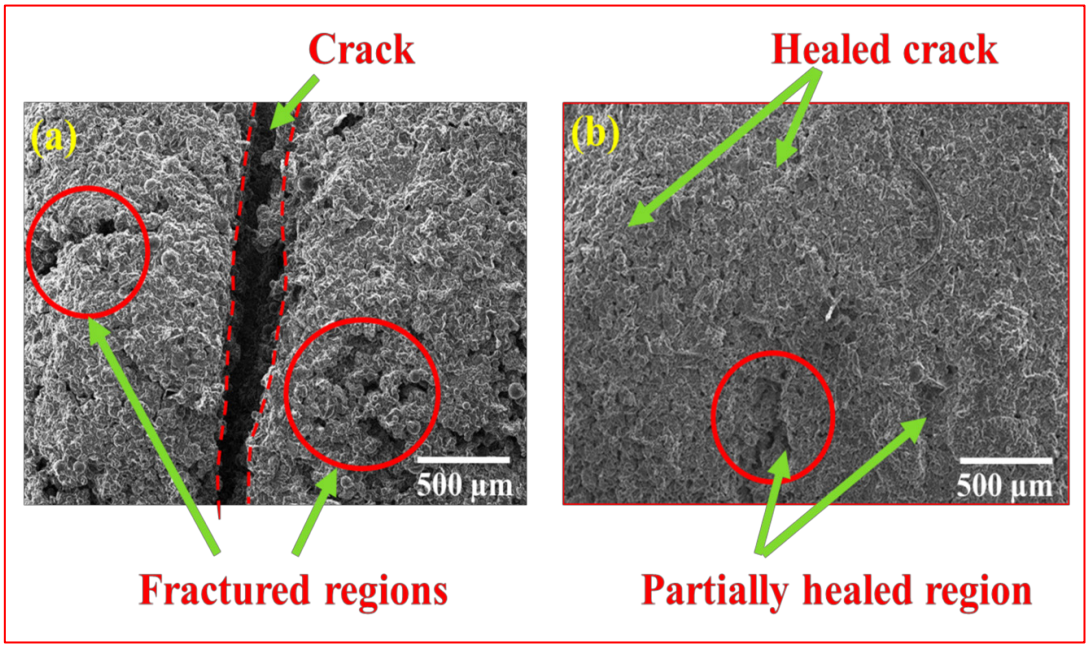

Fig. 2.12 SEM analysis of (a) cracked, and (b) healed sample.

2.3.7. UV-vis spectroscopy

NZF shows maximum optical absorption at ~307 nm, when irradiated with optical light (Fig. 2.11). The band gap (optical) was measured from the Tauc plot presented in the inset, using the relation

$$\alpha h\nu = A(h\nu - E_g)^n \qquad (2.3)$$

Here, A, and ν are the constant, and the optical transitional frequency respectively. n represents the nature of the transition, where n is considered 1/2 when band gap is direct, and 1/3 when it is indirect. In NZF, n is taken 1/2 as its band gap is direct in nature. The band gap acknowledged from the Tauc plot of NZF was ~3.51 eV.

2.4 Self-healing analysis

2.4.1. Self-healing capability of the sensing film

The chief purpose of this report is the fabrication of a sensing film which is able to recoup its actual structure afterwards any deformation. The recovery of sensing properties of the film also depends on the amount of healing. If any discontinuity is present amid the anode and cathode in the device, we won't get any response as the drift of charge carriers is obstructed by that damaged area. The movement of the charge carriers can be regained only when the damage will be recovered. For that purpose, a bi-layered film was assembled with the topmost layer acting as the detector, and lower layer acting as healer. The microcapsules containing NZF and flaxseed oil make the healing layer, where flaxseed oil plays the character of a mediator to transport NZF towards the cracked region owing to its mobility, as granular NZF cannot transfer by itself. After creating an imitation fracture, the bi-layered film was warmed at ~100 °C, where, the microcapsules broke, and the oil with NZF came out and filled the crack. Fig. 2.12 (a) shows the SEM micrograph of the cracked region of the film, where, some additional fractures can be seen in the film as some stress developed in the sample while creating the crack. After generating the crack, the film was kept at a temperature of ~100 °C for 60 min and then kept at ambient temperature overnight to get rid of all the extra oil from the material.

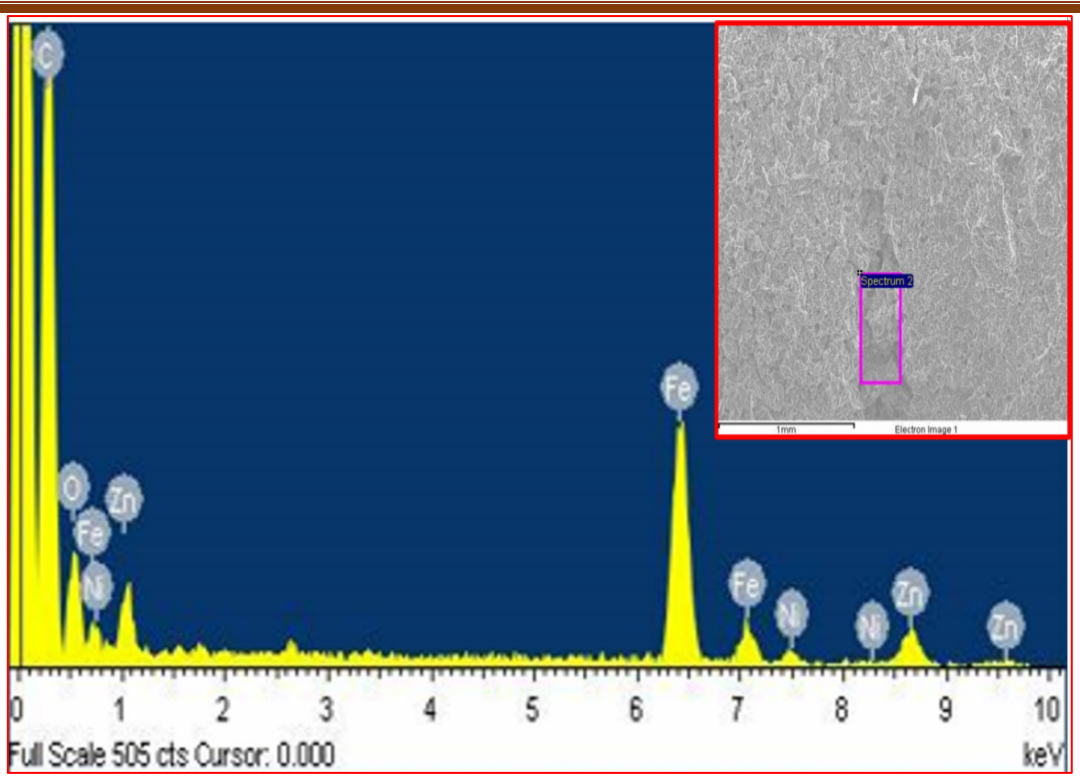

Fig. 2.13 EDS response from the healed region of the film.

Figure 2.12 (b) shows the SEM image of the healed region of the film where partial healing can be observed in some places around the edge of the film, which might be due to leakage of NZF with the oil through the edges. EDS analysis was performed in the healed region to prove the presence of NZF in the healed area (Fig. 2.13). It confirmed that NZF was effectively mediated in the deformed area.

2.4.2. Photodetection mechanism

When a sensing film is kept in the open atmosphere, the molecules of oxygen start chemically adsorbing on the sensing element by the reaction with the surface electrons of the material as,

$$O_2\,(ads) + e^- \leftrightarrow O_2^-(ads) \qquad (2.4)$$

$$O_2\,(ads) + 2e^- \leftrightarrow 2O^-(ads) \qquad (2.5)$$

$$O^-(ads) + e^- \leftrightarrow O_2^-(ads) \qquad (2.6)$$

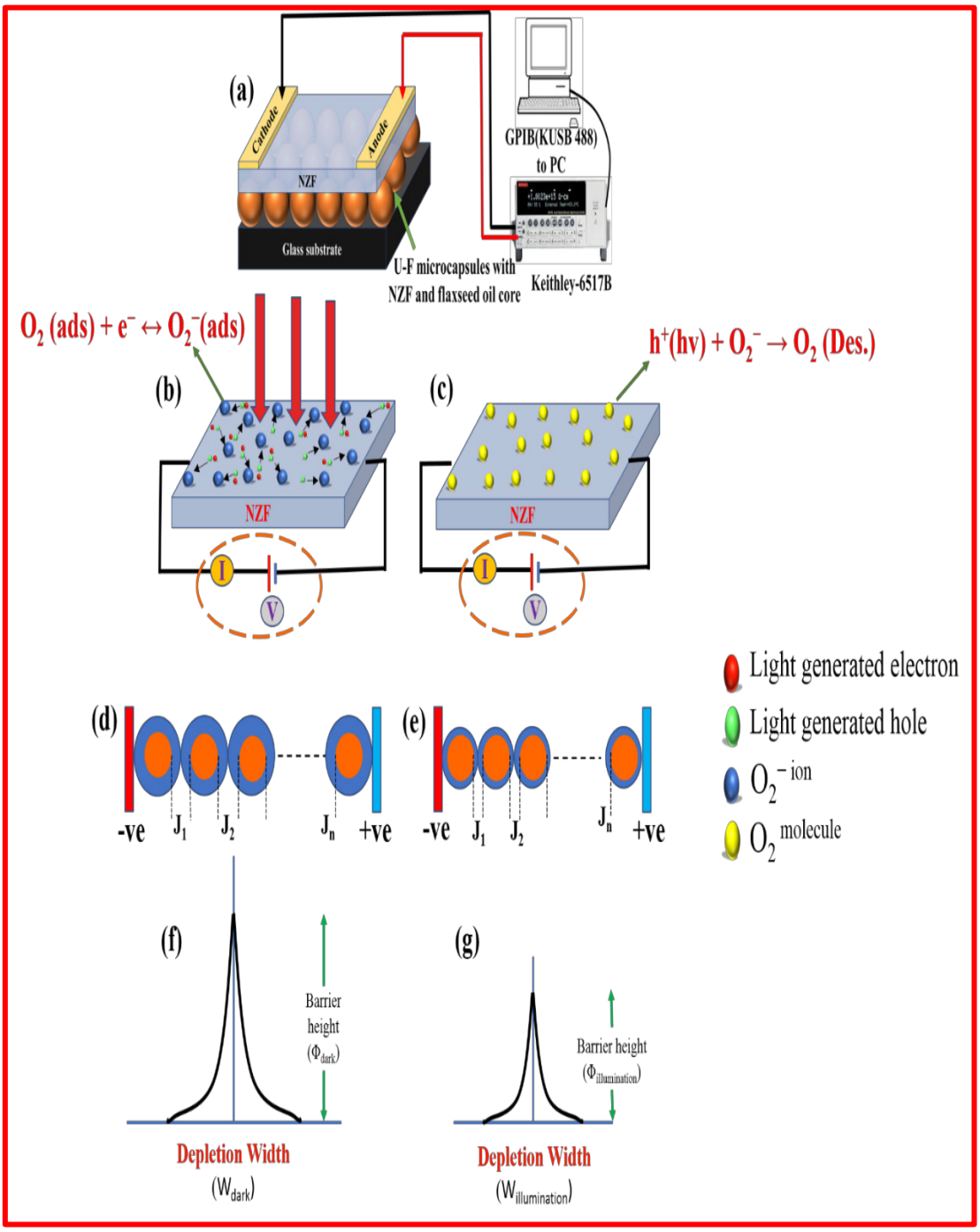

Fig. 2.14 (a) Schematic diagram of the device with measuring unit (b) formation of O_2^- ion due to environmental exposure of the device and generation of electron-hole pair due to light (c) Conversion of O_2^- ion into O_2 molecule via reaction with holes in the presence of illumination (d) Formation of multiple junctions between metal oxide

grains due to atmospheric exposure (e) Diminution in depletion width after illumination (f) Potential barrier vs. depletion width curve under dark condition (g) decrease in barrier height along with depletion width under illumination.

When the film is radiated with light, multiple electron-hole pairs are created in the material, from which, the holes interact with the previously adsorbed oxygen ions and free oxygen molecules in air.

$$h^{+}(h\upsilon) + O_2^{-} \rightarrow O_2\,(Des) \qquad (2.7)$$

The residual electrons then rise the carrier concentration of the material, creating a decrement in the width of the depleted region along with the electrical resistance of the material. As time passes, further charge carriers get generated, and a significant reduction of the resistance is achieved. This phenomenon practically can be observed in Fig. 2.15. When the light is turned off, the material regains its actual resistance.

2.4.3. Photodetection performance before and after healing

The changes in the resistance of sensing film in the attendance and absence of illumination (~100 mW/cm^2) are shown in Fig. 2.15. After the crack generation, no response was seen in the film, as the charge carriers were not able to move between the electrodes. However, after healing, the response reoccurred (Fig. 2.15(b)). Both the responses of the uncracked film and healed film were almost similar, indicating towards good healing. The photo-response of the material was calculated from the formula:

$$\textbf{Response}\ (\%) = \frac{R_d - R_\ell}{R_d} x100 = \frac{\Delta R}{R_d} x100 \qquad (2.8)$$

Here, R_ℓ and R_d are the resistances in light and dark correspondingly. The variation in the resistance of sensing element is the outcome of the generation of numerous charge carriers in presence of light and it can be described by the relation,

$$\Delta R = \frac{\ell}{q\mu dt\Delta n} \qquad (2.9)$$

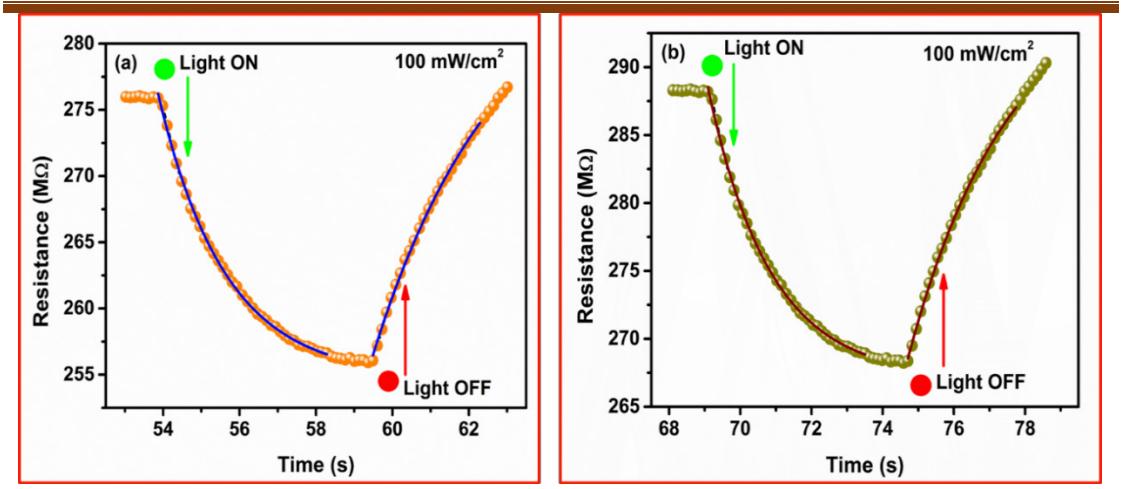

Fig. 2.15 Change in electrical resistance (a) before healing, and (b) after healing at 100 mW/cm^2 light intensity.

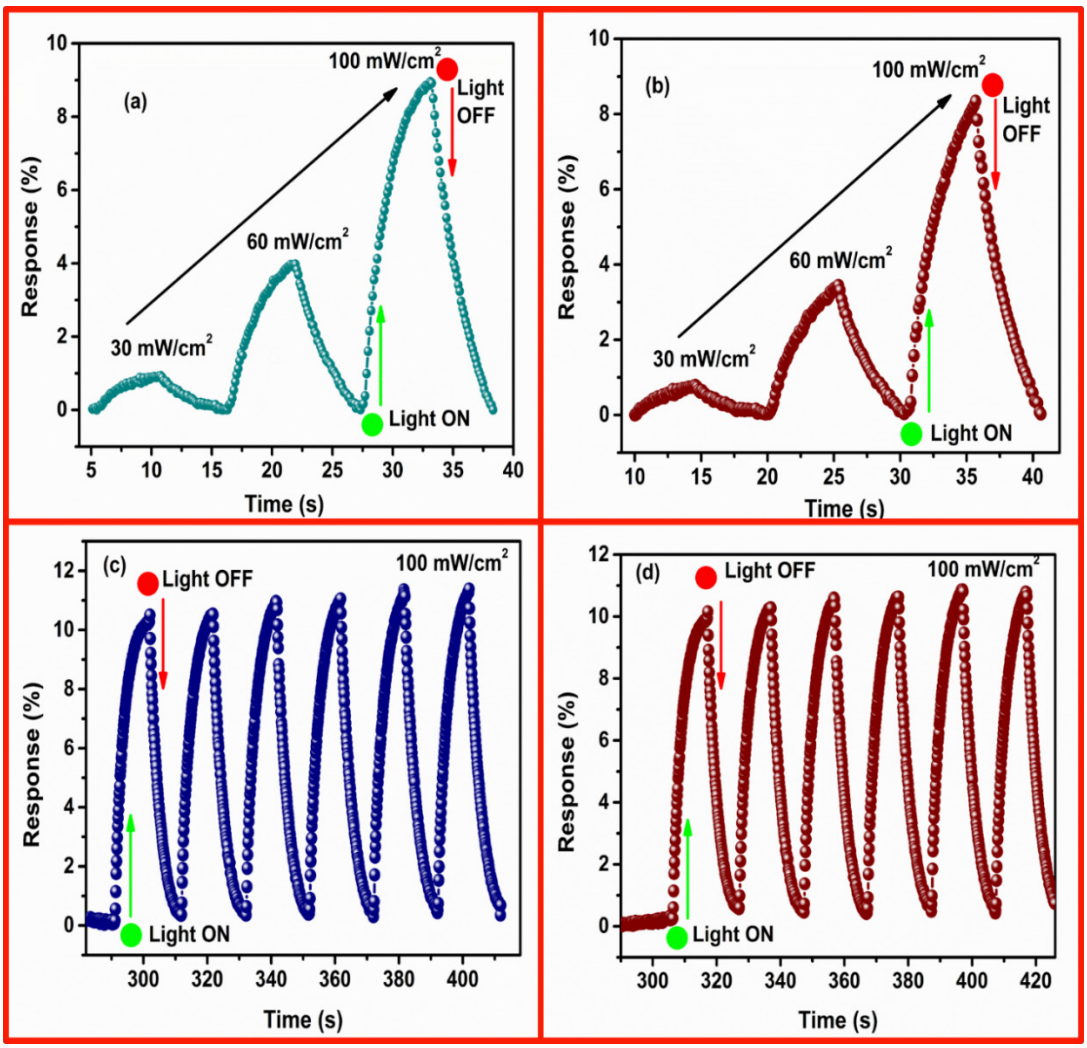

Fig. 2.16 Photoconductive response of NZF (a) before healing (b) after healing at 30, 60 and 100 mW/cm^2 light intensities. The behaviour of Photo response at fixed 100 mW/cm^2 light illumination (c) before self-healing and (d) after self-healing for continuous 6 repeated cycles of illumination and dark.

Where q, μ, d, ℓ, Δn and t are the electronic charges, mobility, width, lengths, change in the carrier concentration under radiation, and thickness of the sensing material respectively.

The photo response of the uncracked film and healed film were measured in case of illuminations of 30, 60 and 100 mW/cm^2 and plotted as shown in Fig. 2.16 (a) and (b). The response/recovery times in uncracked and healed films were calculated to be ~1.74/3.28 sec and 1.75/2.84 sec respectively. Hence, the deviation in the case of response time was ~0.57%, while the same in recovery time was ~13%.

For noticing the reproducibility of the material, the uncracked and healed film was exposed repeatedly to illumination (100 mW/cm^2), as well as dark multiple times, as revealed in Fig. 2.16(c),(d). Both the films show almost similar result, when same experiment was repeated continuously.

Another essential parameter for the evaluation of the sensing performance is responsivity. It can be demonstrated as the current density per illumination power, i.e.,

$$R_\lambda = \frac{J_p}{P_d} = \frac{\Delta I}{A P_d} \qquad (2.10)$$

Where R_λ, J_p, P_d, ΔI and A are the responsivity, current density, illumination power, photo-current, and illuminated film area.

~98.5% response was recovered via healing, revealing successful regain of sensing properties. The electrical resistance of the material was slightly raised after healing (from 276 MΩ to 286 MΩ), possibly due to either partial healing at some places as discussed earlier, or, the existence of some oil in the voids of the film. These outcomes approve that a photodetector is successfully prepared that can reestablish its sensing properties after any mechanical damage.

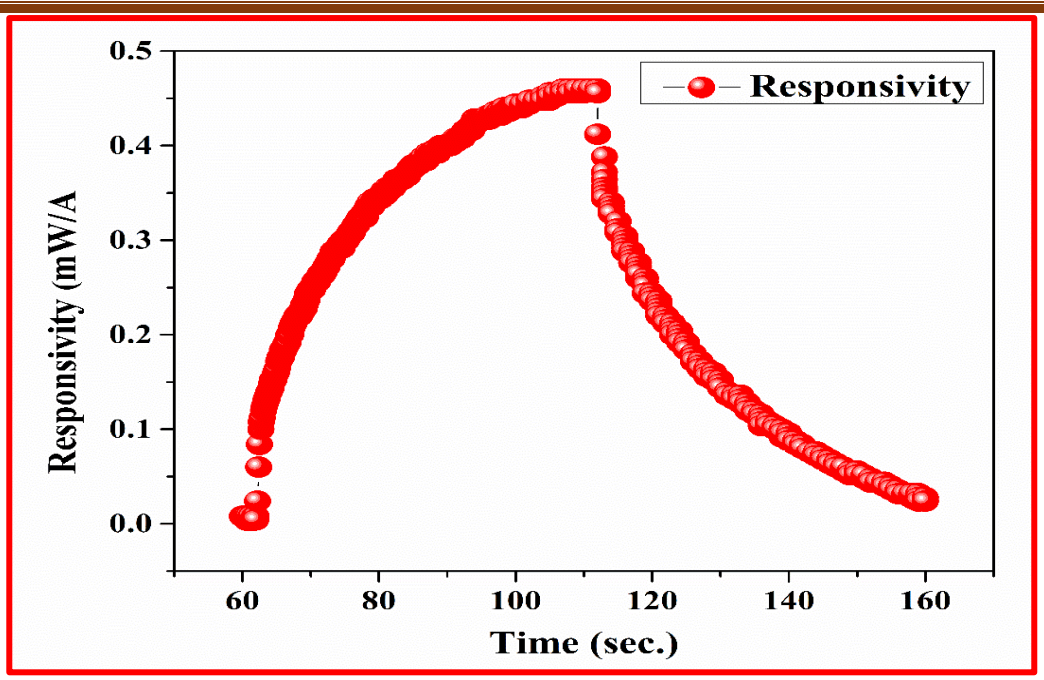

Fig. 2.17 Responsivity curve under the illumination of 100 mW/cm^2.

2.5. Conclusions

The NZF nanomaterial was synthesized via citrate acid aided sol-gel scheme and was used for the light detection measurements. The microcapsules made with U-F polymer, encompassing NZF and flaxseed oil were prepared using reverse micellar method and used to achieve self-healing. The preparation methods are quite easy, effortless and inexpensive. The polycrystallinity and pureness of the NZF were established by XRD study. The wrapping of the nano ferrite by the U-F polymer was proved via SAED, TEM, and FTIR analysis. The effective restoration of the element was authenticated using SEM and EDS investigations. By regaining the actual configuration, the sensing element was competent to reinstate the sensing properties. The response/recovery times taken by the undamaged film were 1.74/3.28 sec, whereas the same for the film after healing were 1.75/2.84 sec correspondingly. The detection capability of the specimen post healing was re-creatable towards ~98.5%. Thus, we have effectively elaborated a procedure for preparation and fabrication of a bi-layered photo-detecting device, which can redeem its actual operations when any damage occurs in its physical structure.

References

[1] M. A. Destek, A. Aslan, Renewable and non-renewable energy consumption and economic growth in emerging economies: Evidence from bootstrap panel causality, Renewable Energy. 111 (2017) 757-763.

[2] Y. Saito, T. Nojima, Y. Iwasa, Highly-crystalline 2D superconductors. Nature Reviews Materials. 2 (2016) 16094.

[3] A. Charnukha, D. Propper, N. D. Zhigadlo, M. Naito, M. Schmidt, Z. Wang, J. Deisenhofer, A. Loidl, B. Keimer, A. V. Boris, D. N. Basov, Intrinsic charge dynamics in high-Tc AFeAs(O,F) superconductors, Phys. Rev. Lett. 120 (2018) 087001.

[4] K. Han, Z. Liu, J. Shen, Y. Lin, F. Dai, H. Ye, A Free-Standing and Ultralong-Life Lithium-Selenium Battery Cathode Enabled by 3D mesoporous Carbon/Graphene Hierarchical Architecture, Adv. Funct. Mater. 25 (2015) 455–463.

[5] J. Song, M. L. Gordin, T. Xu, S. Chen, Z. Yu, H. Sohn, J. Lu, Y. Ren, Y. Duan, D. Wang, Strong Lithium Polysulfide Chemisorption on Electroactive Sites of Nitrogen-Doped Carbon Composites for High-Performance Lithium–Sulfur Battery Cathodes, Angew. Chem. Int. Ed. 54 (2015) 4325 –4329.

[6] C. Sun, J. Liu, Y. Gong, D. P. Wilkinson, J. Zhang, Recent advances in all-solid-state rechargeable lithium batteries, Nano Energy, 33 (2017) 363–386.

[7] I. Rawal, O. S. Panwar, R. K. Tripathi, A. K.Srivastava, M. Kumar, S. Chockalingam, Structural and nanomechanical properties of nanocrystalline carbon thin films for photodetection, Journal of Vacuum Science & Technology A. 33 (2015) 031501.

[8] R. K. Tripathi, O.S. Panwar, I. Rawal, B.P. Singh, B.C. Yadav, Study on nanocrystalline silicon thin films grown by the filtered cathodic vacuum arc technique using boron-doped solid silicon for fast photo detectors, Journal of the Taiwan Institute of Chemical Engineers. 000 (2018) 1–7.

[9] I. Rawal, Tripathi, R. K. Tripathi, O.S. Panwar, Easy Synthesis of Organic-Inorganic Hybrid Nanomaterials: Study of DC Conduction Mechanism for Light Dependent Resistors, RSC Adv. 6 (2016) 31540-31550.

[10] I. Rawal, N. Dwivedi, R. K. Tripathi, O.S. Panwar, H. K. Malik, Organic-inorganic hybrid nanomaterials for advanced light dependent resistors, Materials Chemistry and Physics. 202 (2017) 169-176.

[11] R. Kripal, A. K. Gupta, R. K. Srivastava, S. K. Mishra, Photoconductivity and photoluminescence of ZnO nanoparticles synthesized via co-precipitation method, Spectrochimica Acta Part A. 79 (2011) 1605– 1612.

[12] A. K. Tripathi, M. C. Mathpal, P. Kumar, M. K. Singh, M.A.G. Soler, A. Agarwal, Structural, optical and photoconductivity of Sn and Mn-doped TiO_2 nanoparticles, Journal of Alloys and Compounds. 622 (2015) 37–47.

[13] T. Georgakopoulos, N. Todorova, K. Pomoni, C. Trapalis, On the transient photoconductivity behavior of sol–gel TiO_2/ZnO composite thin films, Journal of Non-Crystalline Solids. 410 (2015) 135–141.

[14] C.P. Baldé, V. Forti, V. Gray, R. Kuehr, P. Stegmann, The Global E-waste Monitor, United Nations, University (UNU), International Telecommunication Union (ITU) & International Solid Waste Association (2017).

[15] B. H. Robinson, E-waste: An assessment of global production and environmental impacts, Science of the Total Environment, (ISWA), Bonn/Geneva/Vienna, 408 (2009) 183-191.

[16] A. Leung, Z. W. Cai, M. H. Wong, Environmental contamination from electronic waste recycling at Guiyu, southeast China, J Mater Cycles Waste Manag. 8 (2006) 21-33.

[17] L. Zhang, Z. Xu, A Review of Current Progress of Recycling Technologies for Metals from Waste Electrical and Electronic Equipment, Journal of Cleaner Production. 127 (2016) 19-36.

[18] I. Labunska, S. Harrad, D. Santillo, P. Johnstona, K. Brigden, Levels and distribution of polybrominated diphenyl ethers in soil, sediment and dust samples collected from various electronic waste recycling sites within Guiyu town, southern China, Environ. Sci.: Processes Impacts. 15 (2013) 503.

[19] Q. Song, J. Li, Environmental effects of heavy metals derived from the e-waste recycling activities in China: A systematic review, Waste Management. 34 (2014) 2587-2594.

[20] World Energy Resources, www.worldenergy.org, (2016).

[21] J. H. Lee, R. Hinchet, S. K. Kim, S. Kim, S.-W. Kim, Shape memory polymer-based self-healing triboelectric nanogenerator, Energy Environ. Sci. 8 (2015) 3605.

[22] W. Xu, L.-B. Huang, J. Hao, Fully self-healing and shape-tailorable triboelectric nanogenerators based on healable polymer and magnetic-assisted electrode, Nano Energy. 40 (2017) 399–407.

[23] K. Parida, V. Kumar, W. Jiangxin, V. Bhavanasi, R. Bendi, P. S. Lee, Highly Transparent, Stretchable, and Self-Healing Ionic- Skin Triboelectric Nanogenerators for Energy Harvesting and Touch Applications, Adv. Mater. 29 (2017) 1702181.

[24] Y. Zhao, J. Wei, H. Li, Y. Yan, W. Zhou, D. Yu, Q. Zhao, A polymer scaffold for self-healing perovskite solar cells, Nature Communications. 7 (2016) 10228.

[25] X. Li, D. Yu, F. Cao, Y. Gu, Y. Wei, Y. Wu, J. Song, H. Zeng, Healing All-Inorganic Perovskite Films via Recyclable Dissolution–Recrystallization for Compact and Smooth Carrier Channels of Optoelectronic Devices with High Stability, Adv. Funct. Mater. 26 (2016) 5903-5912.

[26] F. Lang, N. H. Nickel, J. Bundesmann, S. Seidel, A. Denker, S. Albrecht, V. V. Brus, J. Rappich, B. Rech, G. Landi, H. C. Neitzert, Radiation Hardness and Self-Healing of Perovskite Solar Cells, Adv. Mater. 28 (2016) 8726-8731.

[27] H. Jin, T.-P. Huynh, H. Haick, Self-Healable Sensors based Nanoparticles for Detecting Physiological Markers via Skin and Breath: Towards Disease Prevention via Wearable Devices, Nano Lett. 16 (2016) 4194-4202.

[28] Y. Yang, B. Zhu, D. Yin, J. Wei, Z. Wang, R. Xiong, J. Shi, Z. Liu, Q. Lei, Flexible self-healing nanocomposites for recoverable motion sensor, Nano Energy. 17 (2015) 1-9.

[29] S. Lang, Q. Zhou, Synthesis and characterization of poly(urea-formaldehyde) microcapsules containing linseed oil for self-healing coating development, Progress in Organic Coatings. 105 (2017) 99–110.

[30] M. Behzadnasab, M. Esfandeh, S. M. Mirabedini, M. J. Zohuriaan-Mehr, R.R. Farnood, Preparation and characterization of linseed oil-filled urea–formaldehyde microcapsules and their effect on mechanical properties of an epoxy-based coating, Colloids and Surfaces A: Physicochem. Eng. Aspects. 457 (2014) 16–26.

[31] M. Hasanzadeh, M. Shahidi, M. Kazemipour, Application of EIS and EN techniques to investigate the self-healing ability of coatings based on microcapsules filled with linseed oil and CeO_2 nanoparticles, Progress in Organic Coatings. 80 (2015) 106–119.

[32] T. Szabó, J. Telegdi, L. Nyikos, Linseed oil-filled microcapsules containing drier and corrosion inhibitor – Their effects on self-healing capability of paints, Progress in Organic Coatings. 84 (2015) 136–142.

[33] X. Huang, J. Zhang, M. Lai, T. Sang, Preparation and microwave absorption mechanisms of the Ni Zn ferrite nanofibers, Journal of Alloys and Compounds. 627 (2015) 367–373.

Chapter 3

2-D self-healable polyaniline-polypyrrole nanoflakes based triboelectric nanogenerator for self-powered solar light photo detector

In this chapter, self-powered and self-healable photo detector sensing visible light is demonstrated. Polyaniline-Polypyrrole (PANI-PPY) nano flakes were used in the device and it was prepared using low temperature supported oxidative polymerization procedure. The nano flakes were tested using SEM, FTIR, XRD, and Raman spectroscopy in detail. The formation of the nano flakes is also explained here via thermal scission and surfactant effect. An optical absorption spectra spread was observed in the visible region along with the optical band gap ~1.85eV. The detection was performed using TENG as power supply (maximum voltage ~149 volts, maximum current ~16 μA). With this setup, the nano-flakes showed a sensitivity of ~2.78 %response/mWcm^{-2}. The most novel characteristic of the research presented in this chapter is acetone-supported rapid self-restoration offered in Polyaniline-Polypyrrole (PANI-PPY) nanoflakes, showing maximum healing efficiency ~99.8%.

3.1 Introduction

Triboelectric nanogenerators (TENGs) are known as the next-generation devices to produce environment-suitable, and extremely gainful electrical energy [1]. The development of novel nanoparticles is extremely necessary for maintainable growth in the upcoming years. Increasing demands for energy enhance the demand for progress of self-powered, profitable, self-recoverable futuristic energy-producing devices and methods are extremely crucial in firming small-size electronics [1]. The future battery-less nanogenerators (NGs) based sensors will have a compressed dimension along with huge output power. TENG operates using the principle of triboelectrification as well as electrostatic induction, by which it translates mechanical power to electric power [1]. Materials such as Rhododendron plant [2], decomposable materials like paper [3], and different polymers [4-6] were previously used in TENG fabrication. Despite their outstanding output, TENGs have a chief drawback of deprivation due to repeated mechanical force and environmental degradation. To remove these problems, self-healable materials [SHMs] are incorporated inside NGs. SHMs are widely incorporated in several electronics like solar cells [7-9], supercapacitors [10-12], batteries [13], sensors [14, 15] etc. The incorporation of SHMs in these devices can broadly ease the e-waste problem. In recent years, the TENG based self-powered gas sensors [16-19], humidity sensors [20,21], motion sensors [22-24], pressure sensors [25] etc. are designed. Still, the self-repairing ability is absent in the above battery-less sensing devices. The work presented here focuses on undertaking this problem by incorporating SHM in the device. Electricity conservation is extremely crucial as power production and photodetectors play a chief role in preserving electrical energy.

Here in this work, an extremely responsive self-powered, self-recoverable and conducting polymer (CP) based photodetector for the sensing of solar light is presented. For this purpose, the polyaniline-polypyrrole (PANI-PPY) 2-D nanoflakes (NFs) has been prepared and used in TENG and their output characteristics are observed. The most novel characteristic of this research is acetone-supported rapid self-recovery presented in PANI-PPY nanoflakes.

3.2 Experimental

3.2.1 Materials

Methanol, polyaniline (PANI), cetrimonium bromide (CTAB), polypyrrole (PPY), ammonium persulfate (APS), HCl solution, ethanol (AC grade), and de-ionised water were utilized for PANI-PPY synthesis. These compounds were obtained from Fisher Scientific and utilized in the synthesis process as received. PET films were acquired from Sigma Aldrich.

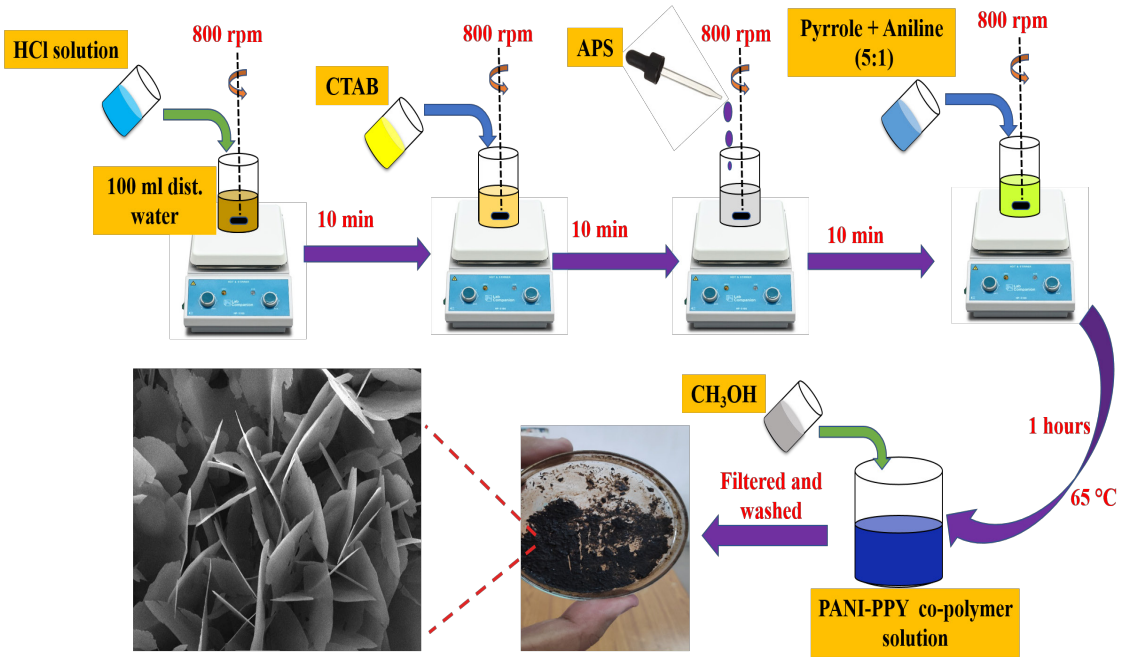

Fig. 3.1 Schematic diagram of steps involved in the synthesis process of PANI-PPY NFs.

3.2.2 Synthesis of PANI-PPY

PANI-PPY was produced using low temperature aided oxidative polymerization method as displayed in Fig 3.1. certain quantity of concentrated hydrochloric acid was diluted in 100 ml of deionized water, and then the beaker was shifted on a stirrer.

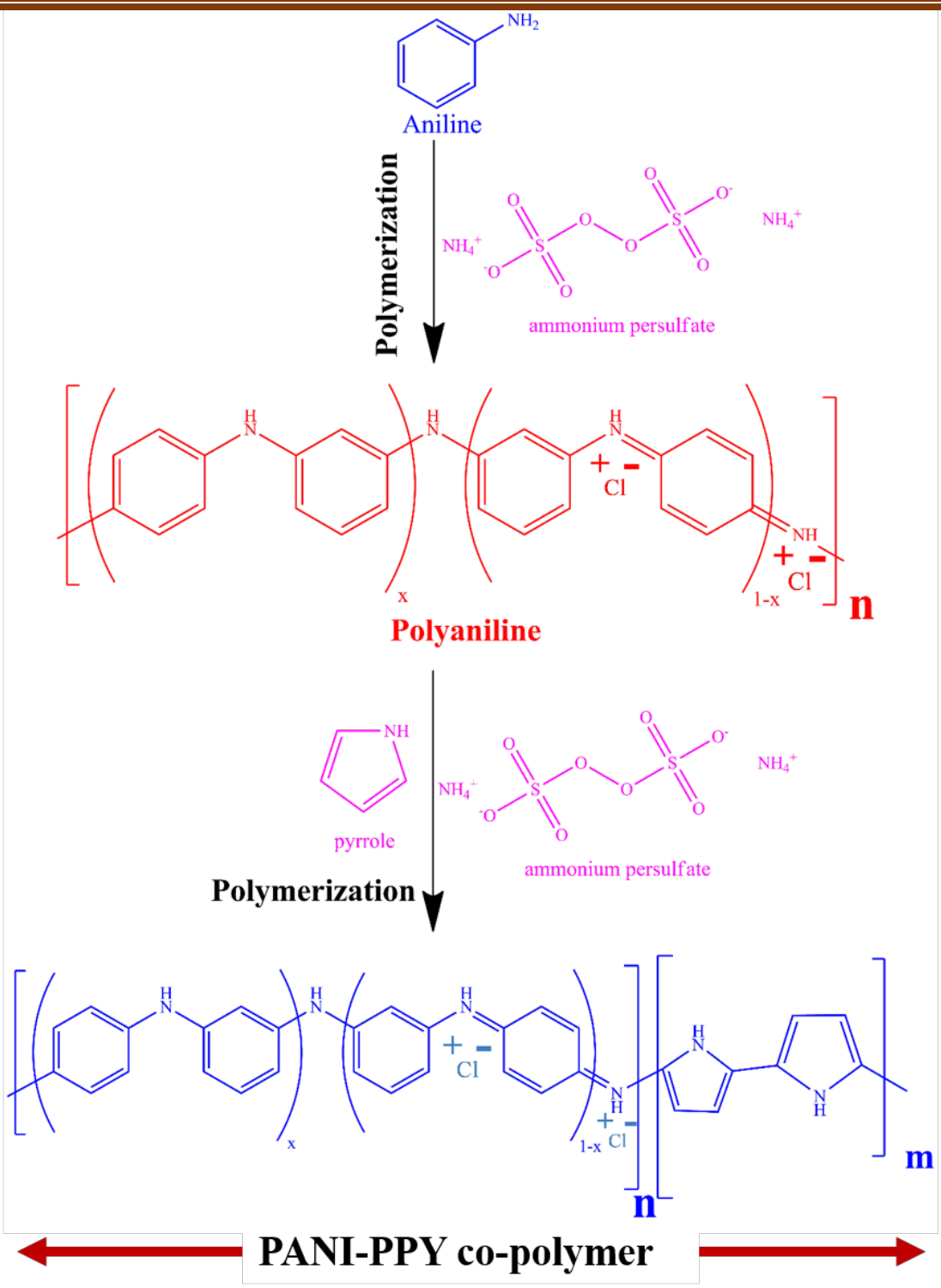

Fig. 3.2. PANI-PPY co-polymer reaction mechanism.

The entire preparation procedure was performed at a rotational speed of 800 rpm. 10 min later, surfactant CTAB was mixed in a concentration of 35 mM for the promotion of the flake-like shapes in the nanomaterial.

APS solution was dropped in the mixture till a precipitate in white colour was observed. PANI and PPY in 1:5 ratio was dropped in the previous mixture. The temperature of solution was upraised towards 65 °C for the next 1 hour. After that CH_3OH was mixed into the mixture to halt polymerization. Finally, the precipitate was cleaned with C_2H_5OH and deionized water. The material was then desiccated at ambient temperature for 1 day, after which the nanoflakes were ready for use.

3.2.3 Reaction mechanism of PANI-PPY formation

PANI-PPY NFs were prepared via the oxidative polymerization procedure as shown in Fig.3.2. At first aniline monomer was mixed in the HCl solution with APS, and initially radical aniline cations were generated. H^+ions from hydrochloric acid solution were utilized in protonation of aniline [26]. This procedure was trailed via an electrophilic replacement method to rejoin these radicals. Monomers used in the reaction comprise their highest responsive de-protonated state. Redox progression of neutral aniline inside solution with oxidizing agent APS begins and in the proliferation phase para-site of this monomer interacts with an oxidized end oligomer of the amino group. With time, the monomers of aniline and APS present in the mixture reduces. Polymerization of Aniline halts after complete reduction of APS or aniline.

Likewise, the polymerization of the monomers of pyrrole occurs in the mixture. The negative ions of the mixture retain electroneutrality of synthesized polymer using the acquisition of the negative ions in the mixture. APS provide e^- towards the pyrrole monomer. Moreover, the π-bond from additional pyrrole was reacted by electron of pyrrole. As a result, a pair formed on creating a free e^- and chain proliferation of polypyrrole starts. The entire mechanism is very similar to polymerization of Polyaniline. Aniline and pyrrole polymerizations occur concurrently in the mixture.

3.2.4 Fabrication of TENG

Copper-tapes (2 mm thick) were stuck to PET film for electrodes. One of these electrodes was stuck to the Kapton film. This Kapton film was scrubbed with sandpaper to improve triboelectricity by increasing its surface coarseness. The second electrode was made by drop casting with PANI-PPY NFs. Overall assembly of the designed TENG is displayed in Fig. 3.3. Both tribo-layers with a surface area of ~32 cm^2 were separated using spacers.

3.2.5 Characterization Techniques

The characterization methods used for analyzing the presence of different elements, bonding, crystal properties, thermal stability, encapsulation, morphology, optical absorption etc. were Fourier transform infrared spectroscopy (FTIR; Thermo-Scientific Nicole 6700), Raman spectroscopy (Renishaw In Via reflex micro-Raman spectrometer), Thermogravimetric analysis (Perkin Elmer Pyris 1 TGA), X-ray Diffraction (XRD; Panalytical - X'Pert Powder) with Cu-Kα radiation (λ~ 1.5418 Å), High-resolution transmission electron microscope (HRTEM; FEI Tecnai TF20) analysis, Scanning electron microscope (SEM; JEOL JSM-6490 LV) and UV–vis spectroscopy (Thermo Scientific-Evolution 201). Thermogravimetric study (TGA) and Differential thermal analysis (DTA) were performed (PerkinElmer Pyris 1 TGA) in a nitrogen environment with 10 °C ramp rate. The electrical measurements of TENG was investigated by Keithley-6517B electrometer.

3.3 Results and discussion

Polymers are widely utilized in NGs and energy storing devices like batteries due to self-recovering and charge holding properties. It is difficult to restrain the shapes in polymer because of their huge agglomeration frequency. Different particles of a monomer can be simply joined to other polymer monomers due to the high accumulation rate during polymerization. Contact electrification quality of nano-scale polymers is significantly amplified due to their great surface-to-volume ratio (S/V).

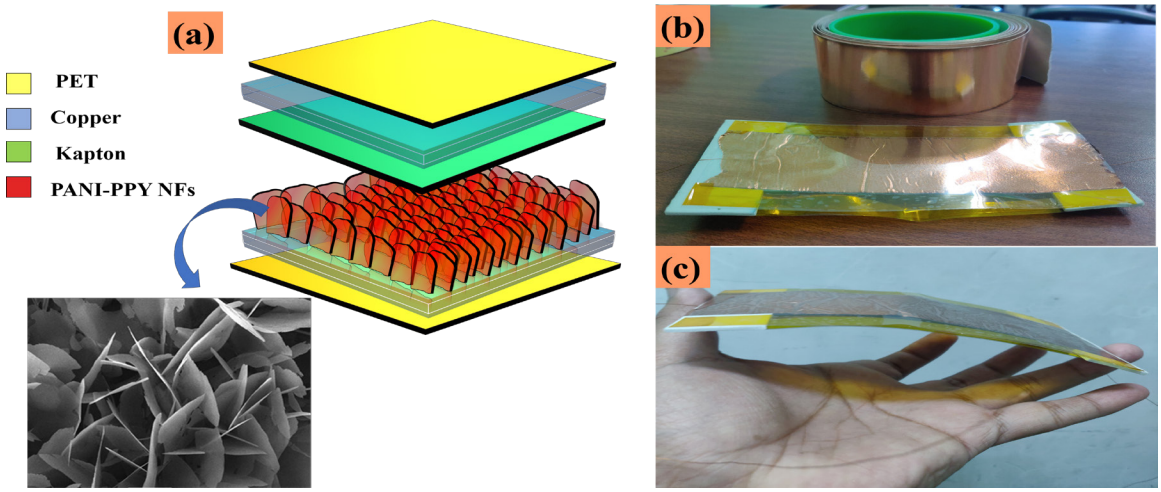

Fig. 3.3. (a) Constituents layers in PANI-PPY based TENG (b) lateral and (c) side-ways images.

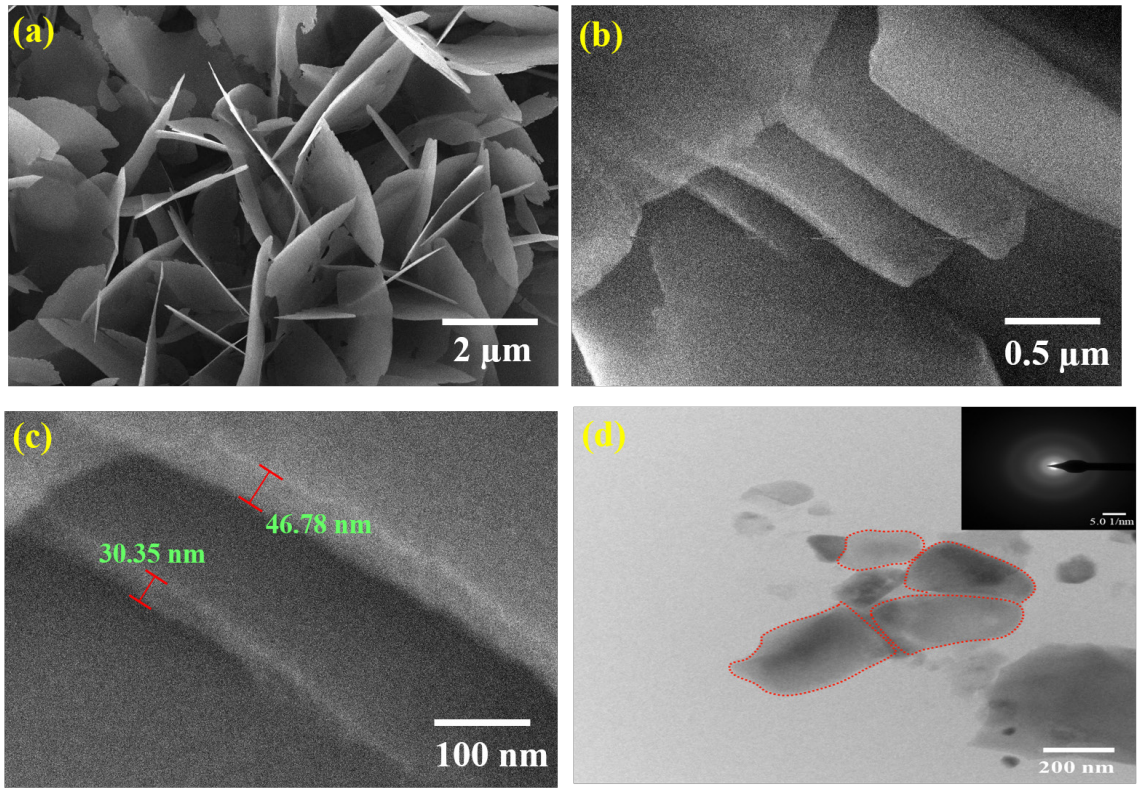

Fig. 3.4. SEM images of (a) Group of NFs, (b) layered NFs and (c) Thickness of NFs ~ 47 nm and (d) TEM image of PANI-PPY NFs with SAED pattern in inset showing semicrystalline defused ring.

The electrical charges produced at the contact are able to be effortlessly received at electrodes with zero waste in TENG, made from conducting polymer (CP). Additional benefit of the development of a polymeric nanostructure is that various nanogenerators [37-46] are constructed with the mixture of inorganic nanomaterials and polymers i.e. in the beginning, an inorganic nanomaterial is prepared, and blended in a polymeric matrix (PVA, PDMS, etc.). Due to the alteration in the mechanical characteristic of both constituents, inner distortion may happen. Furthermore, assume when an extremely conducting nanomaterials like graphene oxide, CNT, graphene etc. are added to polymers with insulating nature, then the overall conductivity of the nano-composite is reduced. The discrepancy present in the internal grain boundaries of the microscale layer gives rise to this characteristic. CNT possess an electrical conductivity of ~10^6-10^8 S/m. When CNTs are dispersed in an insulating polymer matrix, the hybrid structure shows an electrical conductivity of only ~10^2 S/m, as the contact of polymer margins with CNTs arbitrarily in the hybrid. Polymeric nanocomposite can improve the flexibility, and healing capability of the nanocomposite, however, the electron movement is significantly diminished as the resistance and band gap are raised. It is well known that valence and conduction band in CNT overlays, while in CNT-polymer nanocomposite a band gap resides. When the charge is produced after mechanical effort in nanogenerator, it flows throughout the tribo-film to the electrode. If tribo-film is non-conducting, the charges will probably be diffused in the film before approaching an electrode. Output performance of NGs is typically influenced by the proficiency of the collection of the produced charge. If there is an assembly of a huge amount of charges at electrodes before the diffusion, the output performance would upsurge. Conducting polymer in nano dimension improves charge gathering at electrodes and upsurges the total surface extent. So, PANI-PPY based conducting polymer nanosheets are incorporated here.

3.3.1 Electron microscopic analysis

SEM micrographs were taken to examine the exterior features of PANI-PPY nano-flakes. In Fig 3.4(a) group of even and identical NFs are clearly visible, evenly distributed all over. The SEM micrographs validate the reliability of the accepted synthesis procedure

in the creation of identical PANI-PPY NFs. Well-organized NF layers were inspected by aligning the sample platform at an angle of ~50° from y-axis as visualized in Fig. 3.4 (b). A high-resolution SEM micrograph of NFs is displayed in Fig. 3.4(c), where the smallest width of NF is ~30.35 nm.

TEM photographs displayed in Fig. 3.4(d) authenticate the shape and construction of the NFs. While the smallest thickness of nanoflakes (~30 nm) was authenticated from SEM image and the length of NFs was ~ 300 nm. SAED (inset) displays a blurry bright ring-like feature and a glowing epicenter that validates the semi-crystalline nature of the polymer. In polymers, semi-crystallinity resides because of the existence of arrangements repeated over short ranges, established from the XRD analysis (section 3.3.5) as well.

3.3.2 FTIR analysis

FTIR spectra of the copolymer and its constituent individual phases are comparatively shown in Fig. 3.5 (a) and explained in Table 3.1 as well. All the characteristic bands of individual polymer phases were present in the copolymer phase, which confirms the presence of both PPY and PANI phases in the copolymer.

3.3.3 TGA analysis

TGA analysis was executed to validate the thermal behaviour and constancy of the co-polymer. TGA graph presented in Fig. 3.5 (b) shows the deteriotion of PANI-PPY in three steps. 1st phase is visualized at about 75-130 °C due to the loss of adsorbed water from the sample. 2nd stage is visualized at 230-460 °C, when the tiny oligomers get excluded and the ions doped in the polymer are decayed. The disintegration at the 3rd stage was visualized at 510 °C and beyond, due to the obliteration of the chains of the polymer. It was observed that at the termination of the 2nd stage, ~ 43 ± 1 % of the sample was decayed. Therefore, only ~ 57 ± 1 % material remained at high temperatures. These annotations from Fig. 3.5 (b) display the good thermal steadiness of the synthesized material.

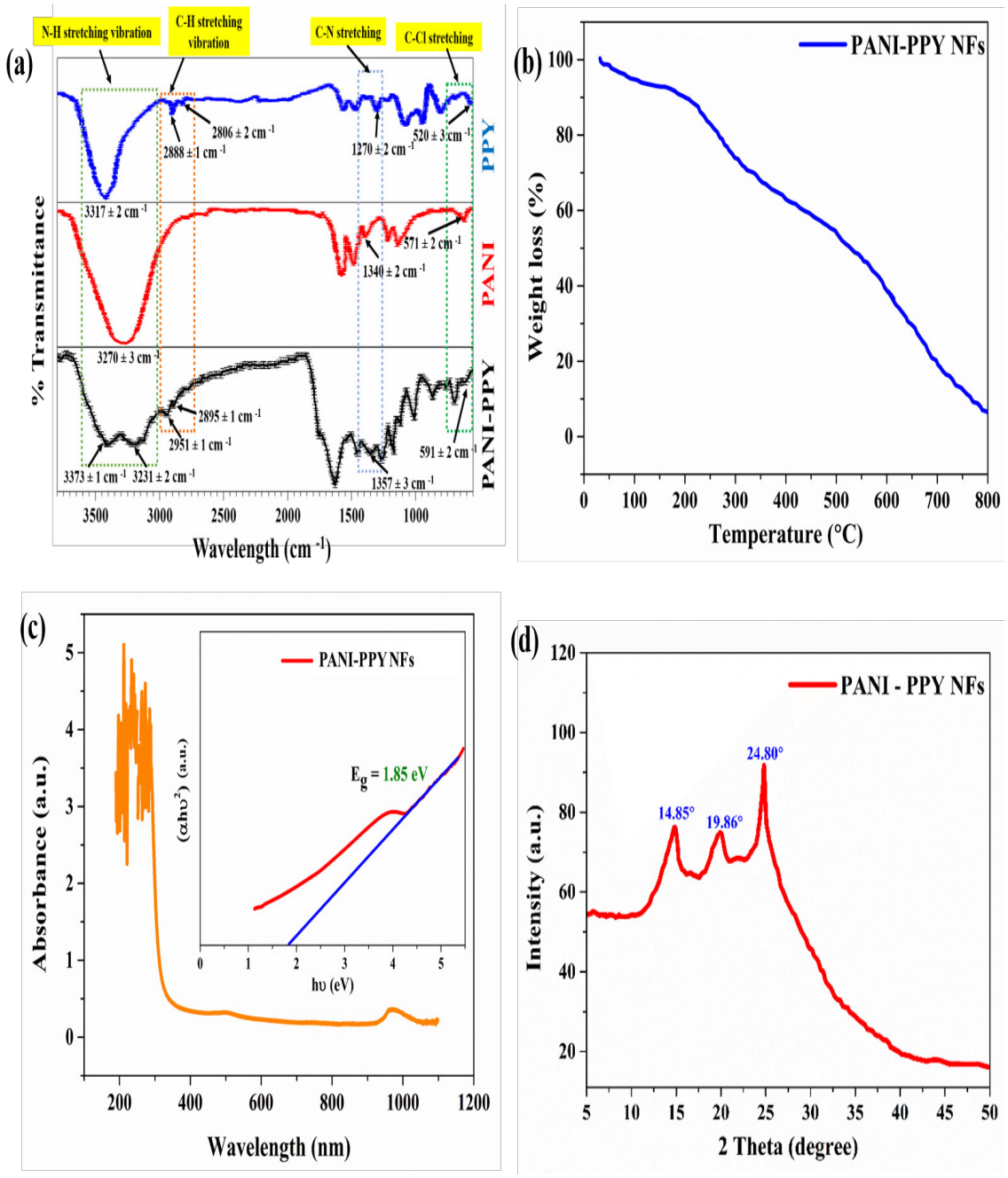

Fig. 3.5. (a) Stacked FTIR spectra of PPY, PANI and PANI-PPY for comparative analysis (b) TGA analysis of PANI-PPY copolymeric NFs (c) UV–Visible absorption spectra with Tauc plot for bandgap observation of PANI-PPY composite (d) XRD of PANI-PPY NFs showing semi-crystalline nature.

Table 3.1 FTIR peaks in PPY, PANI and PANI-PPY with corresponding assignments.

Peak in PPY (cm-1)	Peak in PANI (cm^{-1})	Peak in PP (cm^{-1})	Assignment
3317	**3270**	**3373**	N—H stretching
2888	**—**	**2951**	C—H stretching
2806	**—**	**2895**	C—H stretching
1524	**1543**	**1626**	C═C stretching
1460	**1449**	**1454**	C═C stretching
1270	**1340**	**1357**	C—N stretching
1038	**1167**	**1026**	C—H stretching
520	**571**	**591**	C—Cl stretching

3.3.4 UV-Visible spectroscopy

It is vital to discuss that the band gap of utmost effective photovoltaic constituents lies between 0.5-2.5 eV [27]. Presented NFs reveal bandgap in the same array. The graph amid the energy of photon (hν) and coefficient of optical absorption (α) is graphed as per displayed in Fig. 3.5 (c) for achieving band gap (E_g):

$$\alpha h\nu = A\,(h\nu - E_g)^p \qquad (3.1)$$

where A signifies a constant, ν represents the exact frequency needed in transition, p shows the kind of transition taking place. The $(\alpha h\nu)^2$ vs hν plot, also known as Tauc plot is drawn that displays a bandgap ~1.85 eV as shown in Fig. 3.5 (c).

3.3.5 XRD analysis

Fig. 3.5 (d) displays the XRD configuration of PANI-PPY copolymer. The representative diffraction of PPY is noticed at Bragg angle 25°, while in case of PANI, diffraction occurs at 25°, 20° and 15° corresponding to (200), (020) and (011) planes [28]. Strident diffraction at 25° resembles face-to-face inter-chain piling of phenyl rings. Wide raised peaks at 24.80°, 19.86°, and 14.85° display the semi-crystal like behaviour of polymer. The observed diffraction at 19.86° is related to cyclicity parallel with the polymeric chain, and the diffraction detected at 24.80° exists owing to cyclicity perpendicular with polymer chains. The semi-crystal-like nature of the copolymer is the consequence of the inclusion of semi-crystalline PANI [28]. The emi-crystals are also validated by SAED in HR-TEM section (section 3.3.1). These outcomes coincide with earlier testified copolymeric XRD [29] and display the purity of synthesized material.

3.3.6 Raman analysis

Raman spectra study of the copolymer is displayed in Fig. 3.6. The existing Raman active modes with their positions and assignments are shown in Table 3.2.

Table 3.2 Raman active modes of PANI-PPY copolymer.

Raman shift (cm^{-1})	**Assignment**
1558	C—C stretching
1455	quinoid ring's C═N stretching
1333	C—N^+ stretching
1119	C—H in-plane bending

1004	quinoid polaron structure of Polypyrrole
970	quinoid bi-polaron structure of Polypyrrole
900	in-plane distortion of benzenoid ring of polyaniline
836	in-plane distortion of quinoid of polyaniline
749, 539	C—Cl stretching

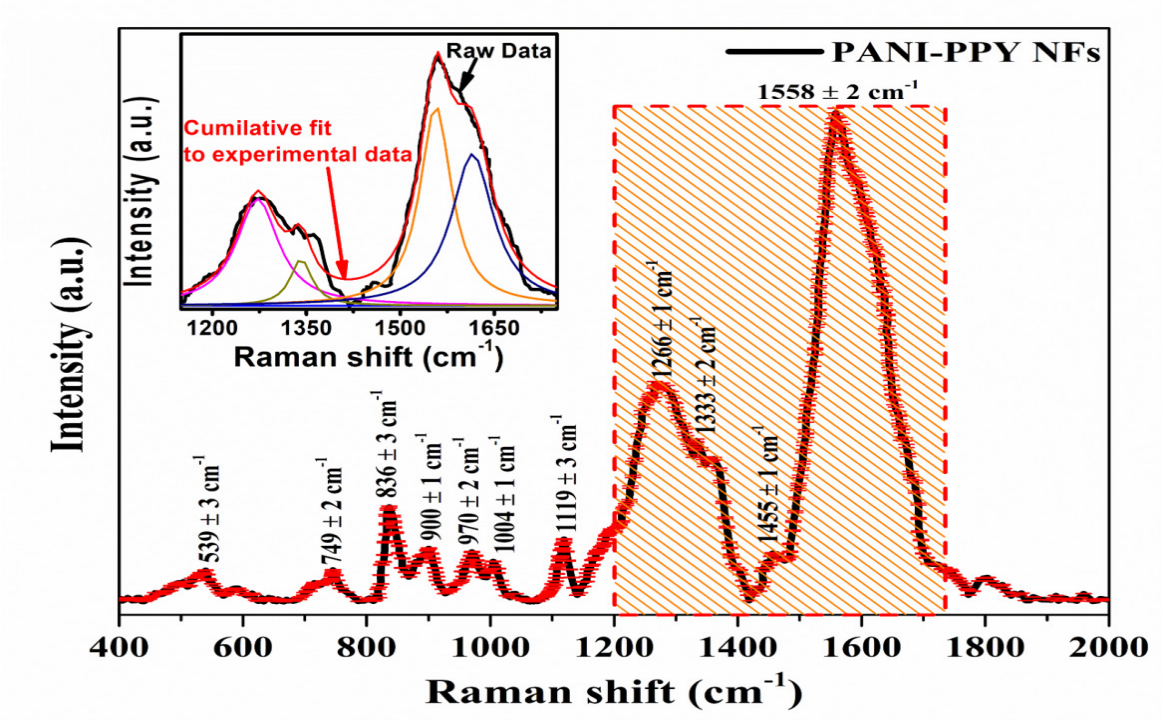

Fig. 3.6. Raman spectra of synthesized conducting PANI-PPY polymeric NFs.

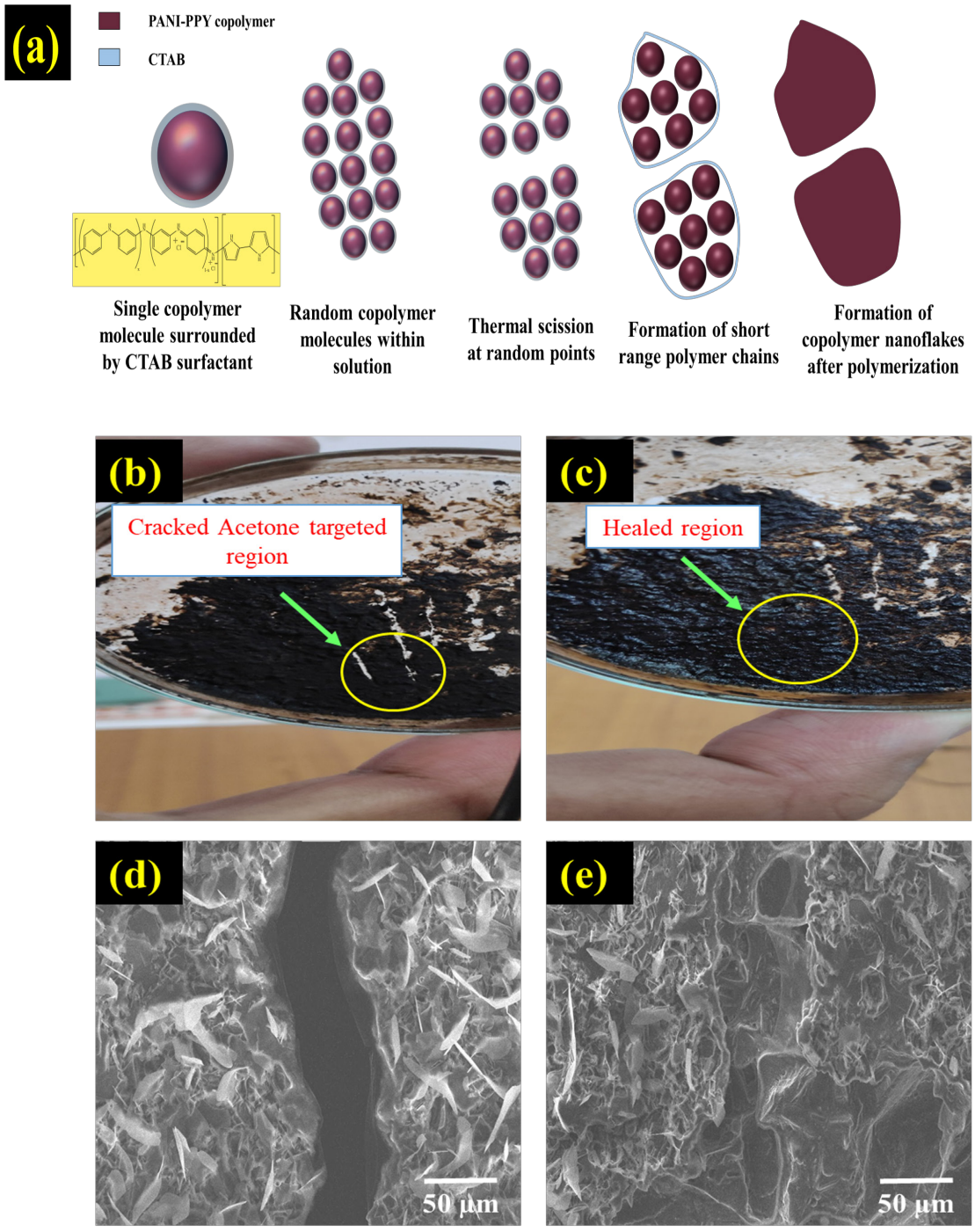

Fig. 3.7. (a) PANI-PPY nanoflakes formation mechanism, (b) optical image of a cracked film, (c) optical image of the healed film, (d) SEM image of a crack generated film, and (e) SEM image of the healed film.

3.3.7 NFs formation process and Self-recovering ability

The formation of every nanoparticles with specific shape requires well-ordered and accurate control. The PANI-PPY polymerization was analyzed in section 3.2.3. The process of NFs development is revealed in Fig. 3.7 (a). The applied temperature of 65 °C and CTAB surfactant are the main keys in the development of NFs. Numerous molecules comprise of PPY and PANI produce when polymerization begins. These molecules are rapidly enclosed by surfactant, which halts these polymer molecules from accumulation. After the temperature was raised towards 65 °C, the process of thermal division arises at random places in the solution [59] and thus short-chained polymer in place of long-ranged polymer is created. These low-range molecules converged and polymerized in a single plane to produce a flake-like assembly. SEM study in Fig. 3.4(a), (b) and (c) validate finely detached 2-D NFs.

To examine the ability of restoration of the NFs, both SEM and optical imaging are performed. For this, the film was itched using a spatula as presented in Fig. 3.7 (b) and (d), the healing phenomenon was observed in the ambient environmental state. Figures 3.7(c) and 3.7(e) exhibit how rapid the healing was originated in the PANI-PPY under only 10 minutes after the inclusion of a few acetone drops, which were dropped using a micropipette. Each copolymer molecule was connected with each other by frail hydrogen and π-bondings [60], that is able to be simply shattered with acetone. When acetone dehydrates, these bonds reestablishes and the crack gets sealed (Fig. 3.7 (c),(e)). Reaction between acetone and the polymer does not disturb the morphological and electrical characteristics of nano-flakes that is clearly visualized in segment 3.3.8.

3.3.8 Self-powered Photo-detection

A graphical picture of the battery-less solar light photo-detector is displayed in Fig. 3.8 (a). Here, PANI-PPY based TENG (section 3.2.4) is utilized to supply the sensor required power for operation. The electrodes of TENG are coupled to a different resistive copolymer film, which behaves like a photo-sensing element. When illuminations of diverse power densities are radiated on this sensing film, it behaves as a changeable

resistor. The potential drop through this resistive film was observed using Keithley electrometer (6517B). A PC linked to the electrometer saves the output data produced. The copolymer film on the glass substrate was positioned inside the detection compartment that is linked to a light intensity controller as can be seen in Fig. 3.8 (a). Photo-sensing setup is completely secured to evade mistakes owing to exterior light sources.

On this context, the discussion of the fundamental working principle of self-powered sensing devices is very crucial. These devices operate on the norm of a voltage divider (Fig. 3.8 (b)) that precisely imitates the self-powered Photo sensing circuit displayed in Fig. 3.8 (a).

The output coming from the nanogenerator plays the role of the input voltage source V_{IN} for the sensing element to work. R_1 is the interior resistance of NG and circuit, whereas R_2 denotes the resistance of sensing film. The potential drop across R_2:

$$\mathbf{V_{OUT} = \{R_2/(R_1 + R_2)\} \times V_{IN}} \qquad \mathbf{(3.2)}$$

Equation 3.2 displays that voltage drop across R_2 is proportionate with R_2. Therefore, any change in R_2 will change V_{OUT} as well. The working of a self-powered sensing devices can be simply realized by this concept. The voltage produced by the TENG works as input voltage V_{IN} for the sensing film. When light is made to fall on the sensing element R_2, the electrical resistance of the material rapidly varies. As the resistance of sensing film varies, voltage drops through the sensing element, hence V_{OUT} also alters. Diverse kinds of earlier testified self-powered sensors operate on a similar principle [16,18,20,21].

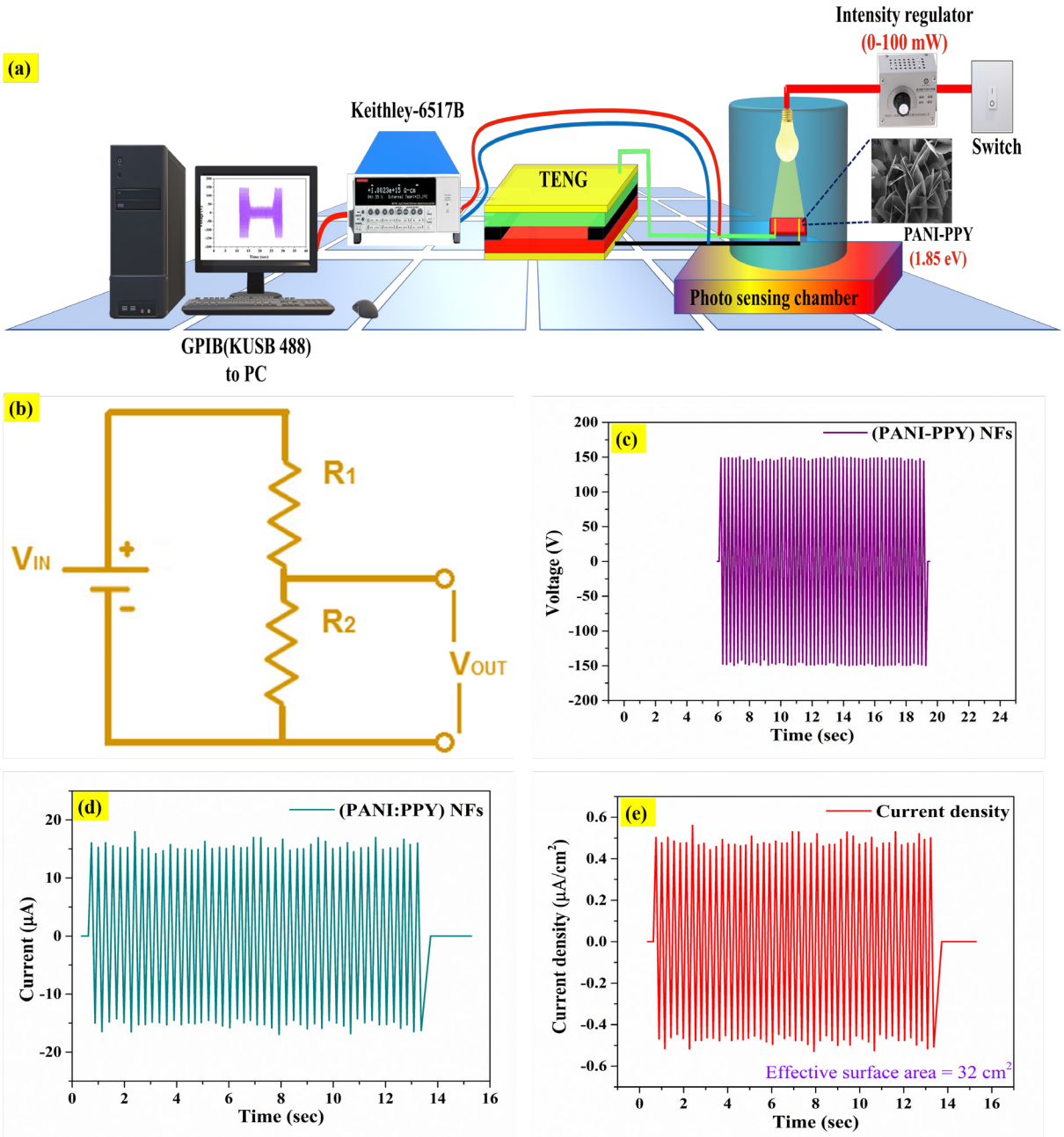

Fig. 3.8. (a) Schematic diagram of self-powered visible light photodetection unit, (b) circuit diagram of voltage divider circuit, (c) Max output voltage of PANI-PPY based TENG, (d) Max output current of PANI-PPY based TENG, and (e) Current density graph of PANI-PPY TENG.

After a detailed literature review, it was found that present PANI-PPY NFs have an improved response/recovery time than previously reported works. Furthermore, this work displays self-healing functionality accompanied by the self-powered property that is the originality of the following study.

The output characteristics of the co-polymer based TENG were investigated under the influence of a perpendicular force (contact-separation mode), which is compressive in nature. For this work, repeatedly pressing by fingers, was applied on the TENG. An open-circuit voltage as high as ~149 volts was attained as displayed in Fig. 3.8 (c). A steady current of 16 ~μA was detected, which demonstrates the permanency of the device. The observed standard deviation in current is 0.7730 μA and the relative standard deviation (RSD) is 4.97 %. These observations illustrate that device generated current is very steady. The power density generated in this device was 83.56 μWcm^{-2} (surface area of TENG ~32 cm^2), while the current density achieved was ~0.56 μAcm^{-2}.

Functioning of the TENG-based solar light photo sensor can be understood by understanding the working of resistance variation during the ON/OFF switching process. The PANI-PPY based resistive film that behaves like a photo sensing element was positioned inside the sensing compartment as exposed in Fig. 3.8 (a). As soon as the material was exposed to open air, oxygen ions get chemisorbed on the exterior of the material as displayed in Eqns. 3.3, 3.4 and 3.5.

$$O_2\,(ads) + e^- \leftrightarrow O_2^-(ads) \qquad (3.3)$$

$$O_2\,(ads) + 2e^- \leftrightarrow 2O^-(ads) \qquad (3.4)$$

$$O^-(ads) + e^- \leftrightarrow O_2^-(ads) \qquad (3.5)$$

Electron-hole pairs are formed when the film is illuminated with light. When the film is endlessly radiated with photons, some electrons get adequate energy for jumping beyond the potential wall to travel from conduction band to valance band.

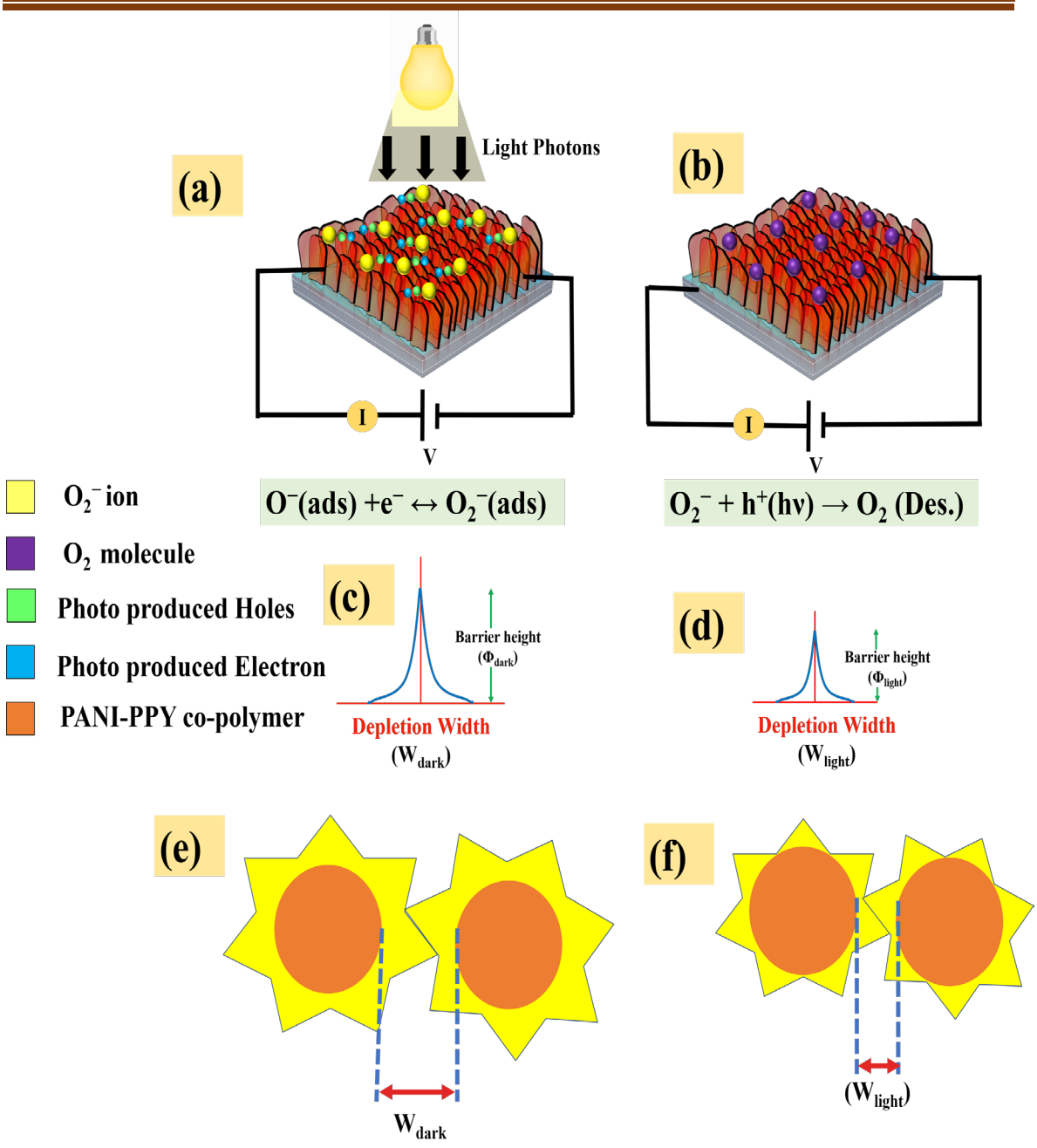

Fig. 3.9. (a) Electron-hole pair production due to visible light and creation of O_2^- ions, (b) alteration of O_2^- ions into O_2 molecule due to photo-produced holes (c) increment of barrier height under dark conditions (d) deduction of barrier height under illumination (e) Formation of O_2^- ions layer (yellow colour) before illumination and (f) deduction of O_2^- ion layer due to interaction of photogenerated holes.

These photo-generated holes react with chemisorbed oxygens and desorb them immediately into oxygen molecule as,

$$O_2^- + h^+(h\nu) \rightarrow O_2 \text{ (Des.)} \qquad (3.6)$$

After this development, because of the remaining unpaired electrons, the resistance drops as depletion width is lessened (Fig. 3.9 (d) and 3.10 (a)). As the light intensity or the illumination time is upsurged, a huge quantity of e-h sets gets produced. This creates an additional reduction in electrical resistance. In dark, oxygen molecules begin to adsorb on the material again by forming O_2^- ions. This aids in the increment of resistance as displayed in Fig. 3.10 (a).

Fig. 3.10 (a) demonstrates the variation in resistance of the material in the presence of solar light (100 mW/cm^2). As discussed earlier in Fig. 3.8 (b), the achieved voltage drop through sensing element varies with its resistance. Fig. 3.10 (b) shows the reduction in voltage across film when film resistance reduces with the rise of irradiance of solar light. The produced voltage of 126.4, 83.6, and 39.4 volts across the sensing film was obtained under the different intensities of the light of 30, 60, and 100 mW/cm^2. As light of 100 mW/cm^2 was put on the sample, the voltage was changed from 149 volts to 39 volts. The least response/recovery times were observed for 30 mW/cm^2, which are 0.41 sec and 0.45 sec as displayed in Fig. 3.10 (c). The % sensor response and sensor response were measured using Eqns. 3.7 & 3.8 [26]:

$$\%\ \textbf{sensor reponse} = (V_{NI} - V_I)/V_I \times 100 \qquad (3.7)$$

$$\textbf{sensor reponse} = V_{NI}/V_I \qquad (3.8)$$

Here, V_I and V_{NI} and represent voltages produced without any illumination and with illumination (30, 60 and 100 mW/cm^2). The %sensor responses and sensor responses at 0, 30, 60 and 100 mW/cm^2 illumination were observed to be 0, 17.78, 78 and 278 %, and 1.00, 1.18, 1.78 and 3.78 correspondingly. Sensitivity is gradient of calibration graph that is 2.78 %response/mWcm^{-2}.

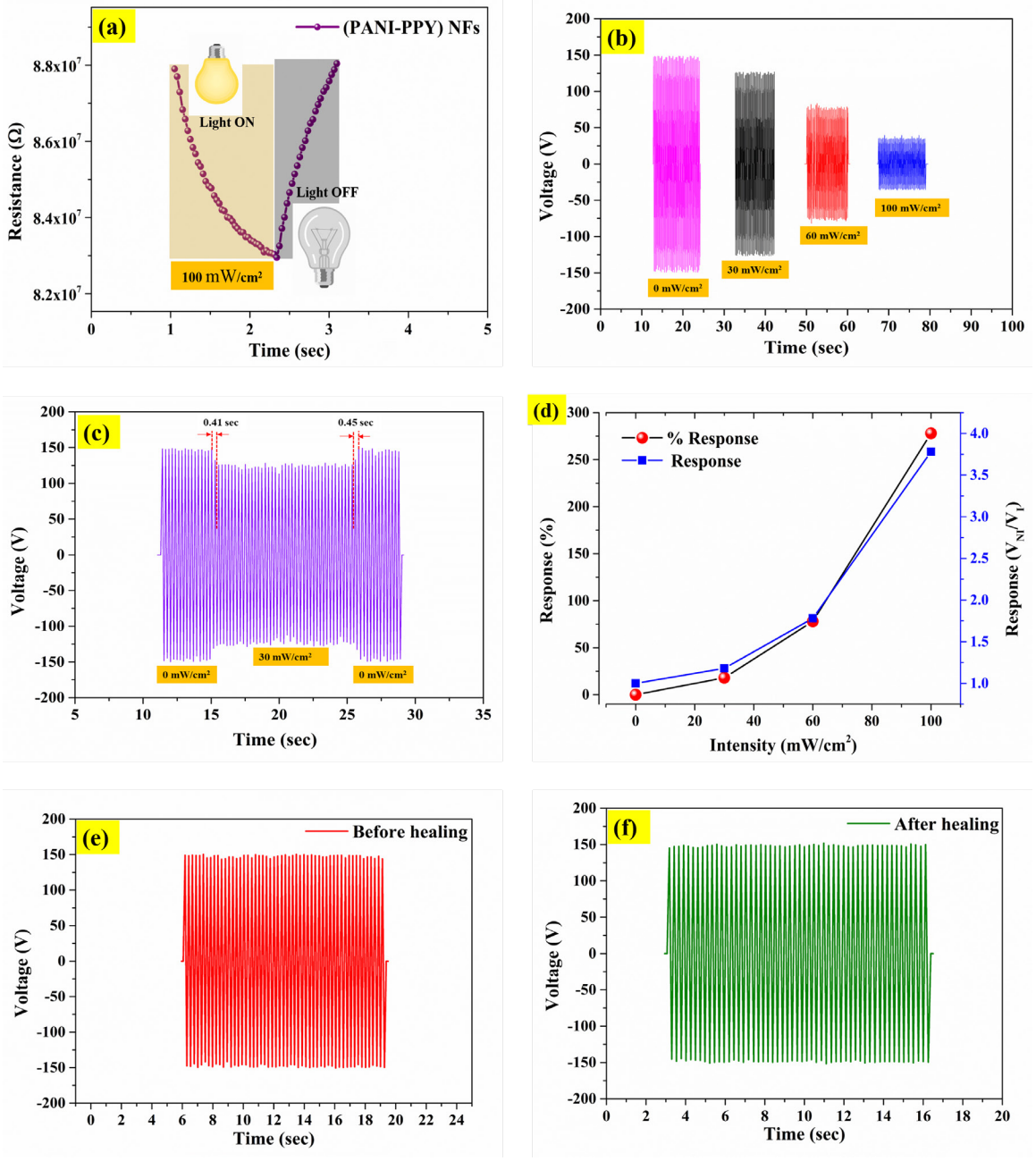

Fig. 3.10. (a) Variation of resistance under illumination and dark, (b) Maximum output voltage under various incident visible light intensities, (c) Change in output voltage when 0 to 30 mW/cm^2 to calculate response and recovery time of photosensor, (d) % response and response curve of the photosensor, maximum output voltage (e) before healing and (f) after healing.

A very significant findings of this research work is the investigation of the the consequence of self-healing on the device's output behaviour. It was achieved by cracking the sensing film using a spatula and then healing it with acetone. The voltages recorded pre and post-healing were 149.2 volts and 149 volts respectively as presented in Fig. 3.10 (e) and (f). It is fascinating to observe that not any significant variations were perceived in the produced voltage that confirms the healing capability and electrical recovery in the TENG. The power density in the healed material was 83.54 μWcm^{-2}. A negligible variation of only 0.02 μWcm^{-2} displays the efficacy of self-healing. Moreover, it demonstrates an insignificant modification in the S/V ratio also occurred post healing.

3.4 Conclusion

In conclusion, we have demonstrated PANI-PPY NFs with self-healing ability prepared via a simple chemical method with the application in self-powered photo sensor. The method of preparation is very simple to form nano-dimension (~30 nm) 2-D NFs. Self-healing ability was found absent in earlier published self-powered photo sensors that are able to change the output enactment of the device after damage. TENG measurements were made to explore the ability of TENG. A highest voltage and current of 149 volts, and 16 µA, maximum current density and power density of 0.56 μAcm^{-2}, and 83.56 μWcm^{-2} were obtained from this sensing scheme that illustrates greater performance against the previously testified self-powered sensors. Thus, this work emphasizes the advancements in self-recoverable and self-powered photo sensors.

References

[1] Y. J. Tan, J. Wu, H. Li, B. C. K. Tee, Self-Healing Electronic Materials for a Smart and Sustainable Future, ACS Appl. Mater. Interfaces 10 (2018) 15331−15345.

[2] F. Meder, I. Must, A. Sadeghi, A. Mondini, C. Filippeschi, L. Beccai, V. Mattoli, P. Pingue, B. Mazzolai, Energy conversion at the cuticle of living plants, Adv. Funct. Mater. 28 (2018) 1806689.

[3] Y. Chi, K. Xia, Z. Zhu, J. Fu, H. Zhang, C. Du, Z. Xu, Rice paper-based biodegradable triboelectric nanogenerator, Microelectron. Eng. 216 (2019) 111059.

[4] W. Zhong, L. Xu, H. Wang, J. An, Z. L. Wang, Tilting-Sensitive Triboelectric Nanogenerators for Energy Harvesting from Unstable/Fluctuating Surfaces, Adv. Funct. Mater. 29 (2019) 1905319.

[5] T. X. Xiao, X. Liang, T. Jiang, L. Xu, J. J. Shao, J. H. Nie, Y. Bai, W. Zhong, Z. L. Wang, Spherical Triboelectric Nanogenerators Based on Spring Assisted Multilayered Structure for Efficient Water Wave Energy Harvesting, Adv. Funct. Mater. 28 (2018) 1802634.

[6] J. P. Lee, J. W. Lee, J. M. Baik, The Progress of PVDF as a Functional Material for Triboelectric Nanogenerators and Self-Powered Sensors, Micromechanics 9 (2018) 532.

[7] D. Wang, M. Wright, N. K. Elumalai, A. Uddin, Stability of Perovskite Solar Cells. Sol. Energy Mater. Sol. Cells 147 (2016) 255−275.

[8] Y. Zhao, J. Wei, H. Li, Y. Yan, W. Zhou, D. Yu, Q. Zhao, A polymer scaffold for self-healing perovskite solar cells, Nat. Commun. 7 (2016) 10228.

[9] F. Lang, N. H. Nickel, J. Bundesmann, S. Seidel, A. Denker, S. Albrecht, V. V. Brus, J. Rappich, B. Rech, G. Landi, et al. Radiation Hardness and Self-Healing of Perovskite Solar Cells. Adv. Mater., 28 (2016) 8726−8731.

[10] Y. Huang, Y. Huang, M. Zhu, W. Meng, Z. Pei, C. Liu, H. Hu, C. Zhi, Magnetic-Assisted, Self-Healable, Yarn-Based Supercapacitor, ACS Nano, 9 (2015), 6242−6251.

[11] H. Sun, X. You, Y. Jiang, G. Guan, X. Fang, J. Deng, P. Chen, Y. Luo, H. Peng, Self-Healable Electrically Conducting Wires for Wearable Microelectronics. Angew. Chem. Int. Ed., 53 (2014) 9526−9531.

[12] H. Wang, B. Zhu, W. Jiang, Y. Yang, W. R. Leow, H. Wang, X. Chen, A Mechanically and Electrically Self-Healing Supercapacitor. Adv. Mater., 26 (2014) 3638−3643.

[13] Y. Sun, J. Lopez, H. W. Lee, N. Liu, G. Zheng, C. L. Wu, J. Sun, W. Liu, J. W. Chung, Z. Bao, A Stretchable Graphitic Carbon/Si Anode Enabled by Conformal Coating of a Self-Healing Elastic Polymer. In Materials Engineering and Sciences Division 2016 - Core Programming Area at the 2016 AIChE Annual Meeting, 2 (2016) 532−538.

[14] S. Singh, A. Bhaduri, R. K. Tripathi, K. B. Thapa, R. Kumar, B. C. Yadav, Improved sensing behaviour of self-healable solar light photodetector based on core-shell type Ni0.2Zn0.8Fe2O4@ poly (Urea-Formaldehyde), Solar Energy, 188 (2019) 278–290.

[15] A. Bhaduri, S. Singh, R. K. Tripathi, U. Kumar, K. B. Thapa, B. C. Yadav, Healable, highly sensitive LPG sensor based on Ni0.4Zn0.6Fe2O4 nanohybrid grown by autocombustion process, Sensors & Actuators: B. Chemical, 327 (2021) 128840.

[16] A. S. M. I. Uddin, P. S. Kumar, K. Hassan, H. C. Kim, Enhanced sensing performance of bimetallic Al/Ag-CNF network and porous PDMS-based triboelectric acetylene gas sensors in a high humidity atmosphere, Sensors and Actuators B: Chemical, 258 (2018) 857-869.

[17] S. Wang, Y. Jiang, H. Tai, B. Liu, Z. Duan, Z. Yuan, H. Pan, G. Xie, X. Du, Y. Su, An integrated flexible self-powered wearable respiration sensor, Nano Energy, 63 (2019) 103829.

[18] S. Cui, Y. Zheng, T. Zhang, D. Wang, F. Zhou, W. Liu, Self-powered ammonia nanosensor based on the integration of the gas sensor and triboelectric nanogenerator, Nano Energy, 49 (2018) 31-39.

[19] K. Zhao, G. Gu, Y. Zhang, B. Zhang, F. Yang, L. Zhao, M. Zheng, G. Cheng, Z. Du, The Self-Powered CO_2 Gas Sensor Based on Gas Discharge Induced by Triboelectric Nanogenerator, Nano Energy, 53 (2018) 898-905.

[20] D. Zhang, Z. Xu, Z. Yang, X. Song, High-Performance Flexible Self-Powered Tin Disulfide Nanoflowers/Reduced Graphene Oxide Nanohybrid-Based Humidity Sensor Driven by Triboelectric Nanogenerator, Nano Energy, 67 (2020) 104251.

[21] Y. Su, G. Xie, S. Wang, H. Tai, Q. Zhang, H. Du, X. Du, Y. Jiang, Self-Powered Humidity Sensor based on Triboelectric Nanogenerator, IEEE Sensors, 17467255 (2017) 1-3.

[22] J. Chen, H. Guo, Z. Wu, G. Xu, Y. Zi, C. Hu, Z. L. Wang, Actuation and sensor integrated self-powered cantilever system based on TENG technology, Nano Energy 64 (2019) 103920.

[23] Z. Wu, W. Ding, Y. Dai, K. Dong, C. Wu, L. Zhang, Z. Lin, J. Cheng, Z. L. Wang, Self-Powered Multifunctional Motion Sensor Enabled by Magnetic-Regulated Triboelectric Nanogenerator, ACS Nano, 12 (2018) 5726−5733.

[24] L. Jin, J. Tao, R. Bao, L. Sun, C. Pan, Self-powered Real-time Movement Monitoring Sensor Using Triboelectric Nanogenerator Technology, Scientific Reports 7 (2017) 10521.

[25] V. Vivekananthan, A. Chandrasekhar, N. Rao Alluri, Y. Purusothaman, S. J. Kim, A highly reliable, impervious and sustainable triboelectric nanogenerator as a zero-power consuming active pressure sensor, Nanoscale Adv., 2 (2020) 746-754.

[26] S. J, Tang, A. T. Wang, S. Y. Lin, K. Y. Huang, C. C. Yang, J. M. Yeh, K. C. Chiu, Polymerization of aniline under various concentrations of APS and HCl, Polymer Journal (2011) 43, 667–675.

[27] A. Polman, M. Knight, E. C. Garnett, B. Ehrler, W. C. Sinke, Photovoltaic materials: Present efficiencies and future challenges, Science, 352 (2016) 4424.

[28] Y. Zhang, J. Liu, Y. Zhang, J. Liu, Yuping Duan, Facile synthesis of hierarchical nanocomposites of aligned polyaniline nanorods on reduced graphene oxide nanosheets for microwave absorbing materials, RSC Adv., 7 (2017) 54031.

[29] H. Mi, X. Zhang, X. Ye, S. Yang, Preparation and enhanced capacitance of core–shell polypyrrole/ polyaniline composite electrode for supercapacitors, Journal of Power Sources 176 (2008) 403–409.

Chapter 4

Gigantic stimulation in response by solar irradiation in self-healable and self-powered LPG sensor based on triboelectric nanogenerator

Visible light induced, self-powered and self-recoverable LPG senor is reported in this chapter. The operating voltage was supplied by TENG fabricated in the laboratory. The utilization of unused energy (finger tapping) for functioning sensors to maintain green and sustainable development have been employed. 2-dimensional PANI-PPY (2P) nanosheets were prepared and employed as PDMS/PANI-PPY (3P) based TENG. The TENG reveals huge output voltage and current. 3P polymeric nanocomposite also displayed fast self-recovering competency under 35 min. The 2P-based film was used in the recognition of LPG at room temperature under visible light illumination.

4.1 Introduction

Due to their applicability in developing imperishable energy-centred, sustainable, self-driven, highly efficient sensors detecting pressure, humidity, light, gases etc., nanogenerators have been investigated and modified in the last few years [1,2]. Conventional gas detectors need an external power source and external heating equipment for producing good sensing behaviour with high and fast response [3,4]. The addition of nanogenerators in these sensors cut off the need for an external power source as the output voltage of the nanogenerators can directly be used to operate the sensor. LPG is an exceedingly combustible gas with a lower explosive limit as low as ~2.2 vol.%, and is widely used by mankind as a fuel source [5,6]. The early detection of leaked LPG is exceptionally important, as the number of LPG consumers is rising sharply day by day. For decades, metal oxides (ZnO, CdO, MgO etc.), polymers (polypyrrole, polyaniline), and different nanohybrids (Nb_2O_5/PANI, CdO/graphene, PANI/CNT etc.) have been explored in LPG detection [8-10]. However, most of these sensors need high temperature for operation and are mostly not self-powered. Many attempts have been taken to remove the temperature barrier in gas sensing applications. In this context, light-induced gas sensing is one of the newest and very effective methods in room temperature gas sensing. Here, photon energy is utilized to boost the gas detection capabilities of the material at room temperature (RT). However, the usage of this technique in LPG sensing is rather new. Combining the photo-enhanced LPG sensors with nanogenerators can considerably improve the sensing behaviour, decrease the operating cost and prevent any accidents (due to high temperature) in the device [11, 12].

TENG operates on the concepts of combined effect of electrification on contact, and electrostatic induction, which generated comparatively higher output voltage than other kinds of nanogenerators [46]. Yet, the nonstop mechanical process causes structural damage in TENG. This obstacle can be removed by introducing self-healing material inside the TENG matrix. The self-healing materials can regain their original structure afterwards without any mechanical damage. Hence using self-healing materials, the working life can be enhanced and the production cost of the devices can be reduced significantly. Inclusion of self-recovery in electronic devices lowers the

generation of electronic waste, which is a serious global issue. The usage of self-healing materials in these devices also reduces the number of toxic materials released from electronic waste. Toxic elements like Pb, Cd, Cu etc. get mixed from the e-waste in the natural water sources and soil, causing serious health and environmental issues [14-16].

Polymeric materials have been utilized extensively in sensors, batteries, supercapacitors, self-healing, and nanogenerators for being highly stable and non-toxic in nature. To make the material highly responsive towards gas, it can be illuminated with light instead of applying external temperature. For this application, the optical band gap of the utilized sensing material is a very important factor. The band gap of the used material decides the energy needed to activate the photocatalytic property of the material. According to Plank, the energy (E) of the photon can be related to its wavelength (λ) [17],

$$\mathbf{E = hc/\lambda = 1240\ eV/\lambda} \qquad \mathbf{(4.1)}$$

From this relation, it can be realised that the materials utilizing the visible part of the falling light should possess a band gap between ~ 1.7 to 3.1 eV. At a higher band gap, the material would be activated by UV light. The adsorption rate of the oxygen molecules can be expressed as Eqn.4.2:

$$\boldsymbol{R_{ads} = R^{0}_{ads} e^{-E_{ads}/RT} + R^{I}_{ads}(\lambda, I)} \qquad \mathbf{(4.2)}$$

Where R_{ads}, R^{0}_{ads}, E, R, T, R^{I}_{ads}, λ and I are the rate of adsorption of O_2, maximum rate of adsorption of O_2 on exterior driven by temperature, temperature of the material surface, rate of adsorption of O_2 on material surface driven by photons, wavelength and intensity of light used. Eqn. 4.2 gives an idea of how the adsorption rate depends on the operating temperature and irradiation. The adsorption rate is proportional to the exponential of inverse of applied temperature, whereas, it is directly proportional to the wavelength of the applied light. Clearly, at room temperature, the effect of light is dominant in the adsorption rate. Hence, we can get improved sensing properties at room temperature by illuminating the sample with light of certain energy.

Therefore, a detailed investigation for developing a self-powered, self-healable, and visible light-enhanced LPG sensor-based PANI-PPY (2P) 2-dimensional nano-

sheets has been carried out. The sensing properties were enhanced at room temperature by applying visible light of 30 mW/cm^2 at room temperature. For TENG operation, these nano-sheets were homogeneously distributed in PDMS matrix (3P), which also worked as a self-healing layer.

4.2 Experimental

4.2.1 Synthesis of 2P nanosheets

A very easy and less complicated synthesis process was followed for the preparation of the nanomaterials as shown schematically in Fig. 4.1. The procedure was similar to what followed in Chapter 3 with some modifications. In short, diluted HCl solution was prepared by mixing concentrated HCl in 150 ml DI. While magnetically stirring this solution at a constant speed, APS solution was added until a white precipitate formed. Next, 50 mM CTAB was added to the mixture to act as a capping agent. The monomers of pyrrole and aniline were added to it at a ratio 4:1, and heated at 70 °C. After completion, the final product was collected, washed and dried overnight at 30 °C.

4.2.2 Reaction and formation mechanism of the nanosheets

Fig. 4.2 (a) and (b) show the possible reactions and formation mechanism of the nano-sheets. Primarily, when the aniline monomer was added to the oxidizing, acidic solution, it formed aniline cations. The Cl^- ions from dissolved HCl protonate the monomer cations to make the material conducting. The radical cations then are connected via electrophilic replacements. The para position of the monomer attaches with the oligomers of the clustered amino that are oxidized. The polymerization continues until the scarcity of any of the reactants [18].

A similar process takes place in the case of pyrrole monomers as well, unless the first stage where the pre-occupied anions maintain the electrical neutrality of the material [19]. The polymerization of both the monomers takes place simultaneously within the solution. The sheet-like structure is obtained via a heat treatment at 70 °C. Three steps were followed in the development of the flake-like structure of the polymer: nucleation and growth, effect of surfactant, scission via heat. The surfactant CTAB and

externally applied temperature play the most crucial role in the formation of the 2D morphology of the nanomaterial.

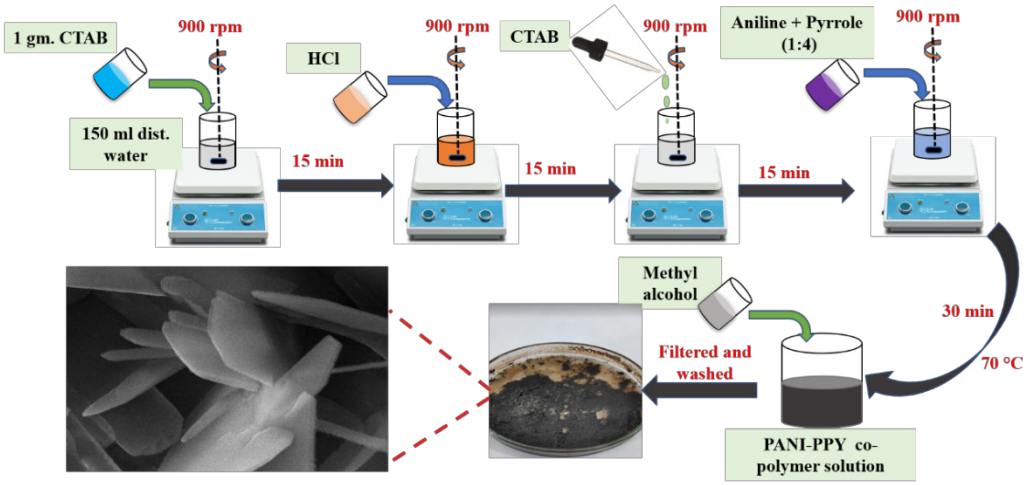

Fig. 4.1 Schematic diagram of synthesis procedure of 2P nanosheets.

The applied temperature in this work is higher than what was used in the previous study. It was observed that this change caused significant improvement in the width and shape of the polymeric sheets. As shown in Fig. 4.2(b), during the early stages of the polymerization, the individual molecules of the PANI-PPY copolymer (2P) get coated with CTAB. This capping agent prevents the agglomeration between the neighboring copolymers by decreasing the surface tension on the boundary of the copolymers. The capping agent prevents further size growth of the polymers. With the creation of more polymers, the newly formed copolymers begin to form chains with the existing copolymers. With an elevation in the reaction temperature, thermal scission occurring at random points of the polymer leads to the formation of short-range polymer instead of long chains. When polymerization takes place amid solitary planes, copolymers tend to manifest sheet-like structures [20].

4.2.3 Assemblage of TENG

For TENG operation, two different layers are needed for the production of contact electrification. For that purpose, a homogeneous dispersion of the 2P nano-sheets in PDMS was covered on single side of a PET substrate inside a spin coating unit.

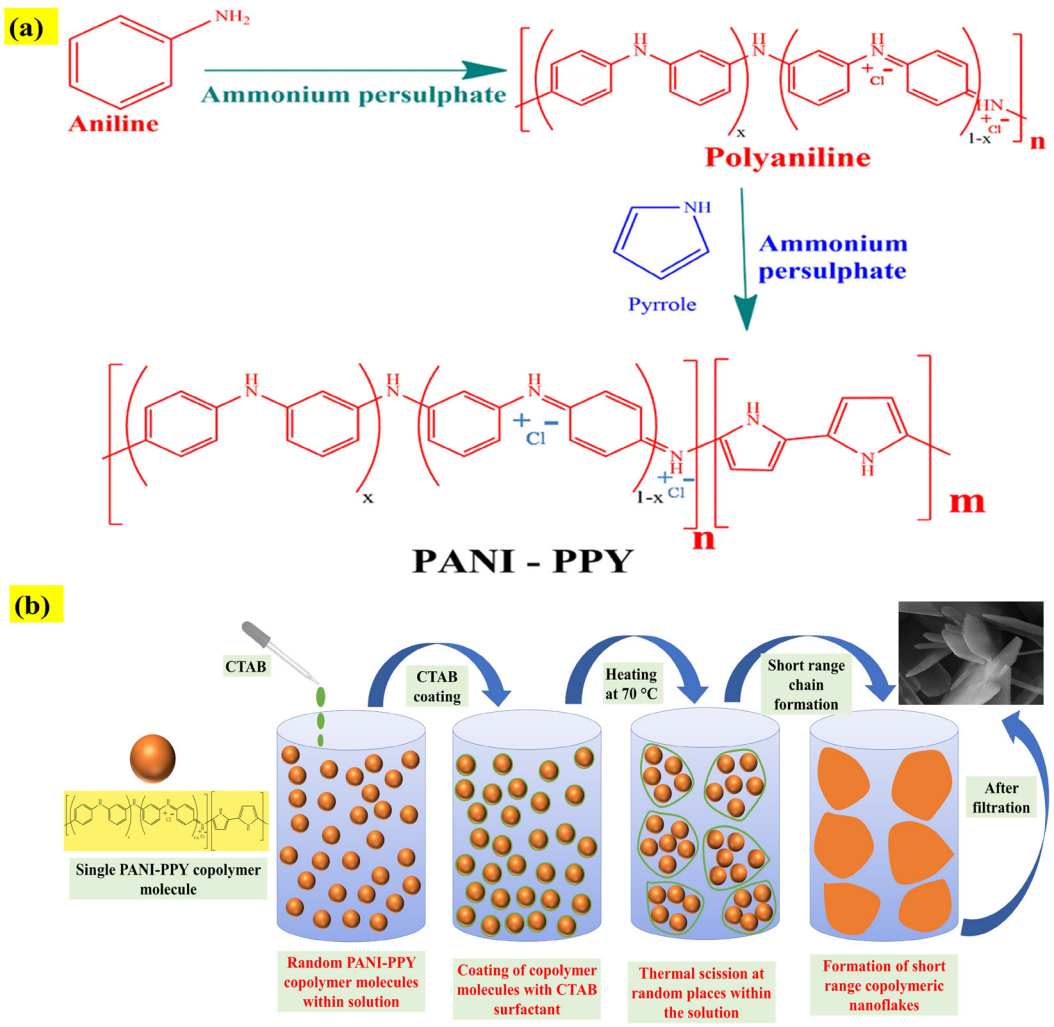

Fig. 4.2 (a) Chemical reaction involved in 2P copolymer synthesis and **(b)** Mechanism of formation of 2D NSs.

The film was kept inside a vacuum compartment to get rid of any air bubbles inside the PDMS matrix, and further dried at room temperature overnight. On the other hand, Kapton adhesive tape was stuck to second PET substrate after rubbing with a sandpaper for making its surface rough. The rough surface makes it more efficient to generate triboelectric charges. Either side of the substrates was then joined using Cu tape, acting as pair of electrodes, and separation of ~ 3 mm was maintained between the active layers with double-sided tape.

4.3 Result and discussion

4.3.1 SEM and TEM analysis

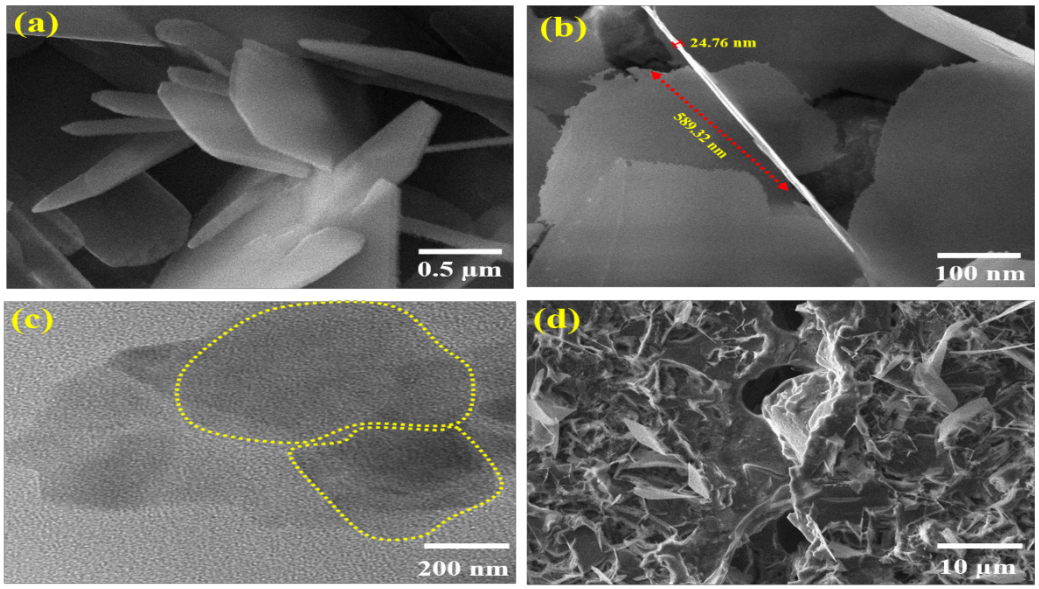

Fig. 4.3 (a) 2P NSs, **(b)** Thickness of NF (~ 24.76 nm), **(c)** TEM images showing nanoflake structure, and **(d)** SEM image of NSs dispersed in PDMS (3P sample).

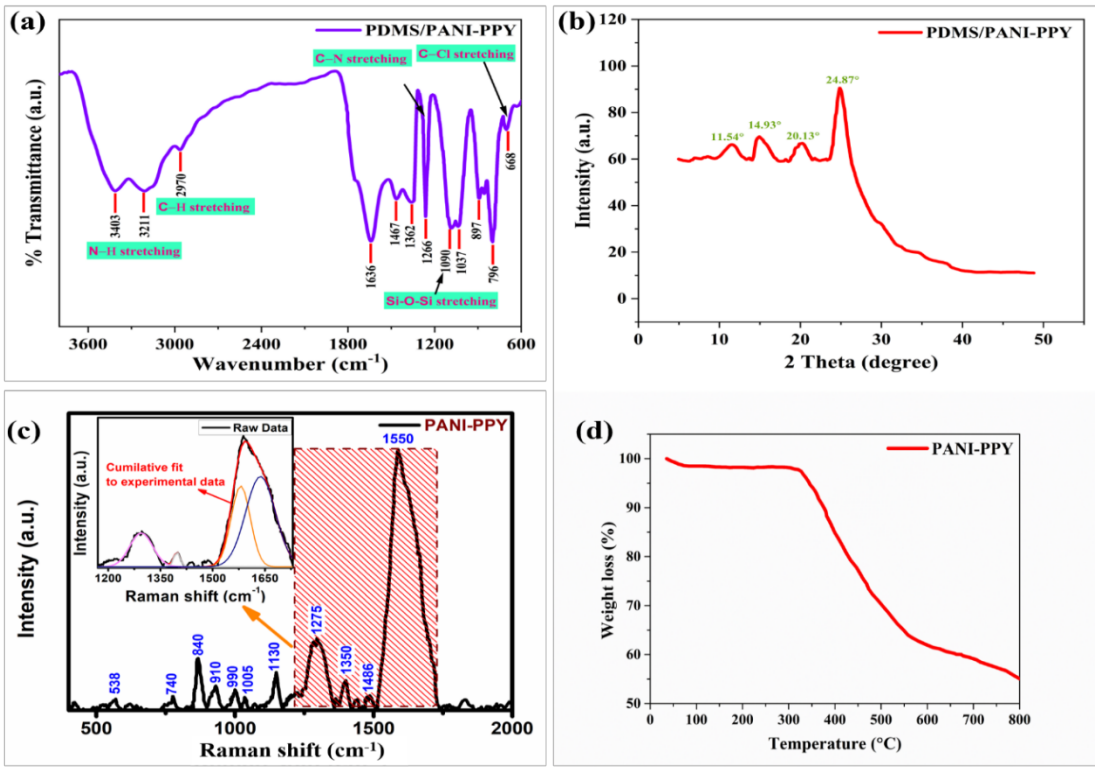

Fig. 4.4 (a) FTIR analysis of PDMS/PANI-PPY, **(b)** XRD of PDMS/PANI-PPY, **(c)** RAMAN peaks of synthesized PANI-PPY, and **(d)** TGA graph of 2P NSs.

The 2-dimensional nanostructured copolymer can be well observed via SEM micrographs in Fig. 4.3 (a) and (b). Multiple nano-flakes can be found all through the sample, which authorizes the effectiveness of the reported synthesis method for the development of sheet-like nanomaterial. From Fig. 4.3 (b), the average thickness of a copolymer flake was measured ~24.76 nm.

HRTEM analysis was performed to authorize 2-dimensional structure of the copolymer. The occurrence of light-colored flakes affirms the polymeric nature of the synthesized material.

4.3.2 FTIR analysis

The chemical analysis of the 2P-PDMS composite was done via FTIR spectroscopy as shown in Fig. 4.4 (a). Two characteristic vibrations corresponding to C═C of quinoid and benzoid rings of PANI were found at 1636 and 1467 cm^{-1} positions. The stretching of the N─H bonds from amine cluster gives rise to an intense absorption at 3403 cm^{-1}. The distinctive vibrations corresponding to the C─H stretching of methyl and methylene groups of PPY were found at 3211 and 2970 cm^{-1} positions. A prominent peak at 3403 cm^{-1} can be seen due to N─H stretching in both PANI and PPY. Other peaks at 1266, 1037, 897 and 796 cm^{-1} were observed owing to C─N vibrations and C─H out-plane distortion, in-plane distortion, and bending vibrations respectively. The successful doping of Cl^- ions in the 2P matrix was confirmed by C─Cl vibration at 668 cm^{-1}. The presence of PDMS was affirmed by the Si─O─Si and Si─C stretching vibrations at 1090 and 897 cm^{-1} [21, 22].

4.3.3 XRD analysis

The semi-crystallographic nature of the copolymer due to the presence of short-range repetitive arrangement was observed in the XRD pattern of the 2P-PDMS composite (Fig. 4.4 (b)). The diffraction peaks at 14.93° and 20.13° confirm the presence of polyaniline in the sample, whereas, the peak at 24.87° can be attributed to both polypyrrole and polyaniline. The existence of PDMS was confirmed by a frail amorphous peak at 11.54°. The co-existence of both crystalline and amorphous peaks

in the sample points towards the manifestation of short-range periodic arrangements of polymeric chains in the sample. The crystallinity can be controlled via the synthesis conditions of the nanomaterial [23, 24].

4.3.4 Raman analysis

The Raman spectrum of the copolymer is visualized in Fig. 4.4 (c). All the characteristic peaks corresponding to the constituent polymers were found in the sample. The presence of doped Cl^- ions in 2P matrix was confirmed by C—Cl vibrations at 740 cm^{-1} and 538 cm^{-1}. Peaks at 1550 and 1350 cm^{-1} are attributed to the stretching in C—C and C—N^+ bonds respectively. The C═N stretching vibration, C—H in-plane twisting, and distortion of quinoid ring are witnessed at 1486, 1130 and 840 cm^{-1}. On the other hand, the benzenoid ring deformation and distortion of PANI can be perceived at 1275 and 910 cm^{-1}. The vibrations from the quinoid polaron and quinoid bi-polaron of PPY occur at 1005 and 990 cm^{-1} [25, 26].

4.3.5 Thermogravimetric analysis

The thermal stability of the copolymer was inspected via TGA analysis. The material was heat treated in N_2 gas environment starting from room temperature. From the TGA curve shown in Fig. 4.4 (d), 1st degradation was observed below 120 °C due to the evaporation of moisture from the sample. Above 250 °C, the long chains start breaking and Cl^- ions start detaching from the polymer. A huge degradation takes place between 310-505 °C owing to the dissociation of dopant Cl^- ions and the elimination of the oligomers from the copolymer. Final degradation occurs above 530 °C due to the complete decomposition of the polymer [70]. By the end, ~ 65% material remains in the sample.

4.3.6 UV-vis spectroscopy

The optical absorption of the material is shown in Fig. 4.5 (a). Maximum absorption was obtained around 367 nm, which falls in the visible range. The inset contains the Tauc plot to reveal the optical band gap of the material ~2.02 eV. As mentioned earlier, the materials possessing an energy gap amid 1.7-3.1 eV are able to utilize photocatalytic behaviour under visible light. Hence, our material is capable to be activated under visible light.

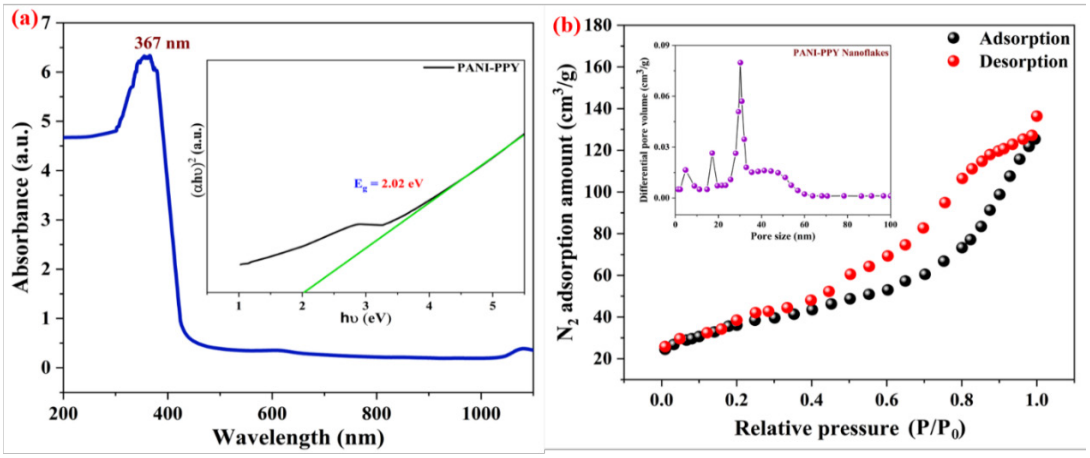

Fig. 4.5 (a) UV-visible spectra of 2P along with Tauc plot in the inset.

(b) Adsorption-desorption isotherm along with pore size distribution in inset.

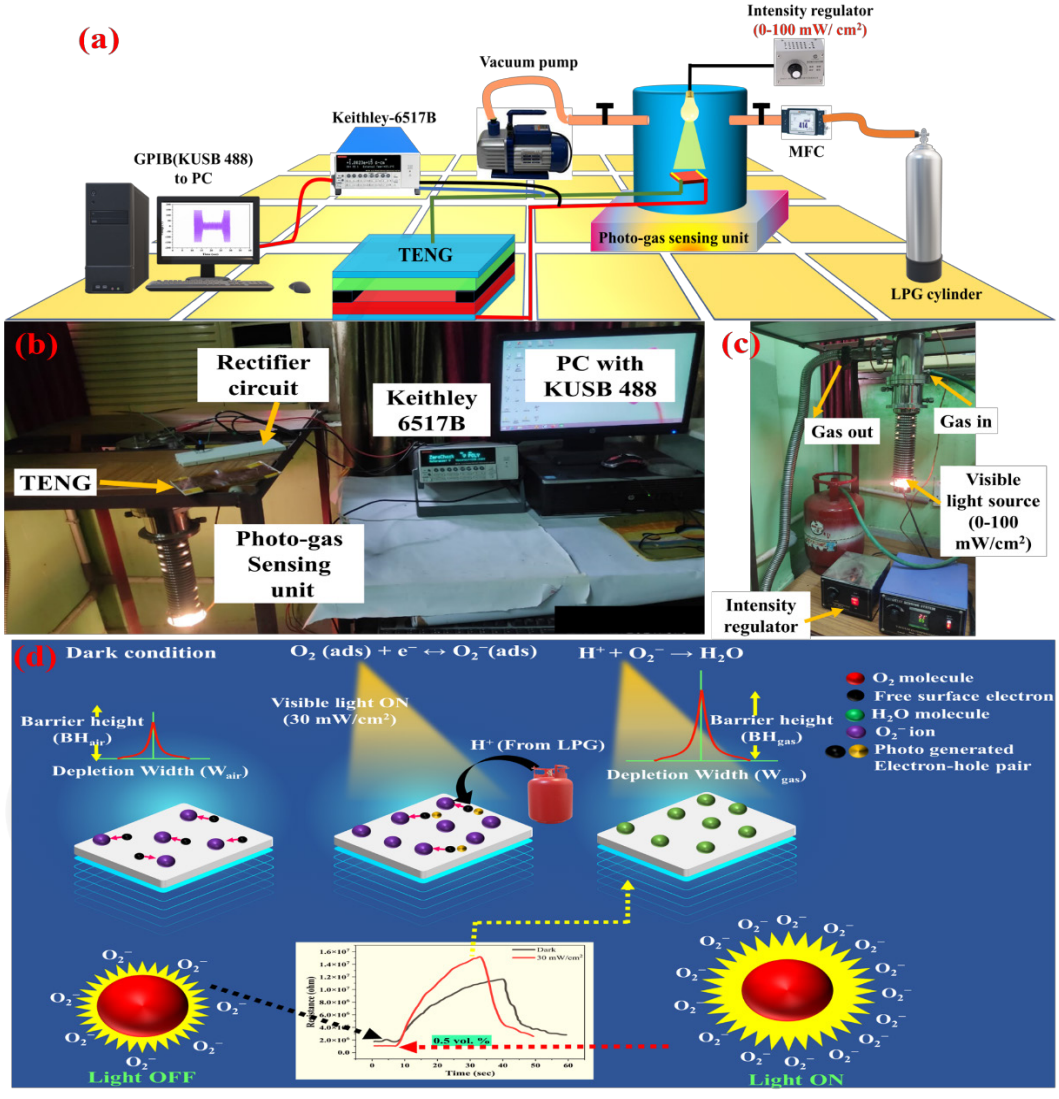

Fig. 4.6 (a) Schematic picture of solar-induced gas detection setup, **(b)** Real-time image of Photoinduced gas sensing setup, **(c)** Lateral view of sensing setup, and **(d)** Mechanism of photo stimulated gas sensing.

4.3.7 BET analysis

To analyze the distribution of pore size and the surface area of the sample, BET analysis was done. For sensing applications, a material should possess a high surface area, and pores lying in the mesoporous region (2-50 nm) [28]. The specimen was 1st pre-treated in nitrogen environment for adsorption studies. The BET analysis was carried out using He carrier gas and N_2 adsorption gas. The distribution of pore size was investigated using BJH model as depicted in Fig. 4.5 (b). The specific surface area, avg. pore size, and mean pore volume were found ~125.6 m^2/g, 30.23 nm, and 0.086 cm^3/g respectively. The mesoporous structure with great surface area reveals its good capability in sensing applications.

4.3.8 Self-powered visible light-induced gas sensing setup and mechanism

All the sensing measurements were executed at RT (30 °C), at humidity ~60 %RH, as measured using HTC-2 Digital Thermo-Humidity Meter. Fig. 4.6 (a) elaborates the graphical representation of the self-powered light-boosted LPG sensing unit. The LPG cylinder, controlled mass flow meter, visible light source, gas chamber, Keithley electrometer (6517-B), PC, and a digital CRO (Owon SDS 1022) are the most important parts of the measurement unit. Real-time photo of the whole measurement unit is shown in Fig. 4.6 (b), (c). The sensing chamber is equipped with a visible light source along with an intensity controller, and an inlet/outlet for inserting/removing gas. A specimen holder is attached inside the chamber to adhere the sensing element. The voltage required to operate the sensing element was supplied via TENG, and recorded through the CRO.

The sensing mechanism depends on the chemical reactions taking place on the material surface and applied gas molecules, and the conduction of charges of the polymer. LPG contains propane and butane molecules that interact with the sensing element.

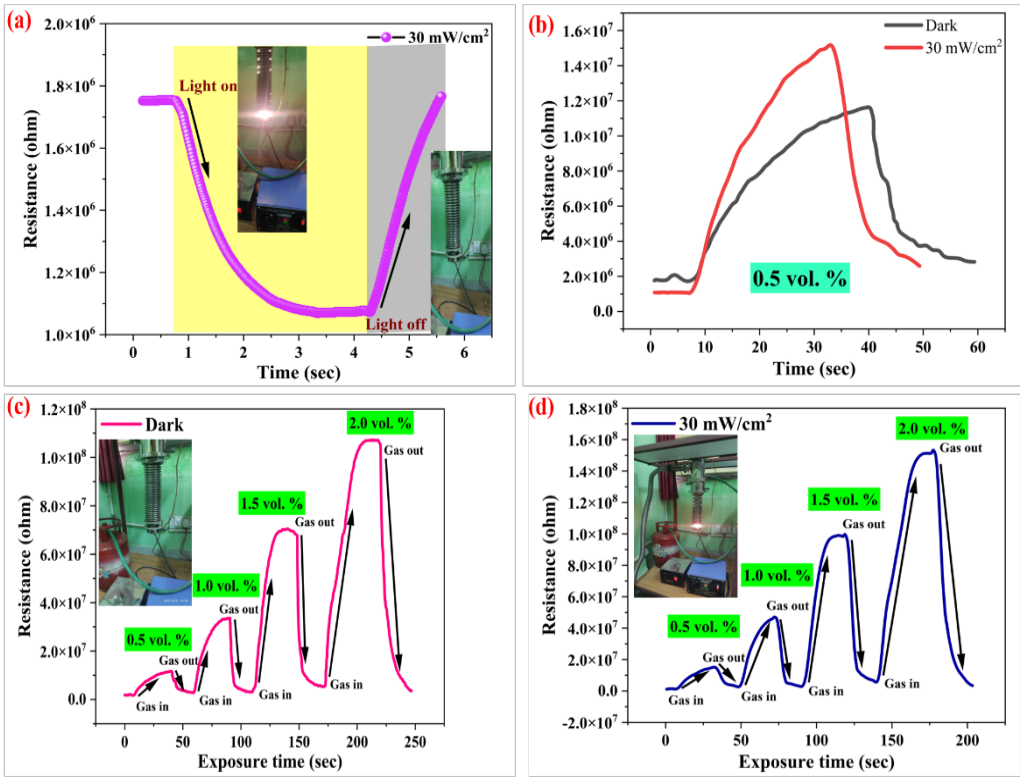

Fig. 4.7 (a) Change of resistance curve under light on and off conditions, **(b)** LPG sensing curve at 0.5 vol. % under dark and illumination conditions, **(c)** LPG sensing at different concentrations under dark conditions, and **(d)** LPG sensing at different concentrations under illumination condition.

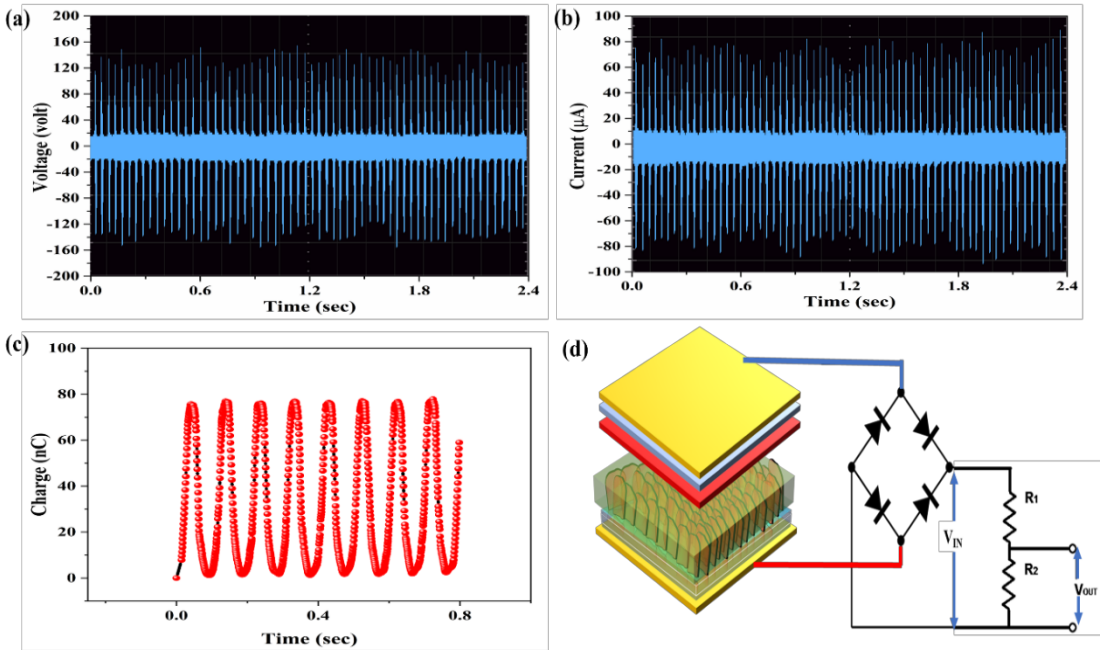

Fig. 4.8 (a) V_{oc}, **(b)** I_{sc}, **(c)** Generated surface charge under continuous tapping by finger, and **(d)** Circuit diagram of voltage divider-based gas sensor powered by TENG.

Conducting polymers generally are equipped with conjugated σ- and π-bonds. The σ-bonds decide the mechanical properties in the material via chain formations through electron sharing. The charge transfer and conduction mechanism arise from the π-bonds. The delocalization of π-bond electrons through the polymer chains causes the electrical conduction of the polymer. The charge transport takes place in two manners: intra chain, where the charge transport takes place along a monodirectional pristine conjugated backbone, and inter chain, where tunnelling and hopping of electrons take place [29].

2P is a p-type material and when it is exposed in air, O_2 molecules get chemisorbed on material surface at room temperature as,

$$\mathbf{O_2(gas) + e^- \leftrightarrow O_2^- (adsorb)} \qquad \mathbf{<200\ °C} \qquad \mathbf{(4.4)}$$

The adsorbed ions create a depletion layer on the material surface, which gives the base resistance R_a of the material.

When the material surface is irradiated with light of particular wavelength, multiple electron-holes sets are created on the surface of material. As a result, the number of carrier of the material upsurges, and the resistance of the material drops significantly (Fig. 4.7(a)). The increased number of surface electrons encourages more adsorption of oxygen molecules on the material surface. As the foreign gas molecules (LPG) react with the adsorbed oxygen, hence with an increased number of O_2^- ions, more reactions will take place with the LPG molecules. The hydrocarbons of LPG react as:

$$\mathbf{C_nH_{2n+2}\ (LPG) + O_2^- \leftrightarrow C_nH_{2n}O + H_2O + e^-} \qquad \mathbf{(4.5)}$$

The newly released electrons then recombine with the majority carrier, holes of the material. As a consequence, the resistance of the material rises, and we get a sensing response of the material.

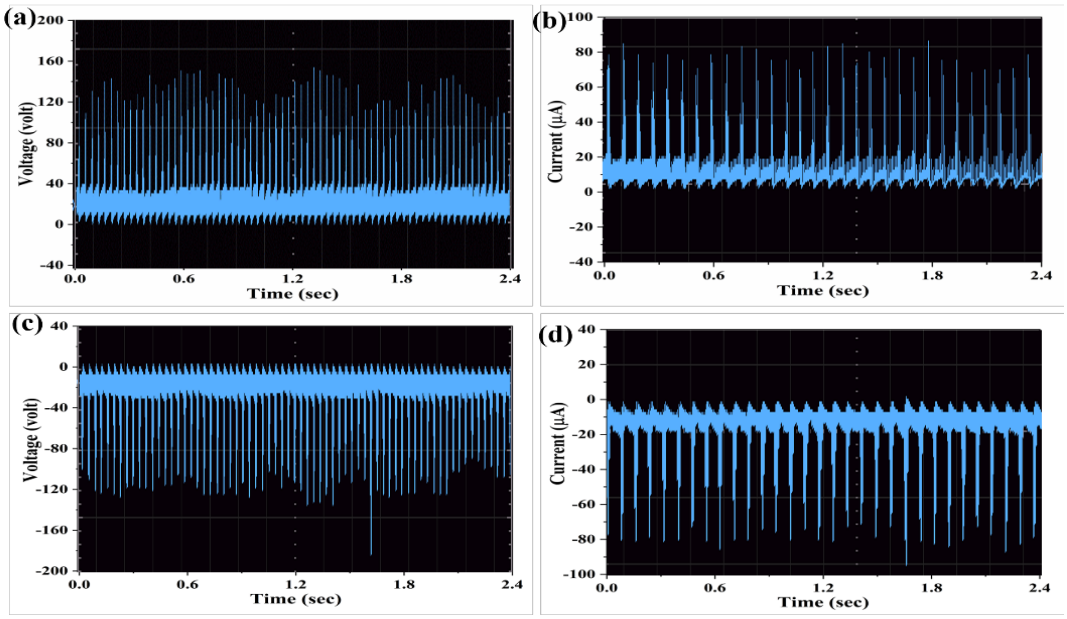

Fig. 4.9 (a) Rectified V_{oc}, **(b)** rectified I_{sc}, **(c)** switched polarity test of (c) generated voltage, and **(d)** generated current.

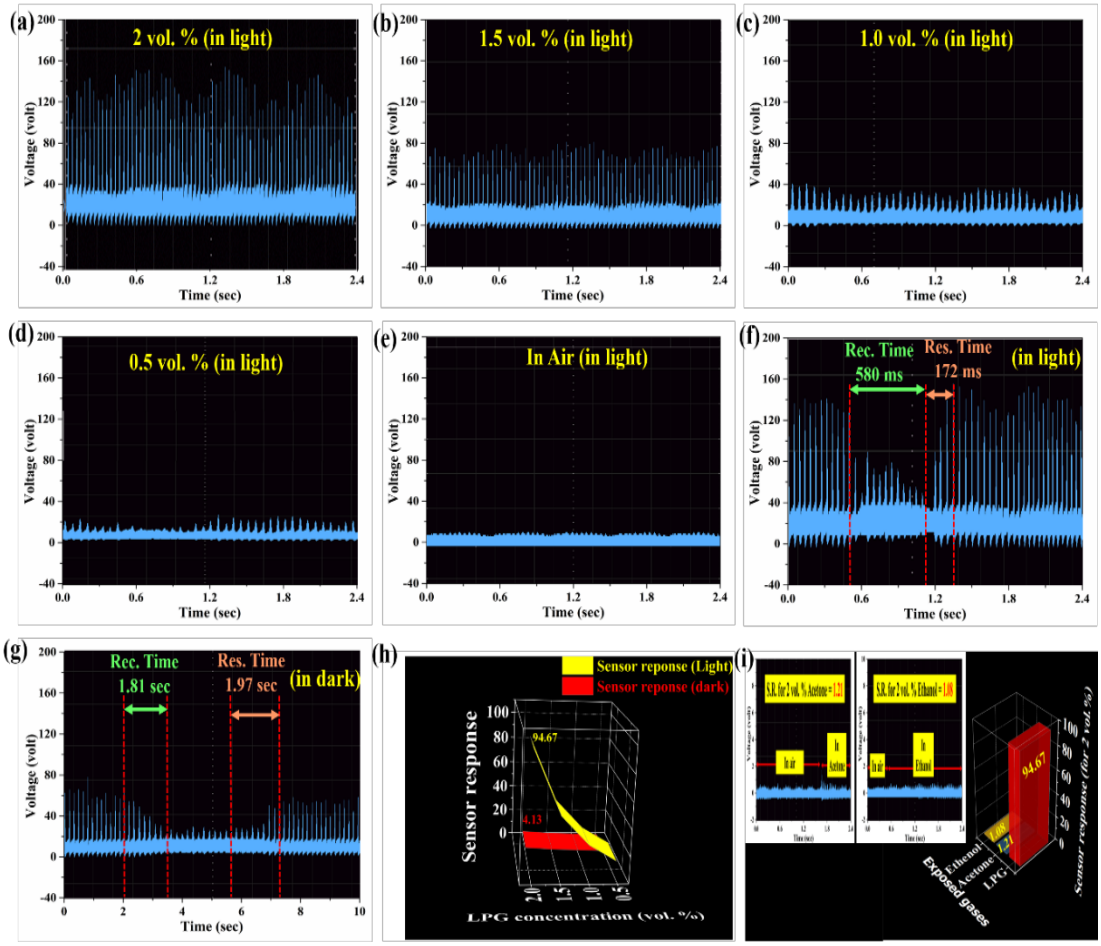

Fig. 4.10. Output voltages under different LPG concentrations **(a)** 2.0 vol.%, **(b)** 1.5 vol.%, **(c)** 1.0 vol.%, **(d)** 0.5 vol.%, **(e)** without LPG in the presence of air; response and recovery time **(f)** under light induced LPG sensing **(g)** under dark condition, **(h)** Sensor response under light on and off conditions; and **(i)** selectivity of fabricated LPG sensor with voltage change in inset.

With increased number of adsorbed oxygen molecules, and charge carriers, the number of interaction with LPG rises in presence of light, thereby, giving an improved sensing performance at room temperature.

The effect of illumination on the LPG sensing performance can be prominently observed in Fig. 4.7 (a), (b) and (c). Different concentrations of LPG (0.5, 1, 1.5, 2 vol.%) was exposed to the sensing element both in dark, and in presence of illumination of 30 mW/cm^2. The base resistance (R_a) in dark and radiance were ~1.83 MΩ and 1.21 MΩ respectively. A sharp decrease in resistance can confirm the creation of enormous charge carriers within the material due to light energy. When exposed to LPG, the highest resistance (R_g) in 2.0 vol.% LPG in dark and radiance were ~107 MΩ and 153 MΩ respectively. This massive change in electrical resistance (~46 MΩ) is the reason of enhanced O_2^- ions adsorption in irradiation. The significance of the huge changes of resistance is very crucial in the gas sensors that are operated by nanogenerators, as discussed in future section. In presence of light, the LPG sensor operated by DC power source displayed minimum response/recovery times ~23/9 sec in 0.5 vol.% LPG exposure.

The real-time pictures of AC open-circuit voltage (V_{oc}) and short circuit current (I_{sc}) of as-prepared TENG measurement are shown in Fig. 4.8 (a) and (b) respectively. Maximum I_{sc} and V_{oc} were ~80 µA and 140 volts respectively. The power density and current density of the TENG (surface area ~30 cm^2) were measured ~390.6 µW/cm^2 and 2.79 µA/cm^2 respectively.

Fig. 4.8 (c) shows the transfer of electrical charges amid the Kapton film and 2P layer, with a maximum ~78 nC. The circuit illustrates the TENG-based sensor operated by the output of the TENG after rectification.

The output voltage and current of the TENG after rectification were found to be ~142 volts and 80 µA (Fig. 4.9 (a), (b)). To confirm whether the figures measured from TENG are pure output or signal noise, the voltage and current were again measured at opposite polarities as shown in Fig. 4. 9 (c), (d). the experiment approved the generation of pure output of the circuit, rather than any noise.

The output voltage of the TENG plays the role of the operating voltage source (V_{IN}) of the LPG sensing element as shown in the circuit diagram (Fig. 4.8 (d)). The formation of the circuit is similar to a voltage divider. As can be seen in Fig. 4.8 (d), the resistance R_2 is the gas sensing element (here 2P film), and R_1 is the internal resistance of the circuit. The output of the circuit is the voltage drop across R_2, i.e.,

$$\mathbf{V_{OUT}} = \{\boldsymbol{R_2}/(\boldsymbol{R_1} + \boldsymbol{R_2})\} \times \mathbf{V_{IN}} \qquad \textbf{(4.6)}$$

It can be clearly seen that V_{OUT} is directly proportional to film resistance R_2. Hence V_{OUT} will increase if film resistance increases. Before it was discussed that the resistance of the p-type sensing element increases in presence of LPG. Hence, the voltage across the film in this circuit also increases when LPG is exposed. The output voltage of the circuit was measured in illumination and in presence of LPG of different concentrations at illuminated conditions (Fig. 4.10 (a-e)). It can be seen that the output voltage across the sensing film for 2.0, 1.5, 1.0 and 0.5 vol.% were ~142, 70.9, 39 and 21 volts respectively, while in the air it was ~1.5 volt. The relative standard deviation (RSD) of the output voltage was ~1.78 %, which is acceptable as the suitable RSD value is below 2 %.

Fig. 4.10 (f) and (g) were utilized for the measurement of response/recovery time of the sensor in case of 2 vol.% LPG, in presence of visible light, and in dark respectively. The response/recovery times in illumination were found to be ~172/580 ms. The voltage decreased from 142 V to 1.5 V when the LPG was removed from the chamber. On the other hand, when 2 vol.% LPG was exposed to the film in dark, it showed response/recovery times ~1.97/1.81 sec, with voltage falling from 67 V to 16.2 V on removal of LPG. A significant improvement can be seen in the LPG sensing behaviour due to illuminating the film. The sensor response was measured from the relation [13],

$$\textbf{Sensor response (SR)} = \frac{V_g}{V_a} \qquad \textbf{(4.7)}$$

Where, V_g = the output voltage of the circuit attained at certain gas concentration, V_a = the output voltage in air. In case of 2.0 vol.% LPG with radiance, the highest sensor response was ~94.67, while the same in dark was only 4.13.

For the measurements taken in Fig. 4.7(b-d), the experiments were operated with an external dc power source that is commonly used in most sensors. In these power supplies, a constant amount of voltage is applied to the sensing element, and the resistance of the film is measured in the presence/absence of gas. But, in self-powered sensors, the voltage generated in a TENG is pulse-type dc voltage in nature that changes every millisecond. Further, in the resistance curves of Fig. 4.7(b-d), the change in the resistance takes place slowly depending on the reactions on the material surface. But in TENG-operated sensors, the voltage is provided for milliseconds multiple times. Hence, numerous electrons are supplied to the film for the reactions within milliseconds. So, in TENG based sensor, the output voltage is the outcome of an instantaneous resistance, and the output voltage/current is in the form of pulses. When external DC power is used, the operating voltage supplied is only 5 volts. But the voltage generated in TENG is high ~142 volt. When this high voltage is applied to the sensing film within milliseconds, a large number of electrons are supplied in the sample, which next does the surface reactions. Due to this reason, the self-powered sensors give very high sensitivity in a very small time.

The slope of the calibration curve gives the sensitivity of a sensor. As can be seen in Fig. 4.10 (h), the sensitivity of the material is ~52.67 SR/vol.% in illumination and ~1.83 SR/vol.% in dark. Selectivity decides the ability to sense a particular gas more than any other gas. For that, the sensing experiments were carried out in presence of ethanol and acetone. The copolymer turned out to be highly selective towards LPG as can be seen in Fig. 4.10 (i).

The stability of the device was tested after a gap of 2 months from the day of film fabrication. For a good sensing device, the outputs should be consistent with the outputs received from the fresh sample. After the time gap, the device produced an output voltage of 141 volts in response to 2.0 vol.% LPG under visible light (sensor

response = 94.00). After two weeks, the experiments were repeated, which gave an output of 142.8 volts under similar conditions (sensor response = 94.93). The obtained results show the high stability of the device over long-term use.

The high porosity of the 2P nano-flakes is the reason behind the high and fast sensing response of the material. The nanomaterials are well blessed with a high surface-to-volume ratio. 2-dimensional nanomaterials possess outstanding charge-transport properties owing to the possession of fewer grain boundaries compared to other types of nanomaterials (1-dimensional, 3-dimensional). Less number of grain boundaries makes the flow of electrons uniform between the electrodes [30]. The low electron diffusion maintains uniform output throughout the experiment. The application of visible light makes the sensing performance even better due to the production of enormous charge carriers on the sample.

4.3.9 Self-healing capability

The self-healing ability of the 3P material was observed at room temperature as shown in Fig. 4.11 with real-time images. At 1st, a layer of 3P was smeared inside a silicon mould, and dried overnight at room temperature. The resultant shiny, smooth, black layer was used to conduct the healing experiments afterwards. With the help of a sterilized, sharp razor, a clean cut was introduced into the specimen. Real-time images were taken after every 5 min, and the sample was found to be completely healed within only 35 min. The introduction of 2P inside the PDMS matrix brings covalent bonds in 3P composite that is reversible in nature. The FTIR and Raman analysis of the composite revealed the presence of C─H and N─H bonds in the sample. These bonds are regenerated within the sample after any deformation. Hence, after a cut was introduced, the material regained its previous uncracked structure by the restoration of reversible hydrogen bonding and π-bonding in the composite. The healing was achieved at room temperature without any external agent within 35 min.

The output voltages of the nanogenerator pre- and post-healing were measured to analyze the restoration of the material. The output voltage of the nanogenerators before any damage was ~142 volts, while, the healed nanogenerators gave an output ~141 volts.

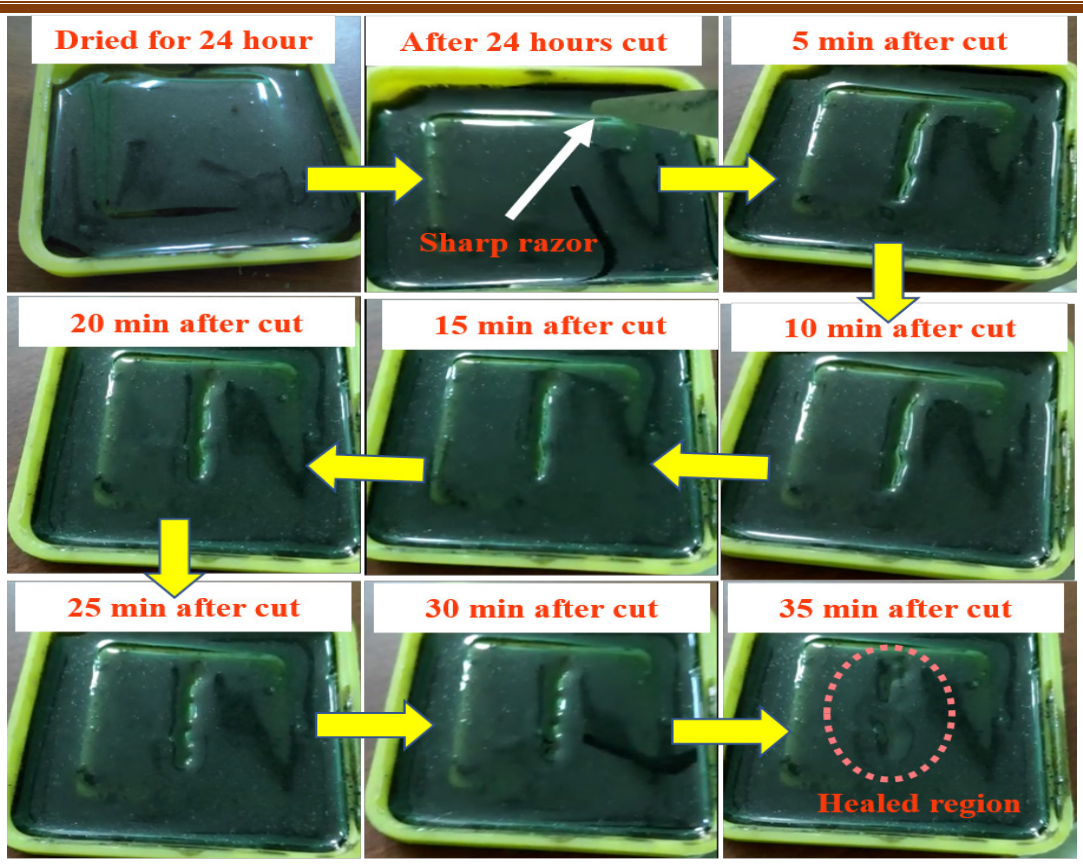

Fig. 4.11 Real-time images of 3P composite, consecutively taken after 5 min gap showing healing nature.

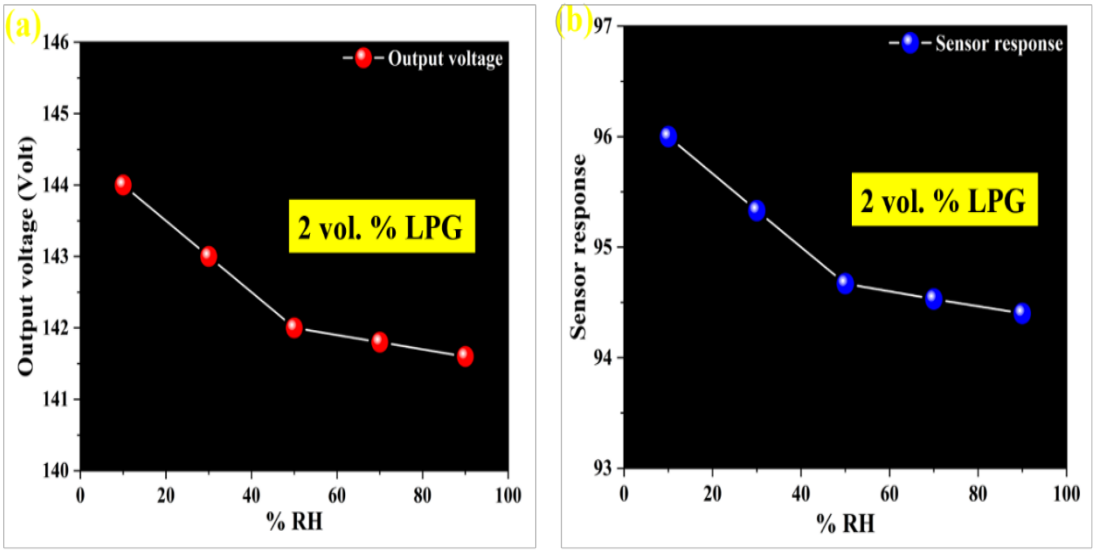

Fig. 4.12 (a) Variations in Output voltage with the increasing %RH for 2 vol.% LPG. **(b)** Variations in sensor response with the increasing %RH for 2 vol.% LPG.

Hence, the healing efficiency of the output voltage was 99.7%, which affirms the fast and effective healing of the composite system.

4.3.10 Effect of humidity on LPG sensing

For a gas sensor fabrication, it is highly desirable to test the effect of different humidity levels on the gas sensing performance of that sensing element. For an efficient gas sensor, the effect of humidity should be the least. Fig. 4.12 (a), (b) shows the changes in output voltage and sensor response, when the material was exposed to 2 vol.% LPG in presence of different humidity levels. There were no extreme changes that occurred in LPG sensing performance which proves that the overall sensing performance does not get affected much in presence of humidity.

4.4 Conclusion

In this work, waste energy has been utilized for driving a sensor. 2-dimensional nano-sheets of PANI-PPY copolymer (2P) were prepared using an easy and inexpensive method. The copolymer was thoroughly investigated using different characterization techniques. The material showed brilliant LPG detection below its LEL when illuminated with visible light at room temperature. The sensor was operated with TENG (3P) that generated an output voltage and current of ~142 volt and 80 µA respectively. Using the output of TENG as a power source, the sensing element showed a maximum sensor response ~94.67 and sensitivity ~52.67 SR/vol.% under the influence of 30 mW/cm^2 visible light. The material was able to detect very low concentrations of LPG almost instantaneously with response/recovery times 172/580 ms. Self-healing ability was also successfully introduced in the TENG layer to regain its properties after any damage.

References

[1] Z.L. Wang, J. Song, Piezoelectric Nanogenerators Based on Zinc Oxide Nanowire Arrays, Science. 312 (2006) 242–246.

[2] F.R. Fan, Z.Q. Tian, Z. Lin Wang, Flexible triboelectric generator, Nano Energy. 1 (2012) 328–334.

[3] A. Bhaduri, S. Singh, R.K. Tripathi, U. Kumar, K.B. Thapa, B.C. Yadav, Healable, highly sensitive LPG sensor based on $Ni_{0.4}Zn_{0.6}Fe_2O_4$ nanohybrid grown by autocombustion process, Sensors and Actuators B: Chemical. 327 (2021) 128840.

[4] A. Singh, S. Sikarwar, B.C. Yadav, Design and fabrication of quick responsive and highly sensitive LPG sensor using ZnO/SnO_2 heterostructured film, Materials Research Express. 8 (2021) 45013.

[5] R.K. Sonker, M. Singh, U. Kumar, B.C. Yadav, MWCNT doped ZnO nanocomposite thin film as LPG sensing, J. Inorg. Organomet. Polym. Mater. 26 (2016) 1434–1440.

[6] M. Singh, B.C. Yadav, A. Ranjan, M. Kaur, S.K. Gupta, Synthesis and characterization of perovskite barium titanate thin film and its application as LPG sensor, Sensors and Actuators b: Chemical. 241 (2017) 1170–1178.

[7] M.D. Gonugade, S.B. Powar, B.S. Salokhe, C.D. Lokhande, J.H. Kim, K. V Gurav, SILAR deposited nanocrystalline ZnO films as LPG sensor, Materials Today: Proceedings. 43 (2021) 2668–2672.

[8] A.R. Choudhary, S.A. Waghuley, LPG sensing application of PPy based nanocomposites at low operable temperature, Materials Letters. 205 (2017) 36–39.

[9] P.T. Patil, P.S. More, S.B. Kondawar, LPG Sensing Properties of Electrospun In-Situ Polymerized Polyaniline/MWCNT Composite Nanofibers, NAC 2019, Springer. 242 (2020) 3–18.

[10] S. Kaur, J. Singh, R. Rawat, S. Kumar, H. Kaur, K.V. Rao, M. Rawat, A smart LPG sensor based on chemo-bio synthesized MgO nanostructure, Journal of Materials Science: Materials in Electronics. 29 (2018) 11679–11687.

[11] J. Wang, H. Shen, Y. Xia, S. Komarneni, Light-activated room-temperature gas sensors based on metal oxide nanostructures: A review on recent advances, Ceramics International. 47 (2021) 7353-7368.

[12] Q. Zhang, Z. Pang, W. Hu, J. Li, Y. Liu, Y. Liu, F. Yu, C. Zhang, M. Xu, Performance degradation mechanism of the light-activated room temperature NO2 gas sensor based on Ag-ZnO nanoparticles, Applied Surface Science. 541 (2021) 148418.

[13] S. Singh, R.K. Tripathi, M.K. Gupta, G.I. Dzhardimalieva, I.E. Uflyand, B. Yadav, 2-D self-healable polyaniline-polypyrrole nanoflakes based triboelectric nanogenerator for self-powered solar light photodetector with DFT study, Journal of Colloid and Interface Science. 600 (2021) 572–585.

[14] Y. Long, Y. Chen, Y. Liu, G. Chen, W. Guo, X. Kang, X. Pu, W. Hu, Z.L. Wang, A flexible triboelectric nanogenerator based on a super-stretchable and self-healable hydrogel as the electrode, Nanoscale. 12 (2020) 12753–12759.

[15] X. Han, D. Jiang, X. Qu, Y. Bai, Y. Cao, R. Luo, Z. Li, A Stretchable, Self-Healable Triboelectric Nanogenerator as Electronic Skin for Energy Harvesting and Tactile Sensing, Materials. 14 (2021) 1689.

[16] D. Yang, Y. Ni, H. Su, Y. Shi, Q. Liu, X. Chen, D. He, Hybrid energy system based on solar cell and self-healing/self-cleaning triboelectric nanogenerator, Nano Energy. 79 (2021) 105394.

[17] F.-R. Fan, L. Lin, G. Zhu, W. Wu, R. Zhang, Z.L. Wang, Transparent triboelectric nanogenerators and self-powered pressure sensors based on micropatterned plastic films, Nano Letters. 12 (2012) 3109–3114.

[18] S.J. Tang, A.T. Wang, S.Y. Lin, K.Y. Huang, C.C. Yang, J.M. Yeh, K.C. Chiu, Polymerization of aniline under various concentrations of APS and HCl, Polymer Journal. 43 (2011) 667–675.

[19] N. V. Blinova, J. Stejskal, M. Trchová, J. Prokeš, M. Omastová, Polyaniline and polypyrrole: A comparative study of the preparation, European Polymer Journal. 43 (2007) 2331–2341.

[20] S. Kuroda, K. Terauchi, K. Nogami, I. Mita, Degradation of aromatic polymers-I. Rates of crosslinking and chain scission during thermal degradation of several soluble aromatic polymers, European Polymer Journal. 25 (1989) 1–7.

[21] M.A. Chougule, S.G. Pawar, P.R. Godse, R.N. Mulik, S. Sen, V.B. Patil, Synthesis and Characterization of Polypyrrole (PPy) Thin Films, Soft Nanoscience Letters. 01 (2011) 6–10.

[22] L.M. Johnson, L. Gao, C.W. Shields IV, M. Smith, K. Efimenko, K. Cushing, J. Genzer, G.P. López, Elastomeric microparticles for acoustic mediated bioseparations, Journal of Nanobiotechnology. 11 (2013) 1–8.

[23] P. Ferreira, Á. Carvalho, T.R. Correia, B.P. Antunes, I.J. Correia, P. Alves, Functionalization of polydimethylsiloxane membranes to be used in the production of voice prostheses, Science and Technology of Advanced Materials. 14 (2013) 055006.

[24] S. Bhadra, D. Khastgir, Determination of crystal structure of polyaniline and substituted polyanilines through powder X-ray diffraction analysis, Polymer Testing. 27 (2008) 851–857.

[25] G.M. Do Nascimento, Spectroscopy of Polyaniline Nanofibers, Nanofibers. (2010) 349.

[26] Y.C. Liu, B.J. Hwang, Identification of oxidized polypyrrole on Raman spectrum, Synthetic Metals. 113 (2000) 203–207.

[27] Y. Zhang, J. Liu, Y. Zhang, J. Liu, Y. Duan, Facile synthesis of hierarchical nanocomposites of aligned polyaniline nanorods on reduced graphene oxide nanosheets for microwave absorbing materials, RSC Advances. 7 (2017) 54031–54038.

[28] Z. Wei, Q. Zhou, Z. Lu, L. Xu, Y. Gui, C. Tang, Morphology controllable synthesis of hierarchical WO_3 nanostructures and C_2H_2 sensing properties, Physica E: Low-Dimensional Systems and Nanostructures. 109 (2019) 253–260.

[29] Y.C. Wong, B.C. Ang, A.S.M.A Haseeb, A.A. Baharuddin, Y.H. Wong, Conducting Polymers as Chemiresistive Gas Sensing Materials: A Review, Journal of The Electrochemical Society. 167 (2020) 037503.

[30] H. Hashtroudi, I.D.R. MacKinnon, M. Shafiei, Emerging 2D hybrid nanomaterials: Towards enhanced sensitive and selective conductometric gas sensors at room temperature, Journal of Materials Chemistry C. 8 (2020) 13108–13126.

Chapter 5

Waste material based self-healable and self-powered Fluoride ion detection device: An unexplored and highly responsive detection method

This work discusses the results of a new method for the detection of fluoride ions in water below permissible limits using a waste material-based self-healable triboelectric nanogenerator. The steps involved during the process is explained in detail. The device is fabricated using waste materials like polythene bags, BSR rubber, and used plastic sheets that confirms the waste-to-energy conversion capability with a voltage ~242 volts and current ~40 μA. The self-powered detector shows maximum sensor response of 12.10 and % sensor response of 1110 %. This device also has self-healing ability showing rapid healing under ~25 min with a healing efficiency of 99.9%. The calculated LOD value in present work is 4.7 μM, which is better than previous works.

5.1 Introduction

In this era, with the progress in technology and economy, the concerns related to a shortage of energy, solid and electronic waste, drinkable water, and other ecological and health distresses are also growing speedily. Earth won't be habitable without energy and water. The fluoride ions in stones and soil are one of the natural sources of the contamination of water. According to WHO, 1.5 gm/ltr is the maximum permissible limit of fluoride concentration in water [1]. Above that, it can cause joint stiffness, calcification of ligaments, sporadic pain, osteosclerosis, and damage in soft tissues, lungs, liver, kidneys etc. [2]. These issues are the reason for the early detection of fluoride effectively. At present, many methods like photoluminescence, colorimetric, absorption, and fluorescent are used for detecting these ions [3]. Yet, these methods have a serious problem of required resources, equipment and detection time. Heavy and big instruments are needed in fluoride detection that needs a huge power supply, while a major portion of the world has electricity insufficiency. Hence, a detecting system that does not need an external power supply is highly needed to detect these ions well. Another big problem is that almost 7.3 kg/capita of electronic waste was produced worldwide in 2019. The report says in the next 30 years the total e-waste will exceed 3.4 billion tons from what it was in 2016 (2.01 billion tons) [4]. Butadiene-styrene rubber (BSR) is present in tyre tube rubber, and plastics are one of the main parts of solid waste. These products are not bio-degradable and are very hazardous [5]. When the non-renewable energy sources will be exhausted, renewable energy resources and green energy equipment will be the only solutions for tackling the energy crisis. Both energy and waste materials crises have given the chance to decipher these issues for the research community.

Recently, waste management has arisen as a widespread area of research to recycle these materials in environment-friendly and sustainable development. Since 2012, triboelectric nanogenerator (TENG) has become a new member in the progress of new techniques for green energy generation, where electricity is generated by coupling of electrostatic induction and contact electrification [6]. In TENG, waste materials can be used as a contact layer to provide the required power to operate

electronic devices. Previously, materials like wasted tea leaves, milk cartons, waste papers, sunflower husk, etc. have been used in preparing the TENG layers to reuse garbage in generating electricity [7-10].

Moreover, in the unceasing progress of different sensors, the dimension of the device, material selection, and power supply plays a very vital part in the price of that device. Existing sensors working on optical, chemisorption, electrochemical, etc. are big-sized, operate at high temperatures, depending on the external power source, have large response/recovery times, exhibit low response, and their production cost is high. With the discovery of TENG, different sensors such as humidity sensors, photosensors, pressure sensors, biosensors, temperature sensors, gas sensors etc. are using nanogenerators for power sources [11-21]. These sensors need a high temperature and power source to operate. One major reason for the need of high temperatures is involving costly but less sensitive materials. Different types of materials (conducting polymers, metal oxides, metallopolymers etc.) have been used to solve this problem. The mechanical distortion in nanogenerators is a big issue occurring from repetitive stress and strain. This problem can be overcome by using healable materials during device fabrication.

Here, a new technique is used and validated to detect fluoride ions, using a TENG-based device fabricated using hazardous waste (BSR). BSR decorated with Lanthanum doped Polyaniline-Polypyrrole (LaPP) nanospheres (BSR-La) mixed in PDMS (PDMS/BSR-La) was used to form one layer of the TENG that is self-healable in nature. The BSR-La gives an increased contact area amid the tribo layers owing to the high surface-to-volume ratio. The same BSR-La was also deposited on scotch tape to use as the sensing element. The detection was very fast and self-powered. This device can detect fluoride ions very efficiently.

5.2 Experimental

5.2.1 LaPP nanosphere synthesis

The synthesis process followed in this work is the same as mentioned in Chapter 3, except for the addition of Lanthanum nitrate for doping of La in the matrix.

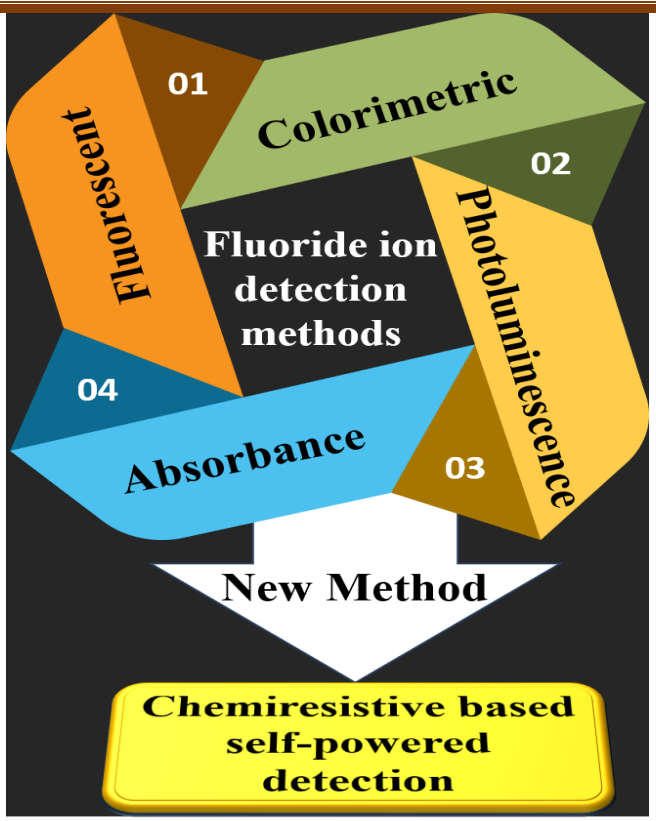

Fig.5.1 Available fluoride detection processes.

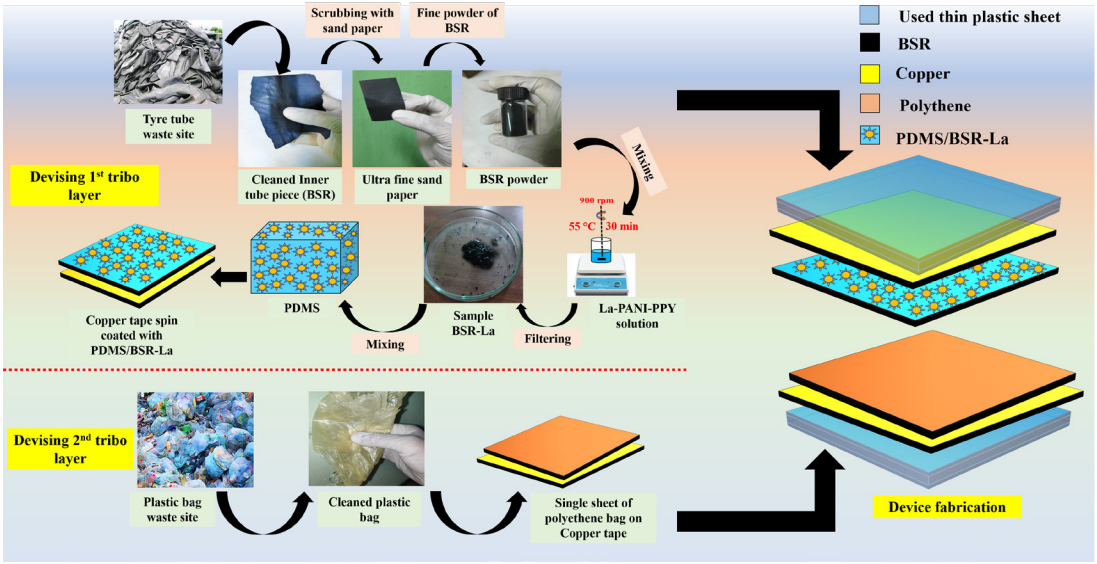

Fig. 5.2 Fabrication of both tribo layers in the present study.

Other steps followed in the entire synthesis process contain no changes. Here, after adding the monomers of aniline and pyrrole, lanthanum nitrate was added immediately and stirred at 900 rpm for ½ hr. After that, 65 °C temperature was applied and kept stirring for 6 hr at 1000 rpm. The final black product was collected, washed thoroughly, and finally dispersed in DI water to coat it on BSR.

5.2.2 Tribo layer fabrication

TENG needs two dissimilar layers for operation. 1st layer was prepared with powdered BSR coated with LaPP (BSR-La) in the PDMS matrix. The BSR was collected from waste space, cleaned thoroughly, and scrubbed with sandpaper to get BSR small particles. The BSR powder was dispersed in an aqueous solution of LaPP, while stirring at 900 rpm for ½ hr at 55 °C, to properly combine both the phases. The final product (BSR-La) was filtered and dried at room temperature. The BSR-La was dispersed evenly in PDMS, and coated on scotch tape using a spin coater. The tape was then stuck to Cu tape (electrode). The 2nd layer was prepared with a waste polyethylene bag collected from waste space, which was cleaned, and attached to another Cu tape. Both the layers were attached to each other using a double-sided tape, leaving space between them as shown in Fig. 5.2.

5.3 Result and discussion

5.3.1 Electron microscopic analysis with elemental mapping

The SEM micrographs of BSR-La are shown in Fig. 5.3(a), where large BSR particles with LaPP may be seen. Fig. 5.3(b) is an SEM micrograph of the marked section of Fig. 5.3(a) at a higher resolution, where both phases can be seen more precisely. The boundaries of the phases can be seen well connected with each other. Fig. 5.3(c) shows the LaPP nanomaterial with a perfect spherical shape within a size 14-50 nm. The elements present in the LaPP were confirmed by both EDX and elemental mapping shown in Fig. 5.3(d) and (e). From the images, the presence of chlorine and lanthanum was proved as well.

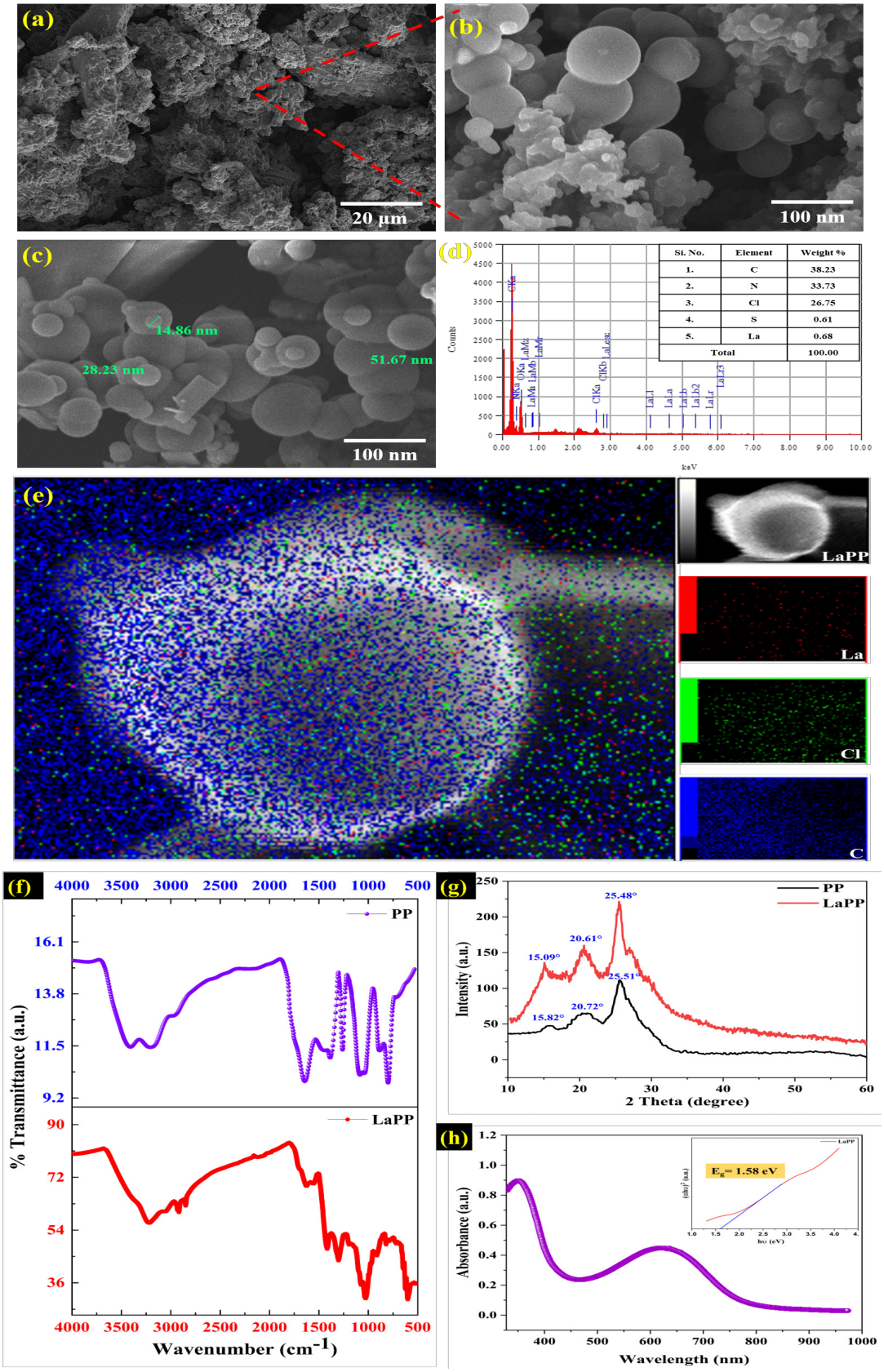
(a)
20 µm
(b)
100 nm
(c)
14.86 nm
28.23 nm
51.67 nm
100 nm
(d)
Si. No. | Element | Weight %
1. | C | 38.23
2. | N | 33.73
3. | Cl | 26.75
4. | S | 0.61
5. | La | 0.68
Total | 100.00
Counts
keV
(e)
LaPP
La
Cl
C
(f)
PP
LaPP
% Transmittance (a.u.)
Wavenumber (cm-1)
(g)
PP
LaPP
25.48°
20.61°
15.09°
25.51°
20.72°
15.82°
Intensity (a.u.)
2 Theta (degree)
(h)
Eg= 1.58 eV
Absorbance (a.u.)
Wavelength (nm)

Fig. 5.3 SEM image of **(a)** BSR-La, **(b)** magnified image of BSR-La, **(c)** LaPP nanospheres, **(d)** EDX analysis of LaPP, **(e)** Elemental mapping of LaPP, **(f)** FTIR of PP and LaPP, **(g)** XRD of PP and LaPP, and **(h)** UV-Visible spectroscopy with Tauc plot in the inset.

5.3.2 Fourier Transform Infrared spectroscopic analysis

In the FTIR spectra of LaPP and PP samples, all the characteristic absorptions were present (Fig. 5.3 (f)) as shown in Table 5.1. In the LaPP sample, an additional band related to doped La was present at 601 cm^{-1}. The bands were slightly red-shifted in LaPP, owing to doping.

Table 5.1. FTIR peak positions in both PP and LaPP.

S.No.	Peak position in PP (cm^{-1})	Peak position in LaPP (cm^{-1})	Assignment
1.	3410	3217	N—H stretching
2.	3203	3052	N—H stretching
3.	2973	2917	C—H stretching
4.	1643	1629	C=C stretching
5.	1460	1423	C=C stretching
6.	1262	1302	C—N stretching
7.	1084	1026	C—H out of plane stretching
8.	889	820	C—H in-plane stretching
9.	798	718	C—H bending
10.	703	647	C—Cl stretching

No other extra bands were present, proving there was no impurity. The presence of C—H stretching in LaPP confirms that the benzene ring of PP sample was not destroyed in the process of doping [22]. The ratio of area under the curves of benzenoid and quinoid rings is proportional to the conjugation length present in the polymer, which is again directly proportional to the electrical conductivity of the nanomaterial

[23]. Here, the ratio is bigger in LaPP than in PP, which means LaPP is more conductive than PP.

5.3.3 XRD investigation

The XRD curves of both LaPP and PP show semi-crystallographic nature of the samples (Fig. 5.3(g)). The peaks at 20.72° and 15.82° are the characteristics of PANI, while the peak at 25.51° is the characteristic of both PANI and PPY. The LaPP diffractions are a bit noisier than PP owing to the doping of La. The increase of crystallinity in LaPP can be observed by broader and sharper peaks compared to those in PP. There is an obvious change in the intensity in the La-doped sample as the density of electrons changes due to La doping. The shifting of peaks can also be observed as the size change in LaPP.

5.3.4 UV-visible analysis

In the optical spectrum of PANI, two major peaks, one due to π—π^* transitions at benzenoid rings at 340 nm, and the other due to excitonic charge relocation in the quinoid arrangement at 600 nm observed [24]. The combination of PANI with PPY, and La doping cause a shift in these absorptions towards higher wavelengths. As a result, in the LaPP sample, the peaks arise at 352.93 nm and 621.86 nm. The optical band gap measured from the Tauc plot was ~1.58 eV. Generally, PP samples possess a bandgap of 1.8-2.2 eV [25]. Here, the band gap can be seen to be red-shifted as the conductivity in the material increases with doping.

5.3.5 TENG output performance and Battery-less fluoride ion detection

The PDMS/BSR-La coated tribo layer is presented in Fig. 5.4 (a), while the fluoride water dripping on the tribo layer, and evaporation of water from the film are shown in Fig. 5.4 (b) and (c). The whole setup of TENG based fluoride detector is shown in Fig. 5.4(d), which operates on the mode of contact separation, and generates an output voltage of ~242 volts when tapped by a finger. The open-circuit output voltage and short circuit current of TENG with finger tapping are displayed in Fig. 5.4 (e) and (f) which are ~242 volts and ~40 μA respectively (area ~24 cm^2). The DC outputs were also produced with a full wave rectifier circuit (Fig. 5.4 (g), (h)), which was detected in a digital oscilloscope for fluoride ion detection.

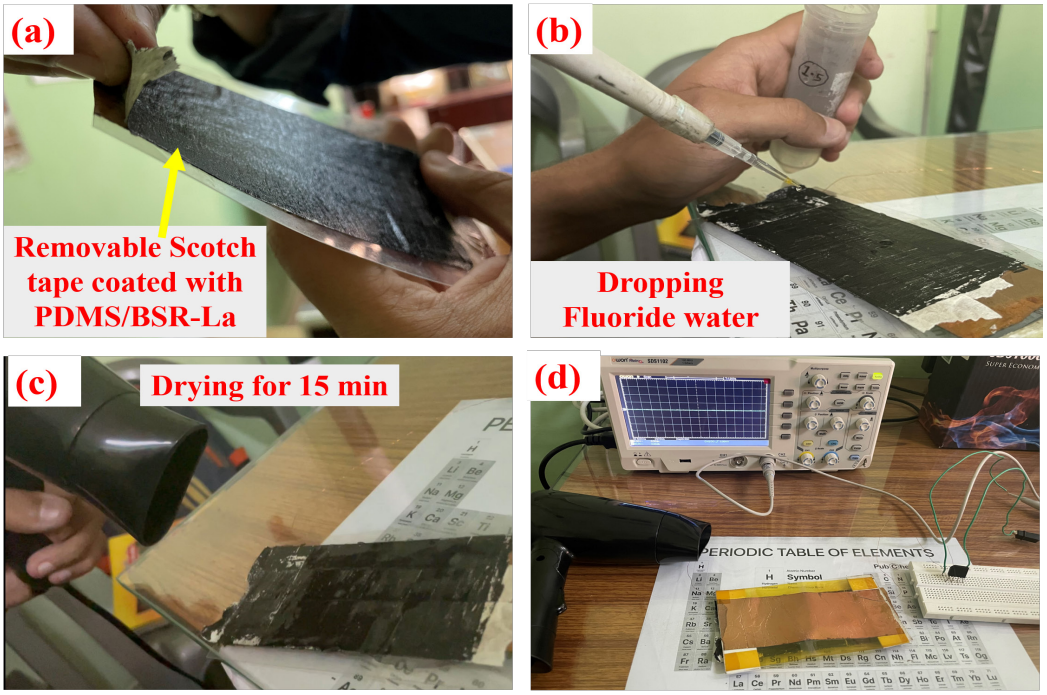
(a)
Removable Scotch tape coated with PDMS/BSR-La
(b)
Dropping Fluoride water
(c)
Drying for 15 min
(d)
PERIODIC TABLE OF ELEMENTS

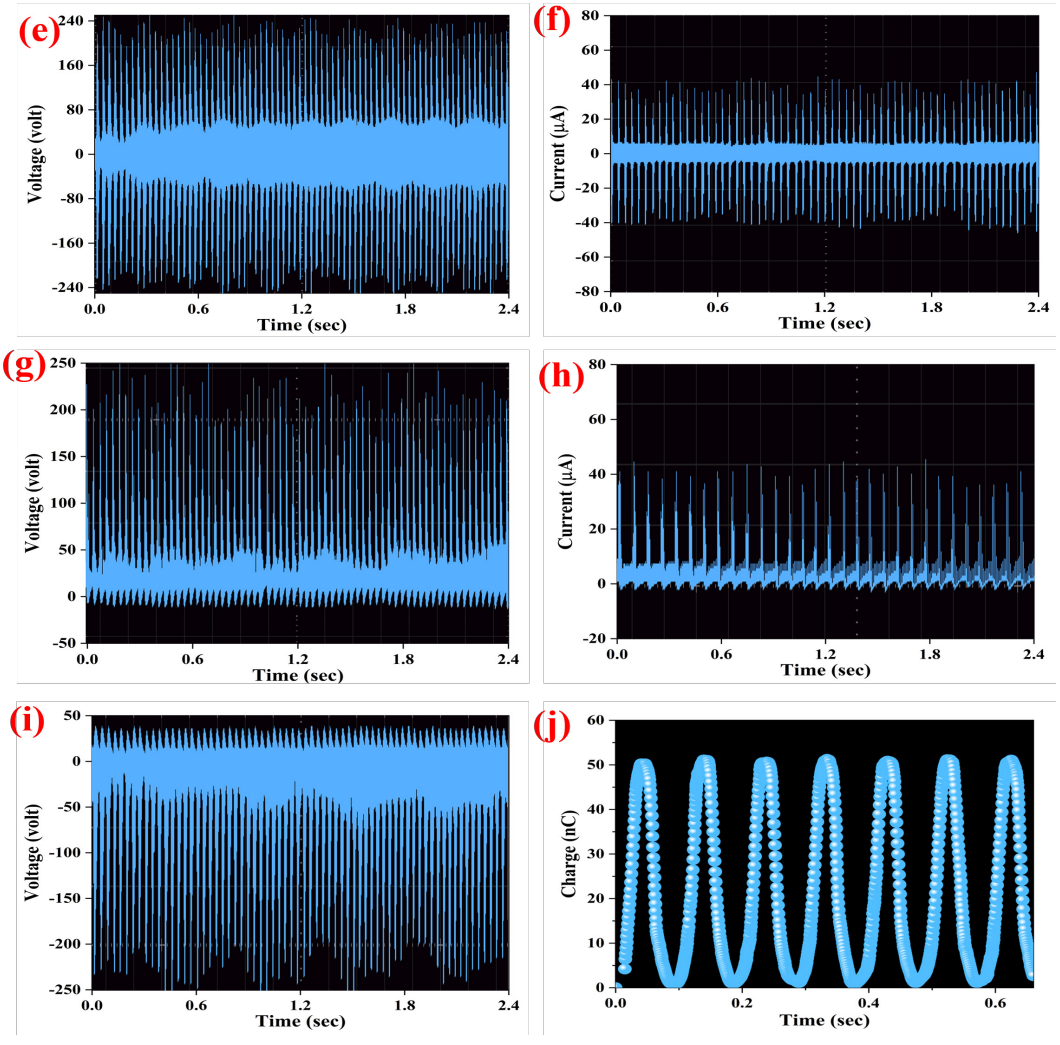
(e)
Voltage (volt)
Time (sec)
(f)
Current (μA)
Time (sec)
(g)
Voltage (volt)
Time (sec)
(h)
Current (μA)
Time (sec)
(i)
Voltage (volt)
Time (sec)
(j)
Charge (nC)
Time (sec)

Fig. 5.4 (a) detachable layer 1 **(b)**dropping fluoride water**, (c)** drying**, (d)** detection setup, **(e-h)** output AC and DC voltage and current, **(i)** reverse polarity test, and **(j)** generated charge.

The self-powered detection mechanism is explained in Chapter 1, section 1.3, with the voltage divider circuit used to generate voltage in the TENG (Fig. 1.4). If V_{IN}, R_C and R_S are the input voltage, the internal resistance of the circuit and the resistance of sensing film, then the output voltage drop across R_S will be,

$$\mathbf{V_{OUT}} = \{\boldsymbol{R_S}/(\boldsymbol{R_C} + \boldsymbol{R_S})\} \times \mathbf{V_{IN}} \qquad \textbf{(5.1)}$$

Eqn. 5.1 shows that the output voltage is directly proportional to the resistance R_S, i.e., the resistance of the detecting film. This phenomenon was used for the detection of fluoride, as the film resistance changes when interacts with fluoride water. The change in resistance causes a change in the output voltage as well. Here, the sensing element can detect even the slightest change in the R_S, by showing a changed V_{OUT}.

A film of LaPP was deposited on a scotch tape using spin coater, upon which two Ag electrodes were prepared and connected along the output of the rectifier circuit. The usage of scotch tape makes the process inexpensive, versatile, and easily discardable after use. After the fluoride water interacts with the sample, fluoride ions are trapped in LaPP. Hence, after each application, a fresh film is needed for the next detection. To save expenses on the new substrate, paper scotch is used here as substrate.

The fluoride ion detection mechanism is based on the interactions between the fluoride water and the sensing element causes the change in resistance of the material (R_S). For the detection of fluoride ions (measured by EUTECH ION 6+ USA), the film of LaPP nanospheres was spin-coated on paper scotch tape, and then 2 silver electrodes were made which were connected across the output of the rectifier circuit. The reason for using scotch tape is because of its low cost, and versatile nature, and it is easily discardable after usage. After the interaction with fluoride water, fluoride ions are stuck in the LaPP matrix. So, for a new sample, a completely new substrate is needed because it cannot be used again for different concentrations of fluoride ions. This is the core motive for using paper scotch tape-based single-use substrate. The whole mechanism of fluoride detection via self-powered way is dependent upon this method. One of the

main features of fluorine is its electronegativity, which is the highest among all the known elements.

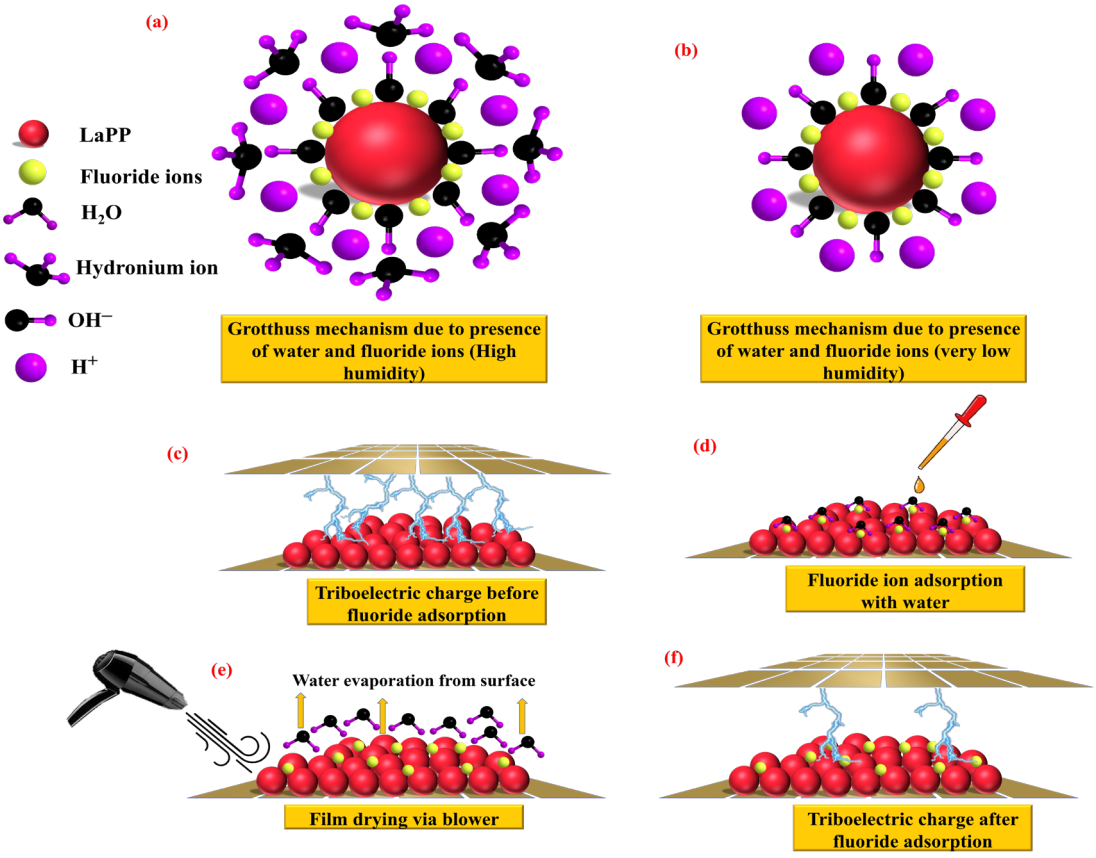

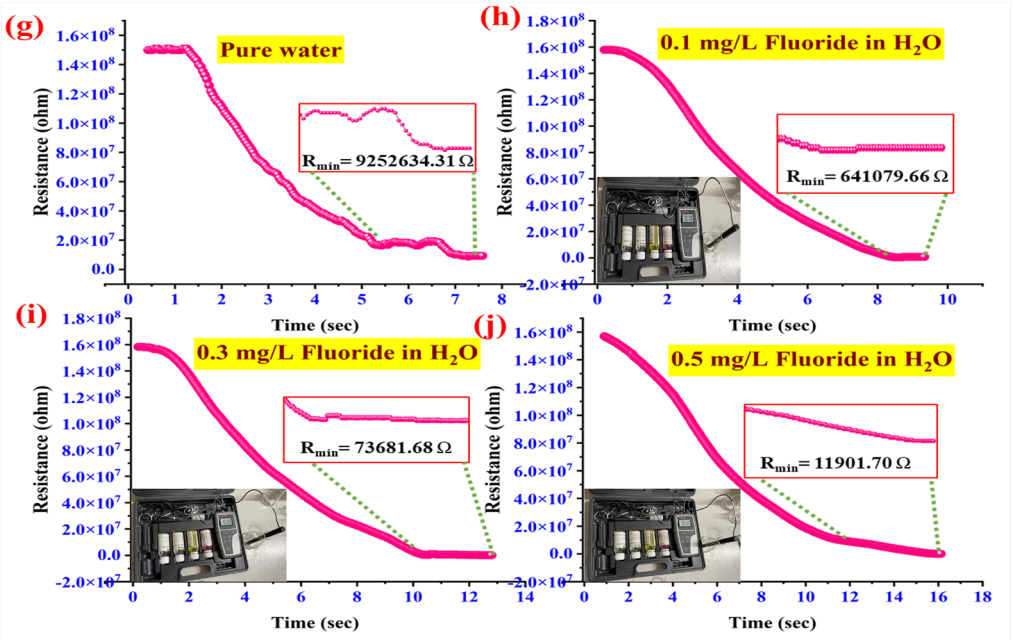

Fig 5.5 (a) Grotthuss mechanism during high amount of water and fluoride, **(b)** after drying at very low humid level, **(c-f)** steps involved in the Fluoride detection **(g-j)** change in resistance at different concentrations of fluoride.

So, it can attract an electron from a nearby atom more easily than any other element. Another basic mechanism to detect fluoride in water is the change in resistance of the film due to the presence of fluoride ions. Both of these principles of electronegativity and change in resistance are related to each other. The mechanism involved after dropping the fluoride water (High concentration) is shown in Fig 5.5 (a). When fluoride water was dropped (200 µL using micropipette) there are two reactions involved in the process **(1)** Change of resistance due to Grotthuss reaction in the presence of water, **(2)** Change in resistance due to reaction of Fluoride ions with Lanthanum atom. When a semiconducting material is exposed to humidity the water molecules rapidly dissociate into H^+ (Protons) and OH^- (Hydroxide ions) ions owing to the self-ionization or collision with the material surface. The Eqn. involved in this process:

$$H_2O \Leftrightarrow H^+ + OH^- \qquad \textbf{(5.2)}$$

The dissociated proton instantly reacts with the next water molecule and produces Hydronium ion (H_3O^+), following the relation:

$$H_2O + H_2O \Leftrightarrow H_3O^+ + OH^- \qquad \textbf{(5.3)}$$

In low humid conditions (10-40 %RH), there are a smaller number of water molecules present. Due to this only hydroxide ions remain on the surface of the material. These hydroxide ions provide the active sites for the hopping of protons onto the material surface as shown in Fig 5.5 (b). So, in very low humidity the conduction is governed by protons ions by hopping. In high humidity conditions (40-90 %RH), due presence of a high number of water molecules, now conduction is governed by protons by hopping onto the water molecules present on the material surface as shown in Fig 5.5 (a). Besides this, diffused H_3O^+ ions also release protons to an adjacent water molecule to form H_3O^+ and so on. This process of transfer of protons between the neighbouring water molecules is known as the Grotthuss mechanism, which results in

a significant decrement in electrical resistance. Fig. 5.5 (c-f) shows the steps involved in the Fluoride detection.

As mentioned earlier fluorine is highly electronegative and highly reactive. The reaction comprises in this process:

$$La^{3+} + HF \longrightarrow H^{+} + LaF^{+2} \quad \text{(Fluoride Complexing)} \quad \textbf{(5.4)}$$

$$La^{3+} + 3HF \longrightarrow 3H^{+} + LaF_3 \quad \text{(Electrostatic attraction)} \quad \textbf{(5.5)}$$

Due to the above reactions, there is the release of H^{+} ions on the surface of p-type LaPP material. This increases the total number of holes on the material surface, and hence decreases the resistance of the material surface. Hence in the early condition, when base voltage before the interaction of fluoride to the triboelectric layer was measured, it shows the increased voltage as the resistance of the film was also high. Conversely, when the triboelectric layer was exposed to fluoride water, the Material surface gained additional holes due to the interactions mentioned earlier. This enhancement in carrier concentration reduces the resistance of the film as shown in Fig. 5.5 (g-j). It can be seen from the insets of Fig 5.5 (g-j) that there is a gradual decrement in minimum resistance of the film when the concentration of fluoride in water is successively increased. It is very important to mention here that this work aims to find the effect of only fluoride (not the water) on the sensing device. So, to neglect the effect of water, a blow dryer was used for ~ 15 min. When the film was dried the resistance of the film again increases, but because of fluoride, it stops increasing above a certain level.

The most unique finding of this work is the change in voltage before and after dropping fluoride water (200 µL using micropipette) as discussed previously in Eqn. 5.1.

To observe the effect of only fluoride ions, the water on the film is dried with a dryer. In the dry film, the resistance again rises, but due to fluoride ions, it stops at a certain value. Fig 5.6 (a) shows the resistance curve of the film dried after applying fluoride water of 0.1, 0.3, and 0.5 mg/L concentrations. It can be clearly seen that the resistance of the dried films is completely different. Due to this, the output voltage will

also be different. Fig. 5.6 (b) shows a maximum voltage of the material ~242 volt without fluoride water. The output voltage of the material in 0.1 mg/L, 0.3 mg/L and 0.5 mg/L fluoride concentrations are shown in Fig. 5.6 (c-e) having a maximum output voltage. Because of the availability of fluoride on the surface of the film change in resistance occur and the voltage generated from the device also changes as suggested in Eqn.5.1.

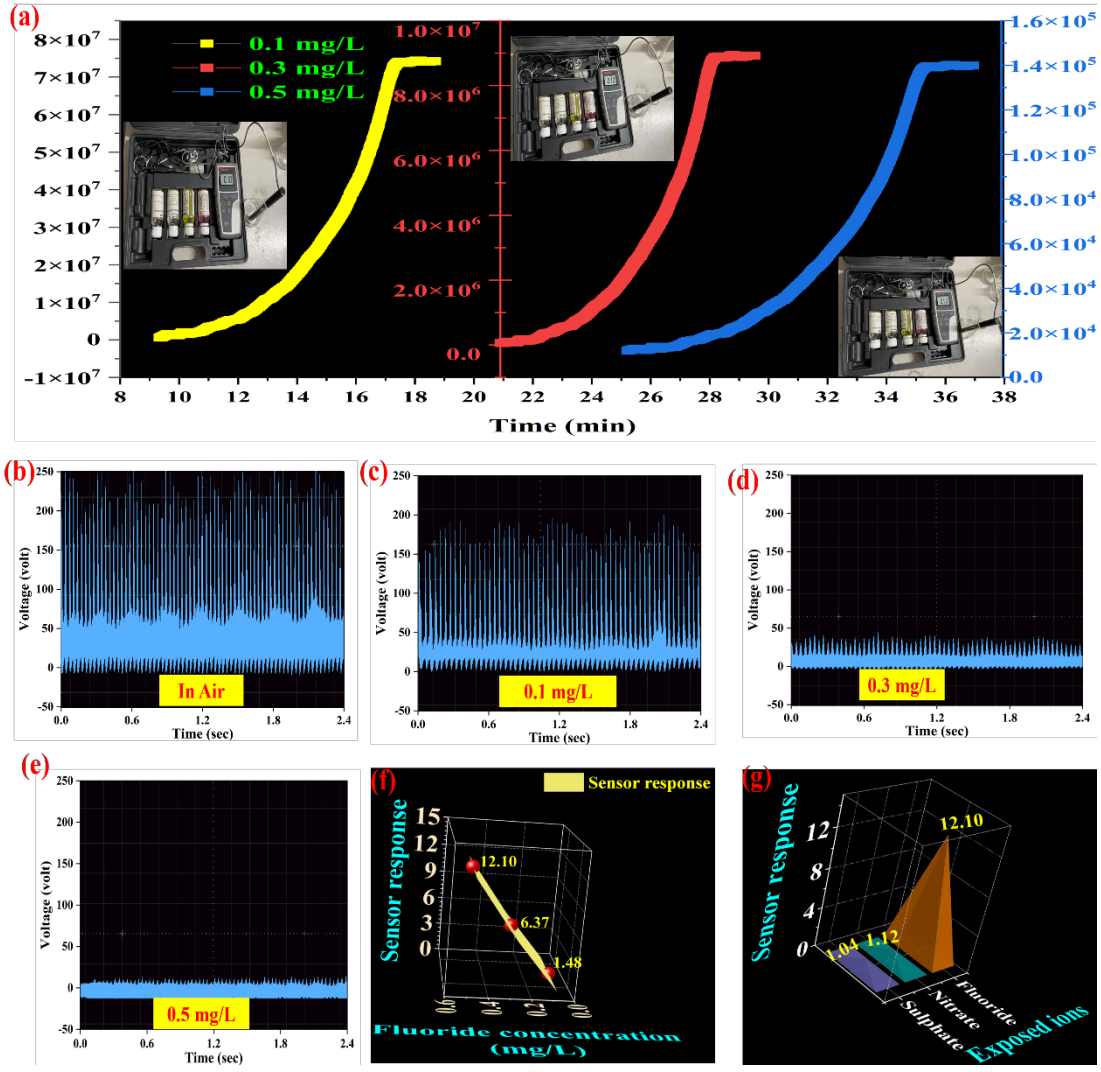

Fig. 5.6 (a-e) Output voltage at different concentrations of fluoride after drying, **(f)** Sensor response of present active sensor, and **(g)** Selectivity of the device.

There is a decrement in voltage for 0.1, 0.3, and 0.5 vol.%, which are 163 volt, 38 volt, 20 volt respectively.

The sensor response (SR) of the sensing element can be measured from,

$$SR = V_{air}/V_f \quad \textbf{(5.6)}$$

Where V_{air} and V_f are voltages in air and in the presence of fluoride respectively. Similarly, % Sensor response (% SR) is given by

$$\% SR = (V_{air} - V_f)/V_f \times 100 \quad \textbf{(5.7)}$$

The calculated SR at 0.1 mg/L, 0.3 mg/L and 0.5 mg/L are 1.48, 6.37 and 12.10 (Fig. 5.6 (f)), while % SR are 48 %, 537 % and 1110 % respectively.

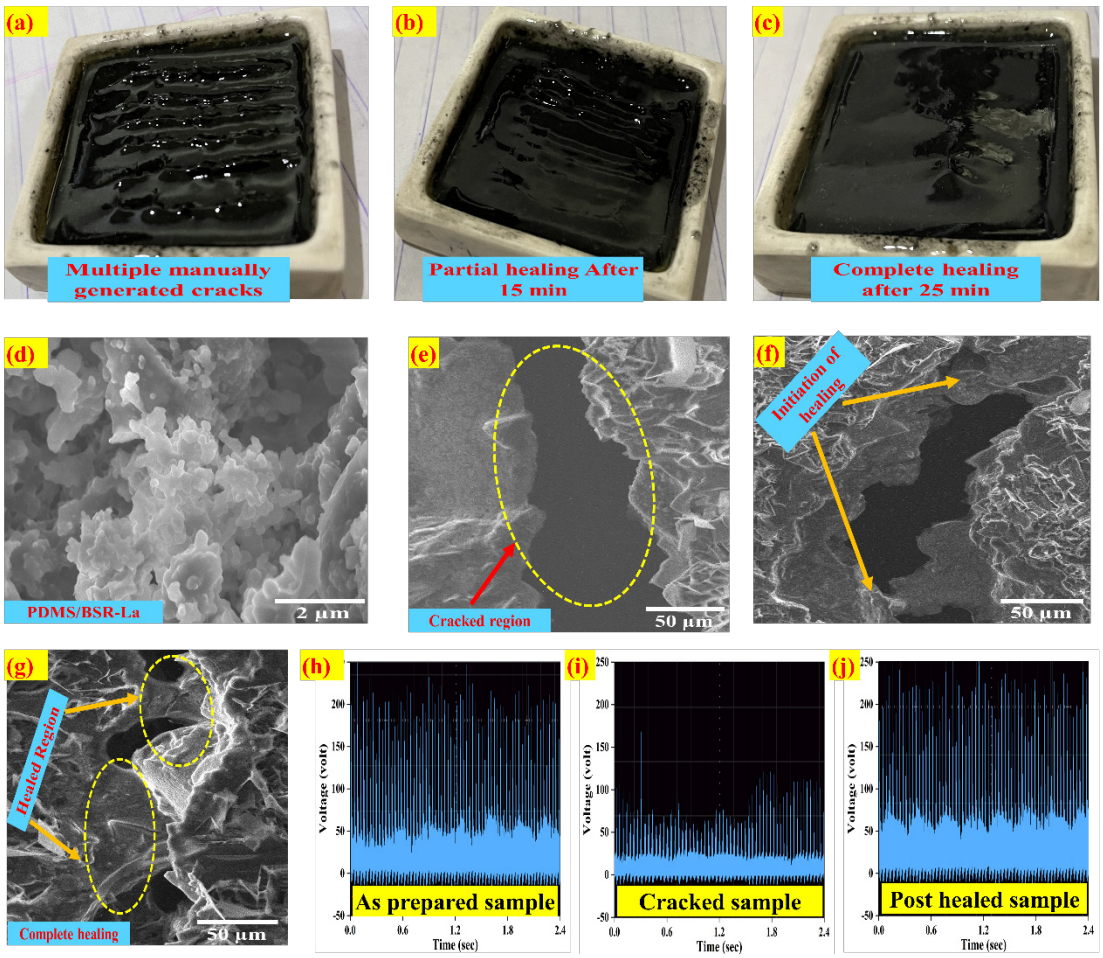

Fig. 5.7. (a-c) optical images of self-healing, SEM image of **(d)** PDMS/BSR-La, **(e)** Cracked sample, **(f)** initiation of healing, **(g)** complete healing, **(h)** output voltage of as prepared device, **(i)** output voltage of cracked device, and **(i)** output voltage of healed device.

Limit of detection (LOD) is another one of the most important characteristic of a sensor (especially in fluoride sensing), which is defined as the minimum concentrations of analyte that can be steadfastly perceived from the sensing device. The calculated LOD value in present work as suggested in previous literature is found to be 4.7 µM. The LOD value of the presented work (4.7 µM) is far better than previously reported works.

For the understanding of the selectivity of the material, it was exposed to nitrates and sulphates of 0.5 mg/L concentration. As can be seen in Fig. 5.6 (g), the device is more responsive toward fluoride than other ions.

5.3.6 Healing analysis in PDMS/BSR-La

PDMS/BSR-La composite showed speedy healing under 25 min in room temperature. The healing was witnessed via optical and SEM images as shown in Fig. 5.7 (a-g). To analyze this, PDMS/BSR-La was fabricated as mentioned earlier. The prepared composite was itched at multiple places with a spatula. Fig. 5.7 (a) is the freshly scratched composite. The healing was observed and pictures were taken time-to-time (Fig. 5.7 (b-c)). A section of the sample was also analyzed and the healing was confirmed using SEM as shown in Fig. 5.7 (d-g). In Fig. 5.7 (d), the PDMS can be seen well coated on BSR-La. Fig. 5.7 (e) was taken on the freshly scratched film, and Fig. 5.7 (f) was taken ~15 min after scratching, where we can see the initialization of the healing process. Fig. 5.7 (g) is the same film after ~25 min where we can see clear proof of healing. The output voltages were also measured during this process. Fig. 5.7 (h) is the output voltage corresponding to film before scratching showing a maximum voltage ~242 volt (1.58% RSD). Fig. 5.7 (i) is the output voltage in the scratched film, with maximum voltage ~95 volt (21.50% RSD), due to broken contact at the cracks. Finally, the healed sample provides a voltage ~240 volt (1.82% RSD) as shown in Fig. 5.7 (j). The composite gives a healing efficiency of ~99.9%. The healing is basically achieved by the reversible covalent bonding in the composite. The FTIR spectrum showed the presence of weak hydrogen bonds present in the sample. The healing capability comes from the reversible hydrogen bonds in the sample.

5.4 Conclusion

Here, an efficient, fast, inexpensive, and self-powered detection technique of fluoride ions in water has been demonstrated. Waste materials such as, used polythene bags, BSR rubber, and used plastic sheets are used in the device fabrication that describes waste-to-energy conversion capability with a maximum voltage ~242 volts and current ~40 μA. This chemisorption-based self-powered fluoride detection device displays a maximum sensor response of 12.10 and % sensor response of 1110 %. The TENG layer is prepared with PDMS/BSR-La nanocomposite that shows self-healing nature under only 25 min. Hence the device is self-healable with a healing efficiency of 99.9%. Also, the method of resistance measurement to minimize the water effect and corresponding output voltage nature of the detector is described in detail.

References

[1] S. Yadav, S.K. Bansal, S. Yadav, S. Kumar, Fluoride distribution in underground water of district Mahendergarh, Haryana, India, Applied Water Science. 9 (2019) 1–11.

[2] S. Srivastava, S.J.S. Flora, Fluoride in drinking water and skeletal fluorosis: a review of the global impact, Curr Environ Health Rep. 7 (2020) 140–146.

[3] D. Udhayakumari, Detection of toxic fluoride ion via chromogenic and fluorogenic sensing. A comprehensive review of the year 2015--2019, Spectrochimica Acta Part A: Molecular and Biomolecular Spectroscopy. 228 (2020) 117817.

[4] S. Kaza, L. Yao, P. Bhada-Tata, F. Van Woerden, What a waste 2.0: a global snapshot of solid waste management to 2050, World Bank Publications, 2018.

[5] P.M. Munnoli, S. Sheikh, T. Mir, V. Kesavan, R. Jha, Utilization of rubber tyre waste in subgrade soil, in: 2013 IEEE Global Humanitarian Technology Conference: South Asia Satellite (GHTC-SAS), (2013) 330–333.

[6] S. Singh, R.K. Tripathi, M.K. Gupta, G.I. Dzhardimalieva, I.E. Uflyand, B. Yadav, 2-D self-healable polyaniline-polypyrrole nanoflakes based triboelectric nanogenerator for self-powered solar light photo detector with DFT study, Journal of Colloid and Interface Science. 600 (2021) 572–585.

[7] Y. Li, Z. Zhao, Y. Gao, S. Li, L. Zhou, J. Wang, Z.L. Wang, Low-Cost, Environmentally Friendly, and High-Performance Triboelectric Nanogenerator Based on a Common Waste Material, ACS Applied Materials & Interfaces. 13 (2021) 30776–30784.

[8] G. Han, B. Wu, Y. Pu, A triboelectric nanogenerator based on waste plastic bags for flexible vertical interconnection system, Microsystem Technologies. 26 (2020) 3893–3899.

[9] K. Xia, Z. Zhu, J. Fu, Y. Li, Y. Chi, H. Zhang, C. Du, Z. Xu, A triboelectric nanogenerator based on waste tea leaves and packaging bags for powering electronic office supplies and behavior monitoring, Nano Energy. 60 (2019) 61–71.

[10] R.A. Shaukat, Q.M. Saqib, M.U. Khan, M.Y. Chougale, J. Bae, Bio-waste sunflower husks powder based recycled triboelectric nanogenerator for energy harvesting, Energy Reports. 7 (2021) 724–731.

[11] L. Han, M. Peng, Z. Wen, Y. Liu, Y. Zhang, Q. Zhu, H. Lei, S. Liu, L. Zheng, X. Sun, others, Self-driven photodetection based on impedance matching effect between a triboelectric nanogenerator and a MoS_2 nanosheets photodetector, Nano Energy. 59 (2019) 492–499.

[12] D. Zhang, Z. Xu, Z. Yang, X. Song, High-performance flexible self-powered tin disulfide nanoflowers/reduced graphene oxide nanohybrid-based humidity sensor driven by triboelectric nanogenerator, Nano Energy. 67 (2020) 104251.

[13] S. Badatya, D.K. Bharti, N. Sathish, A.K. Srivastava, M.K. Gupta, Humidity Sustainable Hydrophobic Poly (vinylidene fluoride)-Carbon Nanotubes Foam Based Piezoelectric Nanogenerator, ACS Applied Materials & Interfaces. (2021).

[14] X. Li, Z.-H. Lin, G. Cheng, X. Wen, Y. Liu, S. Niu, Z.L. Wang, 3D fiber-based hybrid nanogenerator for energy harvesting and as a self-powered pressure sensor, ACS Nano. 8 (2014) 10674–10681.

[15] X. Xie, Z. Wen, Q. Shen, C. Chen, M. Peng, Y. Yang, N. Sun, P. Cheng, H. Shao, Y. Zhang, others, Impedance matching effect between a triboelectric nanogenerator and a piezoresistive pressure sensor induced self-powered weighing, Advanced Materials Technologies. 3 (2018) 1800054.

[16] K. Xia, Z. Zhu, H. Zhang, Z. Xu, A triboelectric nanogenerator as self-powered temperature sensor based on PVDF and PTFE, Applied Physics A. 124 (2018) 1–7.

[17] H. Zhang, Y. Yang, T.-C. Hou, Y. Su, C. Hu, Z.L. Wang, Triboelectric nanogenerator built inside clothes for self-powered glucose biosensors, Nano Energy. 2 (2013) 1019–1024.

[18] Y. Zou, J. Liao, H. Ouyang, D. Jiang, C. Zhao, Z. Li, X. Qu, Z. Liu, Y. Fan, B. Shi, others, A flexible self-arched biosensor based on combination of piezoelectric and triboelectric effects, Applied Materials Today. 20 (2020) 100699.

[19] S. Wang, G. Xie, H. Tai, Y. Su, B. Yang, Q. Zhang, X. Du, Y. Jiang, Ultrasensitive flexible self-powered ammonia sensor based on triboelectric nanogenerator at room temperature, Nano Energy. 51 (2018) 231–240.

[20] S. Cui, Y. Zheng, T. Zhang, D. Wang, F. Zhou, W. Liu, Self-powered ammonia nanosensor based on the integration of the gas sensor and triboelectric nanogenerator, Nano Energy. 49 (2018) 31–39.

[21] K. Zhao, G. Gu, Y. Zhang, B. Zhang, F. Yang, L. Zhao, M. Zheng, G. Cheng, Z. Du, The self-powered CO_2 gas sensor based on gas discharge induced by triboelectric nanogenerator, Nano Energy. 53 (2018) 898–905.

[22] S. Saravanan, C.J. Mathai, M.R. Anantharaman, S. Venkatachalam, P. v Prabhakaran, Investigations on the electrical and structural properties of polyaniline doped with camphor sulphonic acid, Journal of Physics and Chemistry of Solids. 67 (2006) 1496–1501.

[23] N. Su, Improving electrical conductivity, thermal stability, and solubility of polyaniline-polypyrrole nanocomposite by doping with anionic spherical polyelectrolyte brushes, Nanoscale Research Letters. 10 (2015) 1–9.

[24] E.I. Iwuoha, S.E. Mavundla, V.S. Somerset, L.F. Petrik, M.J. Klink, M. Sekota, P. Bakers, Electrochemical and spectroscopic properties of fly ash--polyaniline matrix nanorod composites, Microchimica Acta. 155 (2006) 453–458.

[25] S. Singh, P. Yadav, M.K. Gupta, G.I. Dzhardimalieva, J. Yoon, C. Maiti, B.C. Yadav, Gigantic stimulation in response by solar irradiation in self-healable and self-powered LPG sensor based on triboelectric nanogenerator: Experimental and DFT computational study, Sensors and Actuators B: Chemical. 359 (2022) 131573.

Chapter 6

Conclusion and Future scope of research work

This chapter gives the closing remark and comparative analysis of all synthesized materials and fabricated devices. This chapter deals with the summarised information of the material characteristics, sensing output, and future scope of all the chapters mentioned previously. A chapter wise overview of this thesis including the materials, their application, sensor response, presence of self-healing and self-powered ability along with response/recovery times is depicted in this chapter. A comparative analysis of all the materials synthesized and fabricated sensors were also presented. Also, this chapter gives the future possibilities of research work in this area.

6.1 Conclusion

Mechanical damage along with the need for a power source to operate sensing devices are two main drawbacks during the functioning period. Self-healing and self-powering characteristics are used separately nowadays to tackle these problems. As discussed in Chapters 2, 3, 4 and 5 that previously developed sensors don't have the capability of self-healing and self-powering simultaneously. We have successfully incorporated both functionalities in different types of sensors (Photo sensor, LPG sensor, and Fluoride sensor). TENG was used in powering these different kinds of sensors. As discussed earlier in chapter 1 that polymers were preferred over any other material in TENG for triboelectrification because of the better charge holding properties and rigidity. We have incorporated different types of polymeric materials (2-D and spherical) in TENG for enhanced output performance. Different characteristics of developed sensors are concluded as follows:

6.1.1 Improved sensing behaviour of self-healable solar light photodetector based on core-shell type $Ni_{0.2}Zn_{0.8}Fe_2O_4$@ poly (Urea-Formaldehyde)

In this work, we elaborated a procedure to prepare and fabricate a bi-layered photo-detecting device, which can redeem its actual functionality after damage occurs in its physical structure. In this work two layers were used, microcapsule-based bottom layer and an upper NZF sensing layer. Via the free-flowing skill of flaxseed oil, NZF nanoparticles are able to fill in the damaged areas when the microcapsules are ruptured. Here flaxseed oil acts as a transporting agent, which carries NZF nanoparticles towards the cracks. The NZF nanomaterial was synthesized via citrate acid aided sol-gel method, and was used as the sensing element. The U-F microcapsules with flaxseed oil and NZF core were prepared by oil emulsion method and used as a self-healing material. The preparation methods are very easy, simple and inexpensive. Different characterization techniques were employed to realize the thermal stability, chemical bonding, elemental analysis, optical band gap, and crystal information of the synthesized materials. The polycrystallinity along with the purity of NZF was established by XRD investigation. The encapsulation of NZF inside U-F polymer was proved by TEM and SAED and FTIR analysis. Via TEM analysis, the average NZF

dimension was found as ~20 nm. The measured band gap of NZF via Tauc plot in UV-Visible analysis was ~3.51 eV. The effective restoration of the film was confirmed by SEM and EDS analysis. By regaining the original structure, the sensing element was competent to reinstate the sensing properties. The response/recovery time of the uncracked sample was 1.74/3.28 sec, while those for the healed sample were 1.75/2.84 sec. The most important parameter of healing efficiency was calculated, which tells the restoration of electrical properties of the fabricated photodetector. The sensing capability of the healed sample was reproducible up to 98.5%. These outcomes approve that a photodetector is successfully prepared that can re-establish its sensing properties after any mechanical damage.

6.1.2 2-D self-healable polyaniline-polypyrrole nanoflakes based triboelectric nanogenerator for self-powered solar light photodetector

Here in this research work, PANI-PPY NFs with self-restoring ability prepared via a simple chemical method has been demonstrated. PANI-PPY was synthesized using low temperature aided oxidative polymerization method. The method of preparation is very simple to form nano-dimension (~30 nm) 2-D NFs. A high-resolution SEM image of NFs confirmed the smallest width of NF ~30.35 nm. The measured band gap of PANI-PPY via Tauc plot in UV-Visible analysis was ~1.85 eV. The NFs formation was also explained in this chapter via thermal scission and surfactant effect. Self-healing ability was found absent in earlier published self-powered photo sensors that can change the output enactment of the device after damage. Therefore, this work emphasized on advances in self-recoverable and self-powered photo sensors. TENG measurements were taken to explore the performance of TENG. A maximum voltage of 149 volts, a maximum current of 16 µA, a maximum current density of 0.56 μAcm^{-2}, and a maximum power density 83.56 μWcm^{-2} were detected from the sensing device that illustrates greater performance against the previously testified self-powered sensors. Least response/recovery times were observed for 30 mW/cm^2, which are 0.41 sec and 0.45 sec. The % response at 0, 30, 60 and 100 mW/cm^2 illumination were observed to be 0, 17.78, 78 and 278 % respectively with sensitivity 2.78 $\%response/mWcm^{-2}$. Most significantly TENG doesn't display any foremost variations in voltages pre and post-healing. The most novel characteristic of this

research is acetone-supported rapid self-restoration presented in PANI-PPY nanoflakes. The maximum healing efficiency of 99.8% was accomplished in this work.

6.1.3 Gigantic stimulation in response by solar irradiation in self-healable and self-powered LPG sensor based on triboelectric nanogenerator

Waste energy has been utilized in this work for powering a sensor. A self-powered, self-healable, and visible light-enhanced LPG sensor-based PANI-PPY (2P) 2-dimensional nano-sheets is demonstrated. The procedure to synthesize PANI-PPY (1:4) was similar to what followed in Chapter 3 except for the ratio of monomer. The copolymer was thoroughly investigated using different characterization techniques. Multiple nano-flakes can be found all through the sample with minimum thickness of ~24.76 nm. HRTEM analysis was performed to authorize a 2-dimensional polymer structure. FTIR, RAMAN, XRD, and TGA analysis were also performed to characterize the sample. The measured band gap of PANI-PPy via Tauc plot in UV-Visible analysis was ~2.02 eV. The BET analysis confirmed the specific surface area, average pore size, and mean pore volume of ~125.6 m^2/g, 30.23 nm, and 0.086 cm^3/g respectively. The material showed brilliant LPG detection below its LEL when illuminated with visible light at room temperature. The sensor was operated with TENG (3P) that generated an output voltage and current of ~142 volt and 80 µA respectively. Using the output of TENG as a power source, the sensing element exhibited a maximum sensor response of ~94.67 and sensitivity of ~52.67 SR/vol.% under the influence of 30 mW/cm^2 visible light. The material was able to detect very low concentrations of LPG almost instantaneously with response/recovery times 172/580 ms. Self-healing ability was also successfully introduced in the TENG layer to regain its properties after any damage. The Maximum healing efficiency of ~99.7% was achieved here in this work.

6.1.4 Waste material-based self-healable and self-powered Fluoride ion detection device: An unexplored and highly responsive detection method

This work establishes a unique, cost-effective, and time-efficient detection method of fluoride ions in water. The device is fabricated using waste materials like BSR rubber, used polythene bag, and used plastic sheet, which validates the waste to energy conversion ability with a maximum output voltage of ~242 volts and 40 µA

current. A new technique is used and validated to detect fluoride ions, using a TENG-based device fabricated using hazardous waste (BSR). BSR decorated with Lanthanum doped Polyaniline-Polypyrrole (LaPP) nanospheres (BSR-La) mixed in PDMS (PDMS/BSR-La) was used to form one layer of the TENG that is self-healable in nature. LaPP nanomaterial with a perfectly spherical shape within a size of 14-50 nm was confirmed by SEM. The elements present in the LaPP were confirmed by both EDX and elemental mapping. FTIR, XRD, and UV-Visible analysis were also performed to characterize the sample. The optical band gap measured from the Tauc plot was ~1.58 eV. The present chemisorbed-based self-powered fluoride detection device shows a maximum sensor response of 12.10 and a % sensor response of 1110 %, which is very high. The calculated LOD of the present device is 4.7 µM. The self-healing ability of PDMS/BSR-La nanocomposite shows fast healing in ~25 min with a healing efficiency of 99.9%, which is one of the unique features of this device. Besides that, this manuscript also demonstrates the method of resistance measurement to minimize the water effect and corresponding output voltage behavior of the sensor. In summary, this work establishes the exclusive way to detect fluoride using waste materials.

In conclusion, both physical and chemical sensors with self-restoring and self-powering capabilities were successfully demonstrated. Besides this, A unique new method to detect fluoride ions well below permissible limit was demonstrated with self-healing and battery-less ability.

A chapter-wise overview of this thesis including the materials, their application, sensor response, presence of self-healing and self-powered ability along with response/recovery times is depicted in Table 6.1.

Table 6.1 Chapter-wise information and characteristics of developed material and sensor.

Chapter No.	Sensing element	Application	Max. Sensor response	Self-healing ability and efficiency	Self-powered ability	Min. Response time	Min. Recovery time
2.	**$Ni_{0.2}Zn_{0.8}Fe_2O_4$@ poly (Urea-Formaldehyde) microcapsules**	Photo sensor (Visible light)	11	Present (98.5%)	Not present	1.74 sec	3.28 sec
3.	**2-D Polyaniline-Polypyrrole Nanoflakes**	Photo sensor (Visible light)	3.78	Present (99.8 %)	Present	0.41 sec	0.45 sec
4.	**2-D Polyaniline-Polypyrrole Nanosheets**	Visible light-induced LPG sensor	94.67	Present (99.7 %)	Present	172 ms	580 ms
5.	**Lanthanum doped Polyaniline-Polypyrrole nanospheres**	Fluoride ion sensor	12.10	Present (99.9 %)	Present	–	–

6.2 Future scope of research work

- Other functionalities like self-cleaning, shape memory, etc. along with healing and self-powering may be incorporated into a single device.
- Other polymers with different nano dimensions like 2-D, 1-D, and 0-D may be explored and incorporated into TENG for better performance.
- Other polymers and materials may be explored for enhanced self-healing ability.
- Other types of chemical, gas and biological sensors like CO_2, ammonia, and different acids may be explored with PANI-PPY nanostructures.
- Further studies of nanostructured polymer and formation mechanism can be explored.
- Effects of different synthesis parameters like precursors, concentrations, solvents, pH, temperature, etc. on the prepared material can be studied further for optimization

Appendix Experimental Methods and Characterization Techniques

The techniques utilized all through the preparation, fabrication and characterization of the nanomaterials are designated in this section. The synthesis of metal oxides, conducting polymers and their nanocomposites were executed by citrate gel, oxidation polymerization, and micro emulsion methods. The sensing film and the TENG layers were fabricated using spin coater. For the investigation of different properties, the prepared specimens were tested using SEM, TEM, EDS, SAED, UV-visible spectroscopy, FTIR, XRD, Raman, TGA, etc. Further, the changes in the resistance of the nanomaterials in accordance with applied light, gas molecules, and hazardous ions were investigated with Keithley electrometer.

A.1 Introduction

The methodology as well as several experimental techniques followed in the synthesis of different nanomaterials and their nanohybrids have been elaborated. Different techniques like XRD, SEM, EDS, FTIR, TEM, SAED, Raman, TGA and UV-vis spectroscopy were employed to understand and illustrate the size, shape, structure, compositions, and electrical, thermal, optical properties of the materials. Some of the practices used in this thesis work is defined in detail in this chapter.

A.2 Methodology of Present Work

Succeeding stages were carried out for the present investigation:

1) Synthesis of the chosen nanomaterials.
2) Fabrication of the film and TENG layer.
3) Exploration of various features and properties of the synthesized nanomaterials like, morphology, phase information, bonding, composition, optical absorption, band gap, encapsulation, particle size, crystallinity, etc. utilizing relevant characterization procedures as follows:

a) **X-ray Diffraction (XRD):** XRD is used to investigate the crystallinity and to identify the phases.
b) **Scanning Electron Microscopy (SEM):** It is used for achieving the information about the surface morphology of the material.
c) **Energy Dispersive X-ray Spectroscopy (EDS):** EDS helps to recognize the fundamental elements existing in the specimen.
d) **Transmission Electron Microscopy (TEM):** TEM micrographs expose the topography of the material with internal structure, grain distribution, grain diameter etc.
e) **Selected Area Electron Diffraction (SAED):** SAED patterns help to know about the crystallinity and the crystal planes present in the crystalline materials.
f) **UV-visible Spectroscopy:** It provides the optical absorption of the material, from which the optical band gap of the material is measured.

g) **Fourier Transform Infrared (FTIR) Spectroscopy:** FTIR distinguishes the chemical bonds existing in the material.

h) **Raman Analysis:** It recognizes the molecular vibrational bonds present in the materials.

i) **Keithley electrometer:** It is used to measure the electrical resistance of material at different environments.

j) **Digital CRO:** It is used to observe the AC and DC current and voltage generated by nanogenerator device.

A.3 Synthesis

A.3.1 Citrate gel method

Citrate gel process is a distinct part of the sol-gel method. Here, along with metal nitrate salts, citric acid is also used in precursors, as a chelating agent. Here, the gel condensed from the sol experience auto-ignition owing to citric acid, working as a chelating agent.

Citrate gel method contains self-ignition caused due to self-maintained thermally stimulated redox reactions amid the concoction of precursor solutions. During synthesis, metal nitrates and citric acid in necessary amounts are mixed in deionized water and the pH of the mixed solution is altered from acidic to basic. Heating this basic mixture evaporates the water and changes the watery solution into thick gel system, which gradually converts into xerogel. At a point, exothermic reactions take place in the xerogel network, and the additional heat produced in the system auto-ignites the entire specimen. After complete burning, only powder-like nanomaterial remains inside the beaker.

This scheme is favoured because it is very cost-effective and less complicated procedure. However, the final product has to go experience heat treatment after production for proper crystallization and impurity removal.

A.3.2 Oxidative-polymerization technique

This method belongs to one of the least complicated and cheap polymerization routes for the synthesis of the conducting polymers at room temperature. Polyaniline, polythiophene, polypyrrole, etc. conducting polymers are typically prepared using this technique. The procedure involves inorganic or organic oxidizing agents. Occasionally, surfactants are also incorporated to control the size and shape of the polymers.

Here, the polymerization is originated via the production of cationic radical sites in each monomer. A pair of monomers then link together by covalent bonds, and form a dimer. The dimer then connects to another monomer to create a trimer and so on. Various kinds of arrangements like head-to-tail, head-to-head tail-to-tail can be perceived in the networking of the monomers. Therefore, extensive distinctions of monomers can be merged to create chains of polymer using this method.

A.3.3 Oil-in-water micro-emulsion process

Synthesis via this technique results in large assembly of polymers in a suspension arrangement (oil-in-water). The key components in this method are water, monomers (water insoluble), stabilizer, emulsifier (surfactant) etc.

Generally, the monomer is dripped in aqueous medium that produces droplets suspended in water. Stabilizers and/or surfactants are used to stabilize the droplets and to stop the agglomeration between the droplets. The surfactants construct thin coating around the droplets and repulsion between the droplets are created from the electrostatic charge of the surfactant molecules. Once polymerization occurs, various distinct well separated polymeric particles are formed in the droplets.

A.4. Annealing

Heat treatment of a specimen includes heating and cooling of the material at definite settings to modify its structure, morphology, crystallization, and to alter its mechanical, chemical, and physical characteristics, and to eliminate impurities. There are six different categories of heat treatments typically used: annealing, stress relieving, normalizing, quenching, tempering and hardening. Amid these, annealing mainly

includes warming the material upto a definite temperature at a definite rate, sustaining the temperature upto a definite time, and lastly cooling down at a definite rate. There are two kinds of annealing treatments: slow thermal annealing (STA) and fast thermal annealing (FTA). In STA, at room temperature, the specimen is positioned inside a furnace (Fig. A.1) and heated progressively upto a certain temperature, while in FTA, the sample is placed inside a furnace that is pre-heated in the desired temperature.

Fig. A.1 Experimental setup of tube furnace: Matrex (NSRL, BBAU, Lucknow)

Annealing can be executed in diverse environments: atmospheric air, vacuum, or certain gas. Annealing a sample refines crystal structure, removes impurities, encourage further crystallization, modifies different chemical, electrical, and magnetic properties etc.

A.5. Fabrication techniques for thin film

A.5.1 Spin coating method

Spin coater (Fig. A.2) is used for thin film fabrication using a consistent gel of the nanomaterial. The instrument generally contains a vacuum pump to clutch the substrate placed on top of a rotator and a potent motor to spin the rotator. In this process, some drops of the dispersion is put on the middle of the substrate and the rotator is

gyrated upto needed speed (upto 6000 rpm) for a certain time. Centripetal acceleration is generated when the substrate is revolved. This assists the dispersion to spread out consistently on the substrate.

Fig. A.2 Experimental setup of spin coating: Matrex (NSRL, BBAU, Lucknow)

The thickness of the film is decided from controlling the time and speed of revolution. The thickness of the film reduces as the speed and/or time increases. However, the surface tension, viscosity of the fluid, etc. aspects also subsidizes the film thickness too. Finally, the film is dried either by heating (~100 ˚C) or at room temperature.

A.6. Characterization techniques

The synthesized nanomaterials and their nanocomposites were characterized by various techniques as revealed below:

A.6.1 X-ray Diffraction (XRD)

It was found by Max von Laue in 1912, that the materials that are crystalline in nature, act as 3-dimensional diffraction grating for incident X-ray beams, as the interplanar spacing of the crystal is comparable with the wavelength of the X-rays.

X-ray diffraction (Fig. A.3) analysis is mainly utilized to investigate the crystallographic phases and other crystal information. The process involves the constructive interference of monochromatic X-rays that are diffracted from the planes of a crystal.

Fig. A.3 Experimental setup of XRD: Malvern Panalytical Ltd – X'Pert^3 Powder (USIC, BBAU, Lucknow)

The applied X-rays are created from a CRT (Cathode Ray Tube), and sifted to attain radiation with single wavelength, and guided to get intense and fixated to the specimen. The X-rays falling on the material get diffracted from the planes present in the crystal. The constructive interference of these diffracted rays generates the X-ray diffraction configuration which fulfills the Bragg's law:

$$\mathbf{2d\sin\theta = n\lambda}$$

Where, d, 2θ, n and λ are the spacing between diffracting planes along same direction, Bragg angle, diffraction order and wavelength of the beam.

The diffractions and relevant angles are distinguished using a detector that gives a pattern to analyze further. The diffraction pattern is also equated with the standard

reference outlines conveyed by the Joint Committee on Powder Diffraction Standards (JCPDS) and International Centre for Diffraction Data (ICDD) to recognize the material.

The XRD plot of any material delivers crucial information like, presence of contaminants, existence of phases, degree of crystallinity, presence of any amorphous nature, lattice parameters, direction of alignment of the crystallites, size of crystallite, interplanar spacing between the crystal planes along same direction, micro strain etc. The average crystallite size at a specific direction is generally computed from the Scherrer formula,

$$\mathbf{D} = \frac{k\lambda}{\beta cos\theta}$$

Where, D = average crystallite size, k = polarization factor, β = FWHM of diffraction peak.

A.6.2 Scanning Electron Microscopy (SEM)

Scanning electron microscope is employed for the disclosure of the surface morphology of the sample via glancing over the surface of the material using a fixed ray of electrons excited at high energy. The applied electrons intermingle with the elemental atoms existing on the surface of the material, and creates diverse signals that encompass the accurate data about the surface morphology even at the nanometer scale. Usually, in almost all viable SEM instruments (Fig. A.4), the secondary electrons emanated from the atoms are perceived to achieve the essential info. A SEM device is equipped with an electron gun that has a filament prepared with lanthanum hexaborate or tungsten serving as the electron source to provide electron rays. A voltage is applied externally to heat up the filament, to produce flow of electrons. The electron stream is densified using a condenser lens that limits the current of the electron flow and gets rid of the high-angled electrons from the stream of electrons. An additional condenser lens associated next narrows down the electron beam further, in order to make the beam more concentrated. Adjacent to the end of the device, scanning coils are positioned that focuses the beam of the electrons more.

Fig.A.4 Experimental setup of SEM: JEOL JSM-6490 LV USIC, BBAU, Lucknow)

Additionally, when the electron beam hits the surface of the sample, the scanning coils gather all the secondary electrons and escort them on the way to the detector. The detector then calculates the secondary electrons, strengthens the current intensity and uses these to envision the appearance of the material surface on a computer screen.

Numerous interactions take place when electron beam interacts with the surface atoms of the sample as listed below:

- **Secondary electrons:** When the electron rays fall on the sample surface, they handover some energy to the K-shell electrons and ionizes the surface atoms of the sample. The electrons detached from the material surface are known as the secondary electrons. These secondary electrons hold all the evidence associated with the material surface.
- **Backscattered electrons:** These electrons are backscattered or reflected back from the volume of the material. It happens as the falling electrons strike a surface atom that is perpendicular with the trail of incidence. The number of generated backscattered electrons is equivalent with the atomic number of the sample. Because of this purpose, one can use the backscattered electrons to identify the chemical composition of the sample.

- **Cathodoluminescence:** When the ray of electrons is made fall on the specimen surface, they stimulate the surface atoms. When these atoms go back to the analogous ground state, they emanate photons. This practice is called cathodoluminescence. If suitable detector is used, real colored images can be received.
- **Auger electrons:** When the electron is separated from the core of the atom, an empty space is generated that is filled by higher energy electron discharging energy which is transferred to a different electron, which is then cast out as Auger electron. Auger electron has a distinctive energy feature that is exclusive for each elements. Hence, the auger electrons are detected to give the compositional information of the specimen.

A.6.3 Energy Dispersive X-ray Spectroscopy (EDS)

SEM can also carry out the inspection of discriminatory point sites located on the surface of the material and gives a qualitative analysis of the elements present in the specimen via EDS. It is a qualitative apparatus associated with the SEM for X-ray micro-investigation that means it informs the study relying on the output signal containing the summits of the energy tallies. X-ray ionizes the surface atoms and a solid state detector (SSD) of enhanced resolution detects the outcome, and then its consequences regarding the elements present in the sample is scrutinised by an analyser.

A.6.4 Transmission Electron Microscopy (TEM)

In TEM, extremely focused, highly energetic beams of electrons are passed through the sample that interacts with the material and gives characteristic radiation and some additional particles, and generates 2-dimensional pictures consisting of 3-dimensional restorations using a magnification lying between ~50x-10^6x. The splendid spread of magnification is the outcome of minor wavelengths of the incident electrons.

Fig. A.5 Experimental setup of TEM: FEI Tecnai TF20 (CRF, IITD, Delhi)

Here, the output signal (Fig. A.5) is conquered from both deflected and undeflected electrons which go in through the width of the material. Manifold magnetic lenses at and below the specimen stage are accountable for conveying the output signal to a detector that is normally a screen, a video camera, or a film plate. There are two distinct kinds of specimen examinations proposed by TEM:

- **Image mode:** In this case, an image of the irradiated area of the specimen is generated. The contrast of the image can be ascribed to numerous mechanisms: contrast in thickness because of non-uniform thickness of specimen, mass contrast caused by the separations in space between different elements, contrast of diffraction in crystals due to the incident electrons scattered from the defects in sample and phase contrast.
- **Diffraction mode:** In this mode, electron diffraction pattern can be received in place of topography of the material. The diffraction pattern is analogous to the X-ray diffraction pattern of the same material. Single spot pattern is produced by a single crystal, on the screen, while, ring-like patterns are obtained from polycrystalline materials. Diffused halo-like patterns are achieved from the amorphous material.

A.6.5 UV-visible Spectroscopy

Ultraviolet and visible (UV-vis) absorption spectroscopy (Fig. A.6) is used to study the attenuation of a light beam when it voyages through a material. Ultraviolet and visible light of definite energy are ample to encourage the electrons of outer levels to levels with higher energy. The energy absorption can happen at single wavelength or can be wide-spread over a spectral section reliant to the characteristics of the material. Generally, this technique is practised to molecules or inorganic complexes in solution. This spectroscopy is beneficial in characterizing the transmission, absorption, and reflectivity of materials.

Fig. A.6 Experimental setup of UV-Visible spectroscopy: Thermo Scientific-Evolution 201 (NSRL, BBAU, Lucknow)

The advancement of an electron from the ground state at energy E_i to higher energy state at E_f can be possible, when the material absorbs radiation of the wavelength $\lambda = hc/(E_f-E_i)$ (c = speed of light, h = Planck's constant). The new higher energy state of the electron is known as an excited state. The time period of the existence of the excited states are generally very short (femto seconds to microseconds). The energy difference of the first excited states and the grounds states of most of the materials falls in the UV and/or visible sections of the optical spectrum. In practise, UV-visible spectrophotometers are used to determine absorbance that is the logarithmic ratio

between the transmitted and the incident intensities. The spectrum is further analysed by plotting $(\alpha h\nu)^2$ vs $h\nu$, measured from the equation:

$$\alpha h\nu = A(h\nu - E_g)^n$$

Where, A = constant, α = absorption coefficient, value of n portrays the type of transition. A straight line is obtained when $(\alpha h\nu)^2$ vs light energy ($h\nu$) curve is extrapolated towards the energy axis. The intercept of the straight line on $h\nu$ axis corresponds to the optical energy band-gap (E_g) of that material.

In a standard UV-vis spectrophotometer, a beam of incident light is split in two halves, one part is traversed through a transparent cell containing a dilute solution of the material to be analysed, and other half is travelled through an alike cell holding just the solvent used as reference. The instrument makes a comparison of the intensities of the transmitted beams. If the material absorbs light of certain wavelength, the intensity of the specimen beam will be less than that of the reference beam. Absorption/transmission/reflection of radiation by a specimen is observed by irradiating different wavelengths ranging from 380-800 nm and plotted to display the spectrum that is a plot between the wavelengths vs the absorption of light at each wavelengths.

A.6.6 Fourier Transform Infrared (FTIR) Spectroscopy

For the recognition of inorganic, and/or organic bonds (functional groups) existing in a material, FTIR analysis is performed. The expression 'Fourier transform' indicates a contemporary upgradation where the gathered information is altered from an interference pattern to a spectrum for better realization. Now-a-days FTIR apparatuses (Fig. A.7) are totally computer-functioned, which aids them to be more sensitive and quicker than the older dispersive instruments.

When a sample is radiated with specific wavelengths of light in IR range, the absorptions are treated as the characteristic bands analogous to definite chemical bonds present in that material. The chemical bonds present in a molecule can be spotted from the explanation of the IR absorption spectrum. FTIR spectra of pure materials are distinctive, hence they are often labelled as 'fingerprint' absorptions. The organic

compounds mostly own quite rich FTIR spectra, while inorganic ones have simpler spectra. Typically, the spectrum of an unknown/known material is acknowledged by equating the output data with a library of known complexes.

Fig. A.7 Experimental setup of FTIR: Thermo-Scientific Nicole 6700 (USIC, BBAU, Lucknow)

Counting on the elements and the bonds present in a material, the molecular bonds are likely to oscillate at definite frequencies. Any certain bond can quiver at numerous explicit frequencies. From quantum mechanics, it can be said that, those frequencies fit in the ground level and many excited levels. The frequency of a molecular vibration can be amplified and the bond can be agitated by absorbing light energy in IR region. In case of any transitions amid two energy levels, the light energy should specifically match with the energy difference among the two levels, i.e., the ground level (E_i) and the first excited level (E_f). Hence,

$$\mathbf{E_f - E_i = hc/\lambda}$$

A.6.7 Raman analysis

Raman spectroscopy (Fig. A.8) delivers information about the molecular vibrations to recognize the material in practise. Here, monochromatic laser light is made fall on a material and the lights dispersed from the sample are spotted. Most of the

dispersed light own the frequency analogous to that of the incident light, this is elastic scattering termed as Rayleigh scattering. A tiny segment of the dispersed light gets energy-shifted from the incident light owing to inelastic interactions among the vibrational energy levels of the specimen molecules and the incident light. Drawing a curve among the intensity of this 'shifted' light vs frequency brings in the Raman spectrum of that material. The Raman spectra are graphed with the incident laser frequency to confiscate the Rayleigh band. In the Raman spectrum of a material, the band occurs at frequencies analogous to the certain vibrational energy levels of various functional groups.

Fig. A.8 Experimental setup of RAMAN analysis: Renishaw inVia reflex micro-Raman spectrometer (CSIR-AMPRI, Bhopal)

In 1928, Dr. C. V. Raman witnessed that a minor fragment of the incident visible light was scattered by definite molecules, whose wavelength diverges from the incident light. The shifts in energy is influenced by the chemical assembly of the molecules. The perception of Raman scattering elaborates that the events occur from the identical quantized vibrational deviations which are escorted with infrared absorption. For this reason, the variance in wavelength amongst the incident and scattered radiation matches with the wavelengths in the mid-infrared section.

When a monochromatic laser light of frequency υ_0 excites molecules and changes them in oscillating dipoles, they release light having three different frequencies.

- Photon having frequency υ_0 can be absorbed by a molecule that is in its basic vibrational state, when the interaction takes place. Portion of the energy of the photon is transported to the Raman-active mode having frequency υ_m. The resultant frequency of dispersed light is decreased to $(\upsilon_0 - \upsilon_m)$. This frequency is termed as **Stokes** frequency.
- Photon having frequency υ_0 can be absorbed by a molecule that is literally in its excited vibrational state at the time of interaction. When the extra energy of the excited mode is liberated, the molecule proceeds towards the basic vibrational state and the resultant frequency of dispersed light rises up to $(\upsilon_o + \upsilon_m)$. This frequency is titled **Anti-Stokes** frequency.
- A molecule without any Raman-active modes absorbs a photon of the frequency υ_0. The excited molecule goes back to the same basic vibrational state and releases light with the same frequency υ_0 as an excitation source. This type of interaction is entitled as an elastic **Rayleigh scattering**.

A.6.8 Thermogravimetric Analysis (TGA)

TGA is one sort of thermal stability analysis, where the sample is heated from room temperature (27 ˚C) up to ~1000 ˚C for the observation of the variations in its chemical and physical features.

Fig.A.9 Experimental setup of TGA: Perkin Elmer Pyris 1 (CIPET, Lucknow)

The TGA study of a material embraces the loss of mass with growing temperature. From the exploration, various properties of the material like, decomposition, desorption, vaporization, dehydration, degradation, phase transition etc. can be investigated.

The instrument (Fig. A.9) principally consists of a balance with great precision kept inside a programmable furnace. The material is kept on a sample holder stuck on the balance for uninterrupted weight revelation. The interior temperature of the furnace is slowly elevated at certain rate and the weight loss is recorded all through. The output is presented as a plot between the weight (or the percentage weight loss) of the material vs. applied temperature

Solar Energy 188 (2019) 278–290

Contents lists available at ScienceDirect

Solar Energy

journal homepage: www.elsevier.com/locate/solener

Improved sensing behaviour of self-healable solar light photodetector based on core-shell type $Ni_{0.2}Zn_{0.8}Fe_2O_4$@ poly (Urea-Formaldehyde)

Shakti Singh[a], Abhisikta Bhaduri[b], Ravi Kant Tripathi[a], Khem Bahadur Thapa[b], Rajeev Kumar[c], Bal Chandra Yadav[a,*]

[a] Nanomaterials and Sensors Research Laboratory, Department of Physics, Babasaheb Bhimrao Ambedkar University, Lucknow 226025, India
[b] Department of Physics, Babasaheb Bhimrao Ambedkar University, Lucknow 226025, India
[c] CSIR-Advanced Materials and Processes Research Institute, Bhopal 462026, India

ARTICLE INFO

Keywords:
Micro-encapsulated ferrite
Self-healable photodetector
Electronic waste
Service life
Electricity conservation

ABSTRACT

In this work, a bilayered ultra responsive self-healable photodetector that can restore both its structure as well as sensing property after deformation has been reported. This photodetector is based on ferrite with ultrafast sensing ability along with restoration property. In this dual-layered structure, the upper layer is $Ni_{0.2}Zn_{0.8}Fe_2O_4$ (NZF) prepared by citrate gel method and acts as sensing layer, whereas, the lower layer is Urea-Formaldehyde (U-F) microcapsules with flaxseed oil and NZF core. Here bottom layer acts as a healing layer, which can successfully restore film sensing property after deformation. Flaxseed oil acts as a medium to transport NZF from lower layer to the upper sensing area, which was deformed manually. The evaluated photoresponse and recovery time of NZF before deformation are 1.74 sec and 3.28 sec at 100 mW/cm^2 respectively, whereas, response and recovery after healing were 1.75 sec and 2.84 sec respectively. The solar light photodetector based on microcapsule that can restore its sensing property ~98.5%. The purpose of this work is to develop a method by which anyone can fabricate the different types of self-healable solar light photodetector.

1. Introduction

Non-renewable energy resources like fossil fuel, coals etc. are going to deplete in the near future. The continuous increment in global population and socio-economics will lead to the consumption of more and more electricity (Destek and Aslan, 2017). Non-renewable energy alone cannot fulfil these electricity requirements and hence conventional energy resources will play a vital role in the near future. Electricity conservation is as important as electricity generation to gain sustainable growth. Various research groups continuously working on superconductors (Saito et al., 2016; Charnukha et al., 2018), batteries (Han et al., 2015; Song et al., 2015; Sun et al., 2017), light dependent resistors (LDR) (Rawal et al., 2015; Tripathi et al., 2018) in order to save the generated electric power. Most of the countries are wasting a huge amount of electric power due to unnecessarily overriding of lightning equipment during day time. The unfamiliarity of the energy saving policies and the high cost of automatic switches, like light dependent resistors (LDRs), seem to be the main reasons for electrical energy wastage (Rawal et al., 2016, 2017). The solar light photodetector has a property to change their resistance with a variation of light intensity. Nanostructured metal oxides and metal sulphides are extensively explored for photoconductors and photo-conducting light switches (Kripal et al., 2011; Tripathi et al., 2015; Georgakopoulos et al., 2015), while ferrites are the least investigated materials for photodetector applications.

Other well-known problems in context to the serviceability of electronic devices e.g. photodetectors are continuous degradation of these devices by means of corrosion, repeated mechanical strain and damage during functioning. Even a slight change in a structural design by means of external cause leads to a gigantic change in output performance. In some cases, this causes the total failure of the whole device. These deformations in electronic devices lead to a tremendous increment in electronic waste (E-waste) year by year. Approximately, 44.7 million metric ton of e-waste was generated in 2016 and 47 million metric tons in 2017 (Baldé et al., 2017). Moreover, e-waste creates severe environmental and human health impacts. As these wastes contain heavy and toxic materials like Hg, Cd, Pb, etc. (ISWA, 2009), which contaminate groundwater and soil which directly or indirectly affects all living organisms (Leung et al., 2006; Zhang and Xu, 2016; Labunska et al., 2013). In recent years, research communities are trying to develop self-healable electronic devices, which can regenerate their structures and electrical properties after a mechanical failure. There is

* Corresponding author.
E-mail address: bcyadava@bbau.ac.in (B.C. Yadav).

https://doi.org/10.1016/j.solener.2019.06.003
Received 9 April 2019; Received in revised form 28 May 2019; Accepted 3 June 2019

Journal of Colloid and Interface Science 600 (2021) 572–585

Contents lists available at ScienceDirect

Journal of Colloid and Interface Science

journal homepage: www.elsevier.com/locate/jcis

Regular Article

2-D self-healable polyaniline-polypyrrole nanoflakes based triboelectric nanogenerator for self-powered solar light photo detector with DFT study

Shakti Singh [a], Ravi Kant Tripathi [a], Manoj Kumar Gupta [b], Gulzhian I. Dzhardimalieva [c], Igor E. Uflyand [d], BalChandra Yadav [a,*]

[a] Nanomaterials and Sensors Research Laboratory, Department of Physics, Babasaheb Bhimrao Ambedkar University, Lucknow 226025, India
[b] CSIR-Avanced Materials and Processes Research Institute, Bhopal 462026, India
[c] Laboratory of Metallopolymers, The Institute of Problems of Chemical Physics RAS, Academician Semenov Avenue 1, Chernogolovka, Moscow Region 142432, Russian Federation
[d] Department of Chemistry, Southern Federal University, B. Sadovaya Str. 105/42, Rostov-on-Don 344006, Russian Federation

HIGHLIGHTS

- Synthesis of novel 2-D nanoflakes (~30 nm) of Polyaniline-Polypyrrole based conducting polymer.
- Acetone-assisted self-healing was observed in a polymeric thin film.
- Triboelectric nanogenerator (TENG) based on PANI-PPY nanoflakes (NFs) was fabricated.
- The input source in solar light photodetector with the maximum output voltage of ~149 volts was used.
- Ultra-fast response and recovery time (0.41 sec and 0.45 sec) were recorded respectively.
- The theoretical analysis was carried out using Gaussian 09 and Gauss view 05 software.

GRAPHICAL ABSTRACT

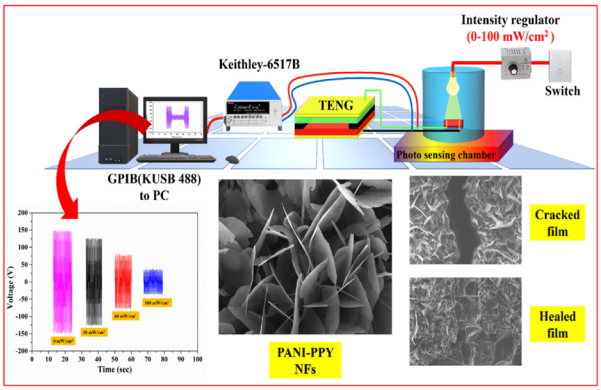

ARTICLE INFO

Article history:
Received 3 March 2021
Revised 5 May 2021
Accepted 9 May 2021
Available online 12 May 2021

Keywords:
Nanoflakes
Self-healing
Triboelectric nanogenerator
Self-powered photo sensor

ABSTRACT

This work demonstrates an easy and cost-effective synthesis of PANI-PPY conducting nanoflakes (NFs) with a self-healing capability. Scanning electron microscopic (SEM) analysis shows the minimum width of NFs as 30 nm, while HRTEM analysis confirms the shape, size, and semi-crystalline nature of the polymer. These PANI-PPY NFs were used to fabricate a contact separation mode triboelectric nanogenerator (TENG) based self-powered photosensor which gave the maximum output voltage (149 V), maximum output current (16 μA), current density 0.56 μAcm^{-2} and power density 83.56 μWcm^{-2}. Detailed literature survey shows the comparative study of PANI-PPY NF's with other photo-sensing materials. This literature review highlights the tremendous ability of PANI-PPY to self-restore and ultra-fast self-powering nature. This work also demonstrates a very easy and cost-effective method to develop polymeric nanomaterials via temperature-assisted polymerization, which need only a stirrer with a hot plate. Theoretical analysis (DFT calculations using Gaussian 09 and Gauss view 05) shows a consistent increase in stability when the number of molecules in the polymer chains analyzed was increased. The developed self-healing triboelectric nanogenerators exhibited stable performance before and after healing.

* Corresponding author.
E-mail address: bcyadava@bbau.ac.in (B. Yadav).

https://doi.org/10.1016/j.jcis.2021.05.052

Sensors & Actuators: B. Chemical 359 (2022) 131573

Contents lists available at ScienceDirect

Sensors and Actuators: B. Chemical

journal homepage: www.elsevier.com/locate/snb

Gigantic stimulation in response by solar irradiation in self-healable and self-powered LPG sensor based on triboelectric nanogenerator: Experimental and DFT computational study

Shakti Singh [a], Prabhakar Yadav [b], Manoj Kumar Gupta [c], Gulzhian I. Dzhardimalieva [d,e], Jinhwan Yoon [f], Chiranjit Maiti [f], Bal Chandra Yadav [a,*]

[a] Nanomaterials and Sensors Laboratory, Department of Physics, Babasaheb Bhimrao Ambedkar University, Lucknow 226025, India
[b] Department of Electrical Engineering, Shri Ram Swarup College of Engineering and Management, Lucknow, U.P., India
[c] CSIR-Avanced Materials and Processes Research Institute, Bhopal 462026, India
[d] Engineering Department, Moscow Aviation Institute (National Research University), 125993 Moscow, Russia
[e] Laboratory of Metallopolymers, The Institute of Problems of Chemical Physics RAS, Academician Semenov avenue 1, Chernogolovka, Moscow Region 142432, Russian Federation
[f] Department of Chemical Materials, Institute for Plastic Information and Energy Materials, Sustainable Utilization of Photovoltaic Energy Research Center, Pusan National University, Busan 46241, Republic of Korea

ARTICLE INFO

Keywords:
Triboelectric nanogenerator
Self-powered sensor
Waste energy
2D material
Photo induced sensor

ABSTRACT

The present paper reports the highest sensor response of Solar light induced, battery-less and self-healable LPG sensor powered by triboelectric nanogenerator. This work establishes the concept of waste to energy conversion and utilization of waste energy (finger tapping) for driving sensors for green and sustainable development. In this study synthesis of 2D PANI-PPY (2P) nanosheets by the polymerization and further its employment as PDMS/PANI-PPY (3P) based TENG is demonstrated. The fabricated TENG exhibits high output voltage of 142 volts and 80 μA current. 3P polymer nano-composite showed fast self-healing capability under 35 min. The assembled 3P based self-powered LPG sensor exhibits exceptional response and sensitivity under light illumination. The maximum sensor response of 94.67 (% response = 9367%) and the sensitivity 52.67 SR/vol% were found under 30 mW/cm^2 visible light radiance, which illustrates that the developed material is extremely responsive and sensitive under light condition even at a very low concentration of LPG below LEL (2 vol%). The least recovery and response times of the material were measured to be 172 ms and 580 ms correspondingly. The theoretical analysis confirms that Cl-doped 2P was highly reactive and exhibited high negative potential sites to interact with the H^+ ion of LPG.

1. Introduction

Nanogenerator technology is one of the most evolving fields, ever since the discovery of Piezoelectric nanogenerator (PENG) [1] and triboelectric nanogenerator (TENG) in 2006 and 2012 correspondingly [2]. The constant evolution of these technologies helps to develop the self-powered, renewable energy based, sustainable and high-performance hybrid nanogenerators [3,4], pressure sensors [5,6], moisture sensors [7–9], gas detectors [10–12], motion sensors [13–15], photocatalysis [16,17], etc. Conventional gas sensors which are resistive type [18,19], electrochemical [20,21], and optical [22,23], etc. have the disadvantage of high electric power expenditure, high operating temperature, and low sensor response. This greatly increases the service cost of the device. But nanogenerator based gas sensors solved these problems as they don't need any external power source and exhibit a high sensing response at room temperature (RT). Continuous monitoring of explosive and volatile gasses is extremely important. Liquified petroleum gas (LPG) which is a combination of propane and butane, is a highly explosive gas with a very low lower explosive limit (LEL) of 2.2 vol% [24,25]. Detection of this gas is extremely important as it covers a large distance in vapor form and household consumers of this gas are rising exponentially year by year. A minute error in detection of this gas early can cause devastating effects due to its explosive nature. For this various metal oxides like $BaTiO_3$ [25], graphene/CdO [26], MgO [27],

* Corresponding author.
E-mail address: balchandra_yadav@rediffmail.com (B.C. Yadav).

https://doi.org/10.1016/j.snb.2022.131573
Received 31 October 2021; Received in revised form 18 January 2022; Accepted 10 February 2022
Available online 22 February 2022

Journal of Hazardous Materials

Waste Material based Self-healable and Self-powered Detection of Hazardous Fluoride Ions and its Removal with Novel Adsorbent: An Unexplored and Highly Responsive Detection Method

--Manuscript Draft--

Manuscript Number:	
Article Type:	Research Paper
Keywords:	Fluoride detection; Self-powered sensor; fluoride removal; waste material; self-healing
Corresponding Author:	Bal Chandra Yadav, Ph.D. Babasaheb Bhimrao Ambedkar University LUCKNOW, INDIA
First Author:	Shakti Singh, M.Phil.
Order of Authors:	Shakti Singh, M.Phil.
	Chandra Bhan, M.Sc.
	Manoj Kumar Gupta, Ph.D.
	Jinhwan Yoon, Ph.D.
	Chiranjit Maiti, Ph.D.
	Jiwan Singh, Ph.D.
	Bal Chandra Yadav, Ph.D.
Abstract:	The current work outlines the finding of a distinctive method to detect hazardous fluoride ions in the water below permissible limits using a waste material-based self-healable triboelectric nanogenerator. In this work, the authors showed the steps involved to detect fluoride in a chemisorption-based self-powered sensor. The device is made-up of waste materials like BSR rubber, used polythene bags, and used plastic sheets, which validates the waste to energy conversion ability with maximum output voltage of ~242 volts and 40 μA current. The present self-powered fluoride detection device displays a maximum sensor response of 12.10 and a % sensor response of 1110%, which is very high. The self-healing ability of PDMS/BSR-La nanocomposite shows fast healing in ~25 min with a healing efficiency of 99.9%, which is one of the unique features of this device. Additionally, the present work also demonstrates not only recognition but the removal of fluoride ions using waste Juncus effusus biomass. The removal percentage of the fluoride was found to be 92.6% having an adsorption capacity of 2.31 mg/g. In summary, this paper establishes a special way to sense the fluorides and their removals using waste materials.

Manuscript Number- HAZMAT-D-22-06757

Федеральное государственное бюджетное учреждение науки
ИНСТИТУТ ПРОБЛЕМ ХИМИЧЕСКОЙ ФИЗИКИ
РОССИЙСКОЙ АКАДЕМИИ НАУК
(ИПХФ РАН)
проспект академика Семенова, д.1,
г. Черноголовка, Московская обл., 142432
Тел.: +7 (495) 993-57-07
e-mail: director@icp.ac.ru
http://www.icp.ac.ru

RUSSIAN ACADEMY OF SCIENCES
INSTITUTE OF PROBLEMS OF CHEMICAL PHYSICS
(IPCP RAS)
Academician Semenov av.1,
Chernogolovka, Moscow region, 142432 RUSSIA
tel.: +7 (495) 993-57-07
e-mail: director@icp.ac.ru;
http://www.icp.ac.ru

№12108-

На № _____ от _____

TO WHOM IT MAY CONCERN

This is to certify that **Mr. Shakti Singh**, PhD Scholar, Department of Physics, Babasaheb Bhimrao Ambedkar University, Vidya Vihar, Raebareli Road, Lucknow, U.P., India visited the Institute of Problems of Chemical Physics of the Russian Academy of Sciences (IPCP RAS) in Chernogolovka (Moscow region) during the period from October 13, 2021 to October 25, 2021 for joint scientific research in the framework of the DST-RFBR joint project INT/RUS/RFBR/P-375 "Preparation and properties of self-healing polymer based nanohybrid materials for energy harvesting application".

Sincerely yours,

Deputy Director of the Institute
of Problems of Chemical Physics
Prof. Elmira R. Badamshina